COMPARISON OF DIFFERENT ACTIVE SUSPENSION CONTROL STRATEGIES USING HALF CAR MODEL

A THESIS SUBMITTED TO
THE GRADUATE SCHOOL OF NATURAL AND APPLIED SCIENCES
OF
MIDDLE EAST TECHNICAL UNIVERSITY

BY

BANU ÇİÇEK BÜYÜKER

IN PARTIAL FULFILLMENT OF THE REQUIREMENTS
FOR
THE DEGREE OF MASTER OF SCIENCE
IN
MECHANICAL ENGINEERING

DECEMBER 2020

COMPARISON OF DIFFERENT ACTIVE SUSPENSION CONTROL STRATEGIES USING HALF CAR MODEL

submitted by **BANU ÇİÇEK BÜYÜKER** in partial fulfillment of the requirements for the degree of **Master of Science in Mechanical Engineering Department, Middle East Technical University by,**

Prof. Dr. Halil Kalıpçılar
Dean, Graduate School of **Natural and Applied Sciences** _____

Prof. Dr. M.A. Sahir Arıkan
Head of the Department, **Mechanical Engineering** _____

Assist. Prof. Dr. Kerem Bayar
Supervisor, **Mechanical Engineering, METU** _____

Examining Committee Members:

Prof. Dr. Ender Ciğeroğlu
Mechanical Engineering, METU _____

Assist. Prof. Dr. Kerem Bayar
Mechanical Engineering, METU _____

Assoc. Prof. Dr. A. Buğra Koku
Mechanical Engineering, METU _____

Assoc. Prof. Dr. Yiğit Yazıcıoğlu
Mechanical Engineering, METU _____

Assoc. Prof. Dr. Can Ulaş Doğruer
Mechanical Engineering, Hacettepe University _____

Date: 30.12.2020

I hereby declare that all information in this document has been obtained and presented in accordance with academic rules and ethical conduct. I also declare that, as required by these rules and conduct, I have fully cited and referenced all material and results that are not original to this work.

Name, Last name : Banu Çiçek Büyüker

Signature :

ABSTRACT

COMPARISON OF DIFFERENT ACTIVE SUSPENSION CONTROL STRATEGIES USING HALF CAR MODEL

Büyüker, Banu Çiçek
M.S., Department of Mechanical Engineering
Supervisor: Assist. Prof. Dr. Kerem Bayar

December 2020, 108 pages

Among other advances in ground vehicle technology, active suspension systems play an important role in improving ride comfort, handling and road holding vehicles. Ride comfort is affected by vehicle motions, such as body bounce, pitch and roll, but also limiting wheel travel and suspension deflection is important for road holding performance. The main motivation of this study is designing different control strategies for active suspension systems equipped with a linear electric motor and making a comprehensive assessment of active suspension systems by comparing these control methods. To achieve this aim, initially, characteristics of linear actuators are reviewed, and a linearized half-car model is obtained with four degrees of freedom. Then in order to compensate the effects of the road profile on ride comfort, PID, LQR, H_∞ and sliding mode controllers are developed. Genetic and gradient-based optimization algorithms are used. Simulations are carried out, and bounce, pitch, wheel travel and suspension deflection of the vehicle are observed. Time-domain and frequency domain analyses were performed to evaluate ride comfort and the effectiveness of controllers.

Keywords: Active Suspension, LQR, Optimization, H_∞ Control, Sliding Mode Control

ÖZ

YARIM ARAÇ MODELİ KULLANARAK FARKLI AKTİF SÜSPANSİYON KONTROL STRATEJİLERİNİN KARŞILAŞTIRILMASI

Büyüker, Banu Çiçek
Yüksek Lisans, Makine Mühendisliği Bölümü
Tez Yöneticisi: Assist. Prof. Dr. Kerem Bayar

Aralık 2020, 108 sayfa

Bugünlerde kara araçlarının performansları gün geçtikçe hızlı bir şekilde artmaktadır. Diğer gelişmelerin yanında, aktif süspansiyon sistemlerindeki ilerlemeler sürüş komforunu ve aracın yol tutuşunu artırmakta önemli rol oynamaktadır. Sürüş komforu şasinin dikey hareketi, yunuslama ve yuvarlanma gibi hareketlerinden etkilenir, bunun yanında tekerlek hareketlerini ve süspansion sıkışmasını sınırlandırmak yol tutuş performansı için önemlidir. Bu çalışmanın ana amacı, doğrusal elektrik motorlu aktif süspansiyon sistemleri için farklı kontrol stratejileri tasarlamak ve bu kontrol methotlarını karşılaştırarak aktif süspansiyon sistemleri üzerine kapsamlı bir değerlendirme yapmaktır. Bu amaç doğrultusunda, öncelikle doğrusal motorların karakteristiği incelenmiş ve dört bağımsız değişkenli doğrusal yarı araç modeli oluşturulmuştur. Daha sonra yol profili kaynaklı rahatsızlığı kompanse etmek için PID, LKR, H_∞ ve kayan kipli kontrolcüler tasarlanmış ve sisteme uygulanmıştır. Genetik algoritma ve gradiant temelli optimizasyon algoritması kullanılmıştır. Simülasyonlar yapılmıştır ve aracın dikey hareketi, yunuslaması, tekerlek hareketleri ve süspansion sıkışması gözlenmiştir. Sürüş komforunu ve kontrolcülerin etkinliğini değerlendirmek için zaman ve frekans temelli analizler gerçekleştirilmiştir.

Anahtar Kelimeler: Aktif Süspansiyon, LKR,Optimizasyon, H_∞ Kontrol, Kayan Kipli Kontrol

To my family,

ACKNOWLEDGMENTS

First, I would like to thank my Supervisor Assist. Prof. Dr. Kerem Bayar for his guidance and advice for working discipline. I would also like to thank Prof. Dr. Ender Ciğeroğlu for his suggestions and comments.

Support of The Scientific and Technological Research Council of Turkey (TÜBİTAK) for TÜBİTAK 3501 project is also gratefully acknowledged.

I would like to thank my dear friends Berk Ataeli and Halil Mutlu have supported and cheered me up all the time. Also, I would like to thank my colleagues in Roketsan Missiles Inc., Cem Mortaş, Damla Çolak, and Görkem Günay for their support and friendship.

Finally, I would like to express my special thanks to my mother and father, Serpil and Veli Büyüker, for their endless love, patience and support.

TABLE OF CONTENTS

LIST OF TABLES

TABLES

LIST OF FIGURES

FIGURES

LIST OF ABBREVIATIONS

ABBREVIATIONS

DFT	Discrete Fourier Transform
FFT	Fast Fourier Transform
GA	Genetic Algorithm
GD	Gradient Descent
IMU	Inertial Measurement Unit
LMI	Linear Matrix Inequality
LQR	Linear-Quadratic Regulator
PID	Proportional-Integral-Derivative
PSD	Power Spectral Density
RMS	Root Mean Square
RMSE	Root Mean Square Error
SISO	Single Input Single Output
SMA	Sprung Mass Acceleration
SMC	Sliding Mode Control

LIST OF SYMBOLS

SYMBOLS

z_s	Sprung mass displacement
θ	Pitch angle
z_f	Front unsprung mass displacement
z_r	Rear unsprung mass displacement
z_0	Input coming from road
k_{sf}	Front suspension stiffness
k_{sr}	Rear suspension stiffness
c_{sf}	Front suspension damping
c_{sr}	Rear suspension damping
k_t	Tire stiffness
M_s	Sprung mass
I_{yy}	Inertia of vehicle body
m_u	Unsprung mass
V_x	Vehicle speed
a	Distance from center of gravity to front axle
b	Distance from center of gravity to rear axle
a_z	Sprung mass acceleration
x	System states
u	Actuator input
g	Gravity

CHAPTER 1

INTRODUCTION

1.1 Background

The suspension systems play an important role in ride comfort and road holding of vehicles. The main goal of the suspension systems is improving ride comfort and handling performance by compensating the road profile input. Handling is related to vehicle stability, and ride comfort is associated with vibration isolation. Vibration coming from the road can arise from road roughness, bumps, road irregularities or other external disturbances. There are conflicting objectives, though, between ride comfort and handling. Improving ride comfort may cause poor handling performance.

1.1.1 The Types of Suspensions

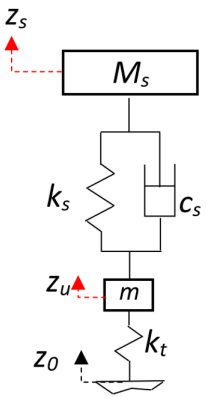

Figure 1.1: Quarter car model passive suspension system

Suspension systems can be categorized under three types: passive suspension, semi-active suspension and active suspension systems. A passive suspension system is represented in Figure 1.1. Passive suspension systems consist of suspension

damping, stiffness and tire stiffness. Additional tire damping can also be considered, but this damping is negligibly small; therefore, it is neglected. Semi-active suspensions have dampers with varying damping coefficients; these dampers are generally hydraulic or magnetorheological.

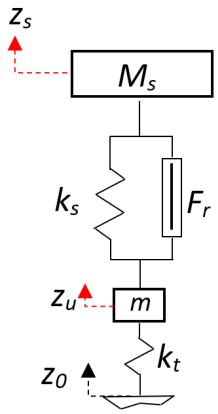

Figure 1.2: Quarter car model active suspension system

Finally, active suspension systems include actuators for producing necessary force, as shown in Figure 1.2 on a quarter car model. These actuators can be hydraulic or electromagnetic actuators. In this study, a linear motor based active suspension system is investigated.

1.1.2 Linear Electric Motor

Linear motors are used in applications that require high-performance translational motions such as high-speed robotics, high-performance positioning systems, automotive industry and air vehicles etc. Translational motion can be actuated with a rack and pinion or a belt and pulley system driven by rotatory motors. However, due to backlash, friction, limited acceleration performance, space constraints and limited operating frequency associated with a rotary motor, the use of a linear three-phase brushless motor is advantageous. [1]

The operation principle of the linear motor is identical to its rotary equivalent; in Figure 1.3, it is shown that the linear motor is a ‘non-rotational’ version of the rotary

motor. Single-sided motor magnets are mounted on the stationary part with the coil, and sensors are fitted to a moving assembly. Linear motors can be connected directly to the 3-phase AC supply, but it is not obligatory; a single-phase AC supply can also be used. That is advantageous for automotive vehicles because DC supplies are used in conventional vehicles, and producing a 3-phase AC signal is more complex and inefficient.

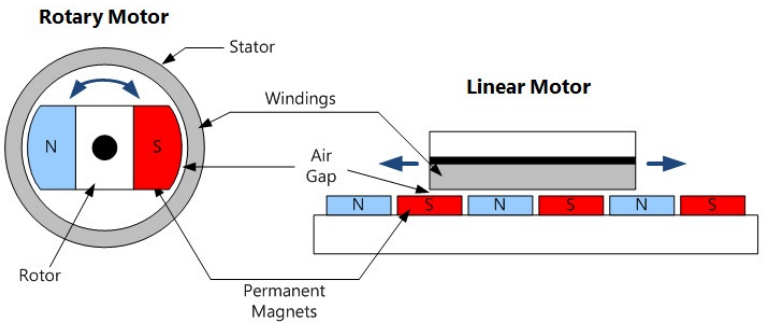

Figure 1.3: Internal structure of rotary and linear motor [2]

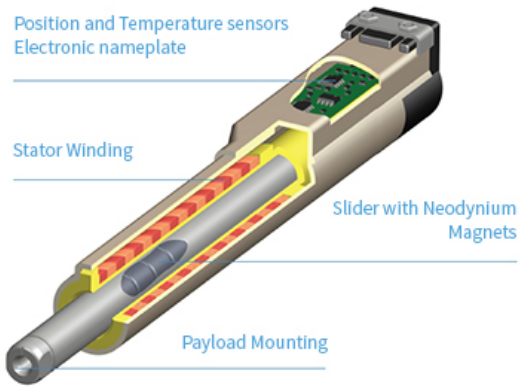

Figure 1.4: Typical linear actuator configuration of LinMot motors [3]

In addition to permanent magnets, position and temperature sensors shown in Figure 1.4 added to the linear motor. High precision working is satisfied with the help of these sensors. In this work, the linear motors on LinMot capable of providing a maximum force of 2150 N at 230 V AC [3] are presented.

1.2 Scope of Thesis

This study aims to investigate different control approaches for improving ride comfort without sacrificing road holding in a conventional passenger car equipped with linear electric motors at the rear suspensions. Active suspension system with linear motor is modeled and simulated considering different control techniques. Classical control methods are tried and compared with nonlinear and robust control methods. For the whole control methods considered, used optimization methods are applied.

There is no real-time control result given in this work. However, sensor and actuator sampling rates are taken into account in the simulations. The obtained results through the simulation are evaluated with ISO-2631 [4] standards; also, the design of random road profiles is based on ISO-8608 [5].

1.3 Literature Review

There is a considerable number of studies on active suspension systems focusing on different aspects. This literature survey can be done base on two main categories:

1. The actuator used in the suspension system; i.e., linear motor
2. The control methods applied

1.3.1 Linear Actuators

In [6], structures and models of various automotive suspensions are described. Consequently, it is stated that electromagnetic active suspensions are the future trend of automotive suspensions due to their simple structure, high-bandwidth, accurate and flexible force control, high ride quality, good handling performance, and energy regeneration. The electromagnetic linear actuator is direct-drive. Therefore, total roll and pitch elimination can be achieved, unlike passive and semi-active suspension systems.

In [7], a comparison of hydraulic and electromagnetic suspensions is made with respect to mathematical models. Also, force and dimension requirements of the suspension are included in this work. It is stated that the electromagnetic actuator is suitable for application in an automobile suspension.

In [8], it is mentioned that active suspensions will gain importance as electric vehicles are used more frequently. The main advantages and disadvantages of electromagnetic actuators are stated as:

- increased efficiency
- improved dynamic behavior
- stability improvement
- accurate force control
- dual operation of the actuator.

The disadvantages are as follows:

- an increased volume of the suspension for the same amount of force, compared to a hydraulic suspension
- relatively high current for a 12-V to 14-V system
- higher system costs

Moreover, Gysen et al. [8] state the advantage of the increased bandwidth of an electromagnetic actuator compared with a hydraulic actuator. It is observed that the bandwidth of the actuator is higher than 50 Hz, proving the improved dynamic force capability compared with a hydraulic system.

1.3.2 Control Methods

In [9], the two degrees of freedom dynamics model (quarter car model) is established with a PID controller to explore the vibration performance of the active suspension system of a car. The white noise model of the random road profile is simulated to excite the quarter car model. The method used for specifying PID gains is not stated in the study, but the results are good. The simulation results demonstrate that the ride

comfort would be significantly improved when the car suspension is controlled with the PID method.

Maurya and Bhangal [10] presented a quarter vehicle model, and two control techniques PID and LQR, are used to suppress the vibrations of the system. There is no optimization procedure applied for both PID and LQR in this paper. The results show that the results obtained with LQR are superior to PID.

The performance of the half-car system tested with two types of controllers in [11], namely Robust H_∞ control and LQR control. The weighting factors for robust H_∞ and LQR controllers are obtained using the Genetic Algorithm (GA). The objective function was set to reduce sprung mass vertical acceleration ($\ddot{x}_s$) of the vehicle. The performance constraints of the system other than sprung mass acceleration are not included in the optimization process of LQR. In the H_∞ controller development part of the paper, the aim is to obtain the state-feedback gain K to minimize $\|H_\infty\|$ of the closed-loop transfer function between the sprung mass acceleration and disturbance input.

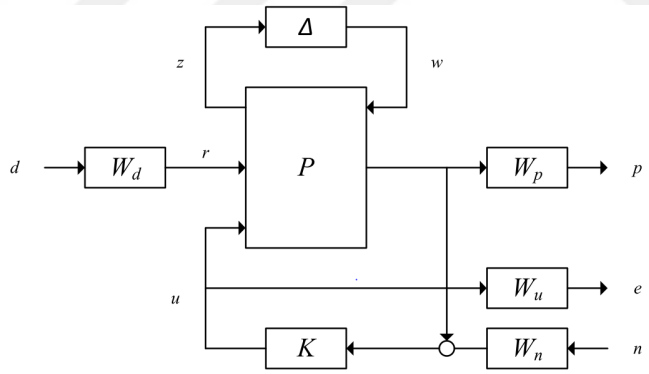

Figure 1.5: Closed-loop system with uncertainty [11]

W_d, W_p, W_u *and* W_n are added to the system. W_n represents the sensor noise, and it is taken 0.02. However, other parameters, W_d for noise coming from the road, W_u for actuator limit and W_p for performance specification, decided with GA. The paper concludes that a robust controller achieves better results than a passive suspension and LQR controller in all aspects under the random road profile.

It is well-known that sliding mode control is a high-performance, robust control method, and it is very effective against unpredictable external disturbances and unpredictable parameter variations. The sliding mode control method is appropriate for active suspensions due to the nature of active suspension control problem with white-noise random road input and variable sprung mass. Sliding mode control is discussed, and different types of it, such as adaptive, fuzzy or predictive sliding mode controls [12],[13],[14], etc., are frequently implemented in literature.

In [15], the optimal sliding surface design is made for the quarter car model. The non-linear quarter car model is described and linearized using the Lie derivative. A Kalman filter estimator is designed for state estimation purpose. The non-linear control is applied using improved optimal sliding mode control. In addition to the standard consideration of system states, derivative of sprung mass acceleration, which is jerk added to the system; hence, it increased system performance. Designed improved optimal sliding mode controller compared with passive suspension and fuzzy logical sliding mode control.

In [16], an improved optimal sliding mode control method is presented. Different from [15], sprung mass acceleration is added as a fifth state. Furthermore, the following methods are applied:

- Linearizing the nonlinear active suspension system
- Designing a Kalman estimator based on the linearized system
- Designing the improved sliding mode controller for the linearized system
- De-linearizing the control input

Improved optimal sliding mode control is compared with fuzzy logical sliding mode control and passive suspension system. For simulation input, road profiles in different roughness levels (B and D classes) and a bump are used. Both time and frequency domain results show that improved optimal control is best between the three control methods.

Zhou et al. [17] proposed an optimal sliding mode controller where coefficients of sliding surface are optimized with a Genetic Algorithm. In the optimization process, sprung mass acceleration, wheel travel and suspension deflection are taken into the performance index:

$$J = \frac{1}{T}\int_0^T \left[\ddot{z}_s^2 + \delta_1\left(z_u - z_q\right)^2 + \delta_2(z_s - z_u)^2\right] dt \qquad (1.1)$$

The sliding surface $S(X) = C_T X$ is defined and sliding surface parameter C_T is determined with GA. The optimal sliding mode controller results are compared with the sliding mode controller; the OSMC controller performed significantly better than the SMC controller.

In [18], the H_∞ controller is designed for a half-car model to eliminate the effect of the disturbance, which is random road input, on sprung mass and pitch accelerations. H_∞ controller gives a chance for developing a robust control against actuator uncertainty. Suspension deflection and dynamic wheel loads are taken as constrained outputs. Linear matrix inequalities (LMIs) are solved to obtain the state feedback gain, K such that the closed-loop system is stable and the constraints on the output are guaranteed. Simulations using the K value showed the effectiveness of the controller compared to the passive suspension.

Sun et al. [19] presented the H_∞ control method for active suspension control using a quarter car model. Sprung mass acceleration is taken as a performance index, and it is tried to be minimized against random road input. This work is distinctive because instead of traditional entire frequency range controllers, it aims to minimize the sprung mass acceleration, specifically at a frequency range, from 4 Hz to 8 Hz. It is the most critical frequency range, considering human ride comfort, with respect to [4]. These 4 Hz to 8 Hz finite frequency controllers are designed based on the generalized Kalman–Yakubovich–Popov (KYP) lemma. In this study, both state feedback and dynamic output feedback controllers are obtained for finite frequency and entire frequency cases. Dynamic outputs feedback controllers are crucial for systems with unmeasured or observable states. The results are impressive; the finite frequency controller gives better results than the entire frequency case for road types

B, C, E between 4 Hz and 8 Hz. Also, time-domain results are presented for bump input, and a system with a finite frequency controller gives a better response compared to the entire frequency H_∞ controller to bump.

1.4 Outline of the Thesis

In this thesis, an active suspension system equipped with a linear electric motor is analyzed. The thesis work starts with background information on suspension types and linear actuators. Chapter 1 continues with a summary of linear actuator technology and control methods applied to active suspension systems.

In Chapter 2, equations of motions for the half-car model with linear actuator are derived, and state-space representation of the system is presented. Also, the random input coming from the road is modeled.

In Chapter 3, the Kalman filter for the active suspension system is presented. Initialization and performance evaluation of the Kalman filter is also provided.

In Chapter 4, the time and frequency domain methods for ride comfort evaluation using the ISO 2631 criteria are given. The weighted frequency filter and comfort boundary lines for performance evaluation are explained.

In Chapter 5, controllers developed using PID, LQR, H_∞ control and SMC methods are derived. The LQR is optimized with GA and GD (gradient-descent) based optimization algorithms. For H_∞ control, finite frequency and entire frequency cases are combined.

In Chapter 6, the optimization methods used in Chapter 5, GA and Trust-Region, are explained. Also, the real-time spectrum analysis used for H_∞ control switching is presented.

In Chapter 7, first, the Kalman filter results are given, and the performance of the Kalman filter is evaluated. After that, the control methods explained in Chapter 5 are simulated, and results are compared. Test results for real-time spectrum analysis are given.

In Chapter 8, discussions and conclusions are made, and future work is mentioned.

CHAPTER 2

HALF-CAR VEHICLE MODEL

2.1 Equations of Motion of Half-car Model

The simplest suspension model for a car is given in Figure 2.1a, called a quarter car model of the passive suspension system. Considering an active suspension system, damping, k_s may be replaced with a linear electric motor, shown in Figure 2.1b.

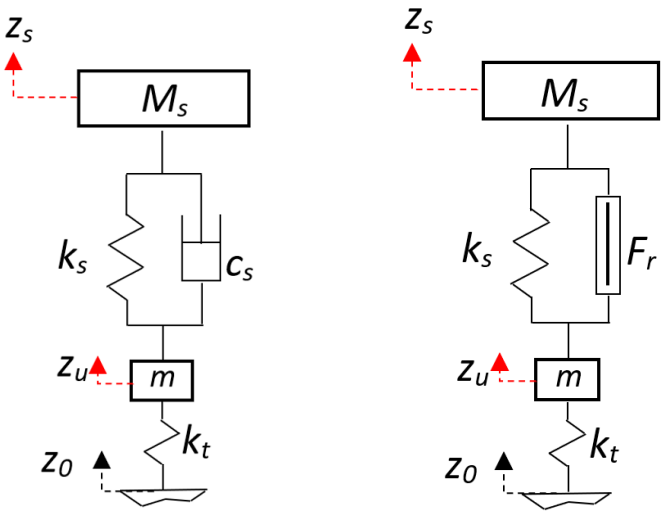

Figure 2.1: a. Passive quarter car model **b.** Active suspension quarter car model

In this work, the half-car model given in Figure 2.2 is preferred because it can be used for analyzing pitch motion beside sprung and unsprung mass accelerations. Due to the front compartment space limitations of the passenger car, linear motors only at the rear suspensions are considered.

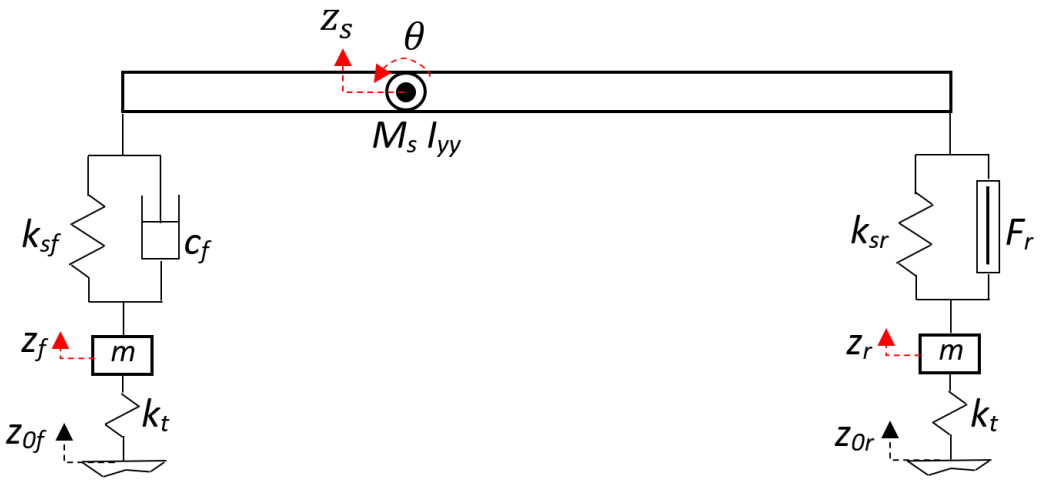

Figure 2.2: Half-car model with a linear actuator at the rear suspension

In Figure 2.2, k_{sf}, and k_{sr} , represent the front and rear suspension stiffness, c_f represents the front damping coefficient, k_t is the tire stiffness. The linear motor is represented by F_r, capable of providing a maximum force of 2150 N at 230 V AC [3], per suspension. z_0 is the road profile, z_f and z_r are the front and rear unsprung mass displacements, z_s is the sprung mass displacement, and θ is the pitch angle.

The equations of motion in the half-car model are defined by Equation 2.1.

$$\ddot{\theta} = \frac{1}{I_{yy}}[-b \times F_{sr} + a \times F_{sf} - h \times (K_{pitch}\theta + C_{pitch}\dot{\theta})]$$

$$M_s(\ddot{z}_s - V_x\dot{\theta}) - F_{sf} - F_{sr} = 0 \qquad (2.1)$$

$$2m_u\ddot{z}_f + F_{sf} - F_{tf} = 0$$

$$2m_u\ddot{z}_r + F_{sr} - F_{tr} = 0$$

Where F_{sf} and F_{sr} are front and rear suspension forces and F_{tf} and F_{tr} are front and rear tire forces. F_{sr}Rear suspension force changes depending on whether the suspension system is passive or active. For the passive suspension system F_r will be zero and for active system c_r will be a small value close to zero. Pitch stiffness, K_{pitch} and pitch damping, C_{pitch}, are assumed to be 0.

$$
\begin{aligned}
F_{sf} &= 2c_f\left(\dot{z}_f - \dot{z}_s + a \times \dot{\theta}cos\theta\right) + 2k_{sf}\left(z_f - z_s + a \times sin\theta\right) \\
F_{sr} &= 2c_r\left(\dot{z}_r - \dot{z}_s - b \times \dot{\theta}cos\theta\right) + 2k_{sr}(z_r - z_s - b \times sin\theta) + 2F_r \\
F_{tf} &= 2k_t\left(z_{0f} - z_f\right) \\
F_{tr} &= 2k_t(z_{0r} - z_r)
\end{aligned}
\tag{2.2}
$$

The suspension forces F_{sf} and F_{sr} are nonlinear parameters but to reach state-space representation, nonlinear parameters are linearized using small angle approximation, and a linear model is obtained.

$$
\begin{aligned}
cos\theta &\approx 1 \\
sin\theta &\approx \theta
\end{aligned}
\tag{2.3}
$$

Linearized forces are given in Equation 2.4, below.

$$
\begin{aligned}
F_{sf} &= 2c_f\left(\dot{z}_f - \dot{z}_s + a\dot{\theta}\right) + 2k_{sf}\left(z_f - z_s + a\theta\right) \\
F_{sr} &= 2c_r\left(\dot{z}_r - \dot{z}_s - b\dot{\theta}\right) + 2k_{sr}(z_r - z_s - b\theta) + 2F_r
\end{aligned}
\tag{2.4}
$$

2.1.1 State-Space Representation of the Suspension System

The states are taken as front and rear wheel travel, suspension deflection, unsprung mass speeds, pitch speed, and sprung mass vertical speed.

$$
x = \begin{bmatrix} x_1 \\ x_2 \\ x_3 \\ x_4 \\ x_5 \\ x_6 \\ x_7 \\ x_8 \end{bmatrix} = \begin{bmatrix} z_{0f} - z_f \\ z_{0r} - z_r \\ z_f - z_s + a\theta \\ z_r - z_s - b\theta \\ \dot{z}_f \\ \dot{z}_r \\ \dot{\theta} \\ \dot{z}_s \end{bmatrix}
\tag{2.5}
$$

The output matrix, y, includes three measured outputs, rear unsprung mass acceleration, pitch speed and sprung mass acceleration.

$$
y = \begin{bmatrix} \ddot{z}_r \\ \dot{\theta} \\ \ddot{z}_s \end{bmatrix}
\tag{2.6}
$$

The control input, u, is actuator force, F_r and disturbance input is derivative of road profile. The reason for taking derivative of road input for disturbance is states x_1 and x_2 includes road input, and as it is mentioned in Chapter 3, states are predicted with Kalman filter.

$$w = \begin{bmatrix} \dot{z}_{0f} \\ \dot{z}_{0r} \end{bmatrix} \tag{2.7}$$

The state-space representation can be written using equations of motions as below in Equation 2.8.

$$\begin{aligned} \dot{x} &= Ax + Bu + Gw \\ y &= Cx + Du \end{aligned} \tag{2.8}$$

where

$$A = \begin{bmatrix} 0 & 0 & 0 & 0 & -1 & 0 & 0 & 0 \\ 0 & 0 & 0 & 0 & 0 & -1 & 0 & 0 \\ 0 & 0 & 0 & 0 & 1 & 0 & a & -1 \\ 0 & 0 & 0 & 0 & 0 & 1 & b & -1 \\ \frac{k_t}{m_u} & 0 & -\frac{k_{sf}}{m_u} & 0 & -\frac{c_f}{m_u} & 0 & -\frac{c_f a}{m_u} & \frac{c_f}{m_u} \\ 0 & \frac{k_t}{m_u} & 0 & -\frac{k_{sr}}{m_u} & 0 & -\frac{c_r}{m_u} & \frac{c_r b}{m_u} & \frac{c_r}{m_u} \\ 0 & 0 & -\frac{2k_{sf}a}{I_{yy}} & \frac{2k_{sr}b}{I_{yy}} & -\frac{2c_f a}{I_{yy}} & \frac{2c_r b}{I_{yy}} & -2\frac{a^2 c_f + b^2 c_r}{I_{yy}} & 2\frac{c_f a - c_r b}{I_{yy}} \\ 0 & 0 & \frac{2k_{sf}}{M_s} & \frac{2k_{sr}}{M_s} & \frac{2c_f}{M_s} & \frac{2c_r}{M_s} & 2\frac{c_f a - c_r b}{M_s} + V_x & -2\frac{c_f + c_r}{M_s} \end{bmatrix}$$

$$B = \begin{bmatrix} 0 & 0 & 0 & 0 & 0 & -\frac{1}{2m_u} & \frac{b}{I_{yy}} & \frac{1}{M_s} \end{bmatrix}^T$$

$$G = \begin{bmatrix} 1 & 0 & 0 & 0 & 0 & 0 & 0 & 0 \\ 0 & 1 & 0 & 0 & 0 & 0 & 0 & 0 \end{bmatrix}^T$$

$$C = \begin{bmatrix} 0 & \frac{k_t}{m_u} & 0 & \frac{-k_{sr}}{m_u} & 0 & \frac{-c_r}{m_u} & \frac{bc_r}{m_u} & \frac{c_r}{m_u} \\ 0 & 0 & 0 & 0 & 0 & 0 & 1 & 0 \\ 0 & 0 & \frac{2k_{sf}}{M_s} & \frac{2k_{sr}}{M_s} & \frac{2c_f}{M_s} & \frac{2c_r}{M_s} & \frac{2(ac_f - bc_r)}{M_s} + V_x & \frac{-2(c_f + c_r)}{M_s} \end{bmatrix}$$

$$D = \begin{bmatrix} \frac{-1}{2m_u} & 0 & \frac{1}{M_s} \end{bmatrix}^T$$

(2.9)

The table below is used for necessary parameters.

Table 2.1: Half-car vehicle model parameters

Vehicle mass [kg]	1600
Unsprung mass [kg]	46
Wheelbase [m]	2.7
Distance from cg to front axle [m]	1.2
Distance from cg to rear axle [m]	1.5
Vehicle pitch moment of inertia [kg.m^2]	2000
Front suspension spring stiffness [N/m]	15000
Rear suspension spring stiffness [N/m]	20000
Suspension damping coefficient [N.s/m]	1100
Spring stiffness of tire [N/m]	180000
Maximum actuator force [N]	2150

2.2 Random Road Input

The effects of road irregularities on a vehicle are the fundamental reason for studying the dynamic characteristics of the vehicle suspension. Road irregularity is a complex random process. The response of a system to random inputs will also be a random process. Therefore, defining surface roughness in a suitable form is necessary. Power Spectral Density function for a includes pertinent information in the whole frequency range of interest. PSD is defined as limiting the mean-square value of a signal per unit frequency bandwidth in ISO [5].

The formula below gives the general form of the PSD:

$$S_o(\mathrm{n}) = S(\mathrm{n}_0)\left(\frac{\mathrm{n}}{\mathrm{n}_0}\right)^{-w} \tag{2.10}$$

where

$\mathrm{n}_0 = 0{,}1$ (cycles/m) is the reference spatial frequency;

w is the exponent of the fitted PSD.

In order to avoid the variance going to infinity at 0 spatial frequency shown by the figure and equation below, Equation 2.12 is used.

$$\lim_{n\to 0} S_0(n) \to \infty \tag{2.11}$$

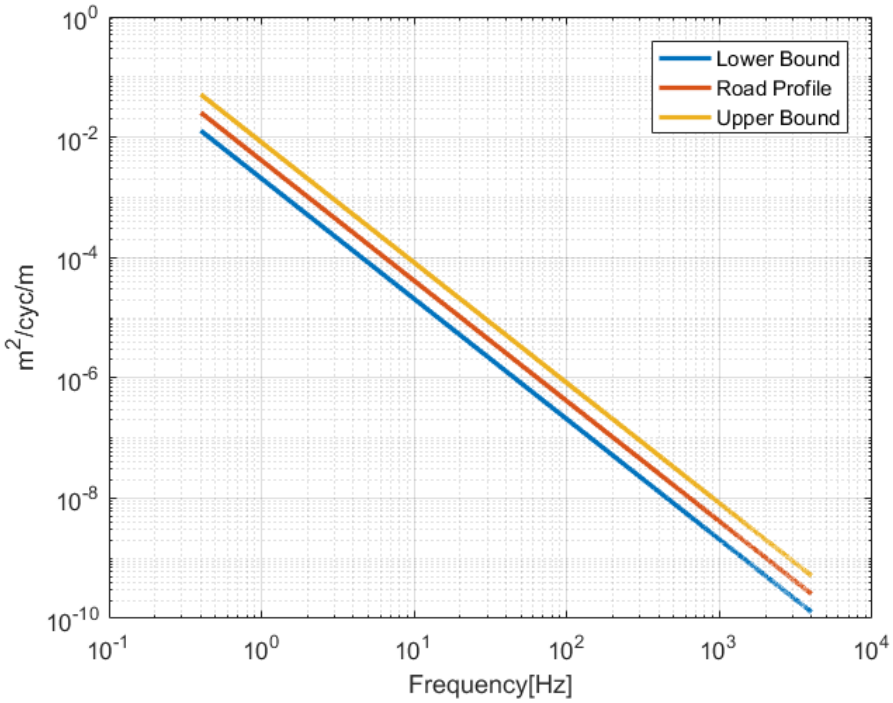

Figure 2.3: C class road profile using the general form in Equation 2.10

To overcome the difficulties of the model without a lower cut-off frequency "First-order Shape Filter" road model, which is valid in the whole frequency range, has been used [20].

$$S(\Omega) = \frac{2\alpha\sigma^2}{\pi}\frac{1}{\alpha^2 + \Omega^2} \quad for\ 0 < \Omega < \infty \tag{2.12}$$

where,

Ω : spatial angular frequency [rad/m],

α : spatial breakaway frequency [rad/m],

σ^2 : variance of road irregularity [m^2]

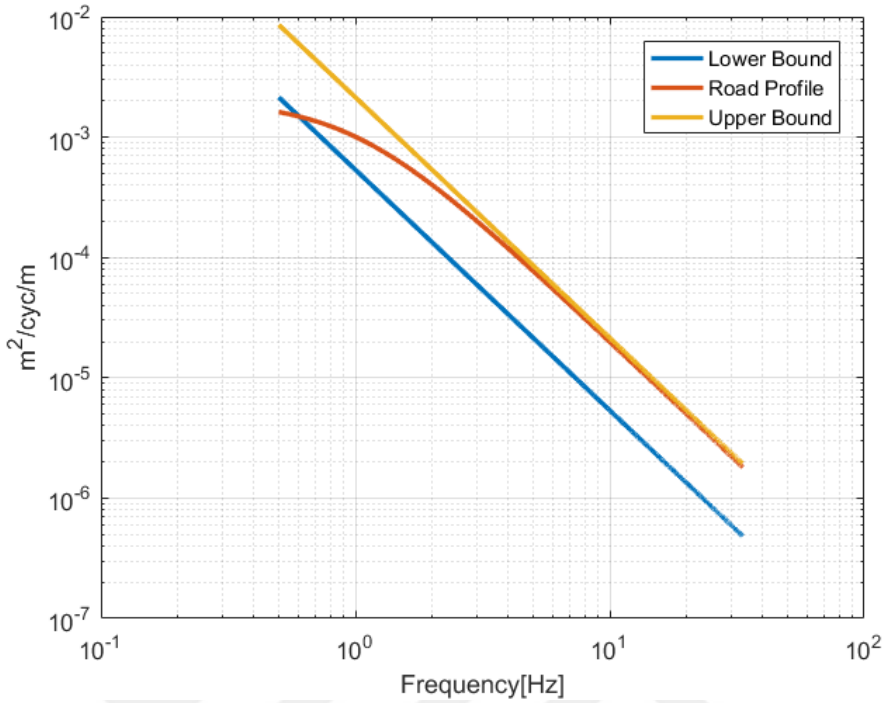

Figure 2.4: Poor asphalt road profile obtained by using first-order shape filter

The road displacement profile z_0 can be generated either in the frequency domain or time-domain by passing a white-noise gradient through a first-order shape filter. The required filter is expressed as:

$$\dot{z}_0(t) = -\alpha V z_0(t) + w(t) \tag{2.13}$$

where,

w(t) is white noise with intensity $2\alpha V\sigma^2$

The variation of the road profile height with time can be obtained by the solution of the first-order differential equation.

The table below is taken from ISO 8608 standards [5] and used for choosing road profiles.

Table 2.2: Road classification

Road class	Lower limit	Geometric mean	Upper limit
	Spatial frequency units, $\times 10^{-6}\ m^3$		
A	-	16	32
B	32	64	128
C	128	256	512
D	512	1024	2048
E	2048	4096	8192
F	8192	16384	32768
G	32768	65536	131072
H	131072	262144	-

Furthermore, by solving the differential equation above, Equation 2.12, the time-domain response of random road input can be observed.

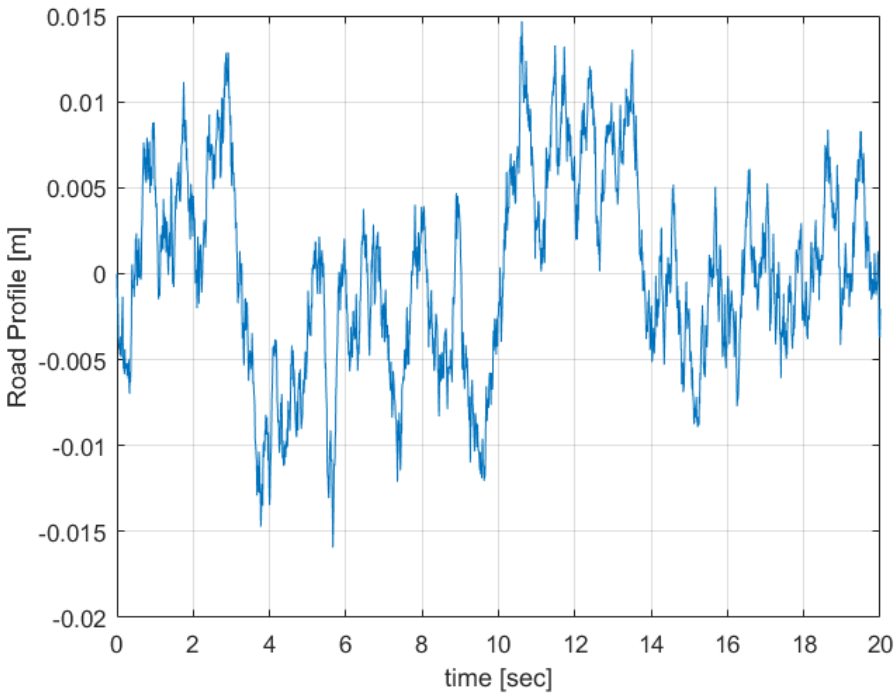

Figure 2.5: Time-domain random road input profile

CHAPTER 3

KALMAN FILTER FOR ACTIVE SUSPENSION SYSTEMS

3.1 Introduction

In a conventional, non-autonomous vehicle, the standard types of sensors are restricted. These sensors are sprung mass accelerometer and gyroscope that is capable of measuring pitch rate, roll rate and yaw rate sensors. In the active suspension vehicles, additional unsprung mass accelerometers can be found as well. In this study, cruising at constant speed is considered. In other words, braking, accelerating and steering movements are not considered in this study. For this reason, yaw and roll rate measurements are not taken into account.

The system states are set as front and rear wheel travel, suspension deflection, unsprung mass speeds, pitch speed, and sprung mass vertical speed, as stated in Chapter 2.1.1. The only measured state is the pitch speed, and other states are estimated. Since the front and rear wheel travels are included, estimating states is a challenge.

The covariance associated with measurement noise and sampling times of the sensors of a passenger car is shown in Table 3.1.

Table 3.1: Variances and sampling times of sensors in a conventional car

	$\dot{\theta}$	$\ddot{z}_s$	$\ddot{z}_u$
Variance	0.0001	0.001	0.4
Sampling Time	10 ms	10 ms	10 ms

3.2 Kalman Filter

Kalman filter is the estimator that gives the Bayesian solution for the problem of estimating the instantaneous states of a dynamical system in which both state evolution and measurement processes are linear and Gaussian. If these states are not linear and Gaussian other approaches of Kalman filter can be used. (e.g., Extended Kalman filter for nonlinear dynamical systems) [21],[22]

Consider a continuous-time state-space model of the form

$$\begin{aligned} \frac{dx(t)}{dt} &= A(t)x(t) + B(t)u(t) + G(t)w(t) \\ y(t) &= C(t)x(t) + D(t)u(t) + v(t) \end{aligned} \tag{3.1}$$

where $A(t)$ is the $n \times n$ state transition matrix, $B(t)$ is the $n \times k$ input matrix,$G(t)$ is a $n \times 1$ disturbance matrix, $w(t)$ is a $n \times 1$ process noise vector with zero mean and covariance matrix $Q(t)$. $C(t)$ is the $m \times n$ output matrix, $D(t)$ is the $m \times k$ direct transmission matrix, and $v(t)$ is the $m \times 1$ Gaussian random measurement noise vector with zero mean and covariance matrix $R(t)$.

Since the system is observable, the Kalman filter is applied to the system.

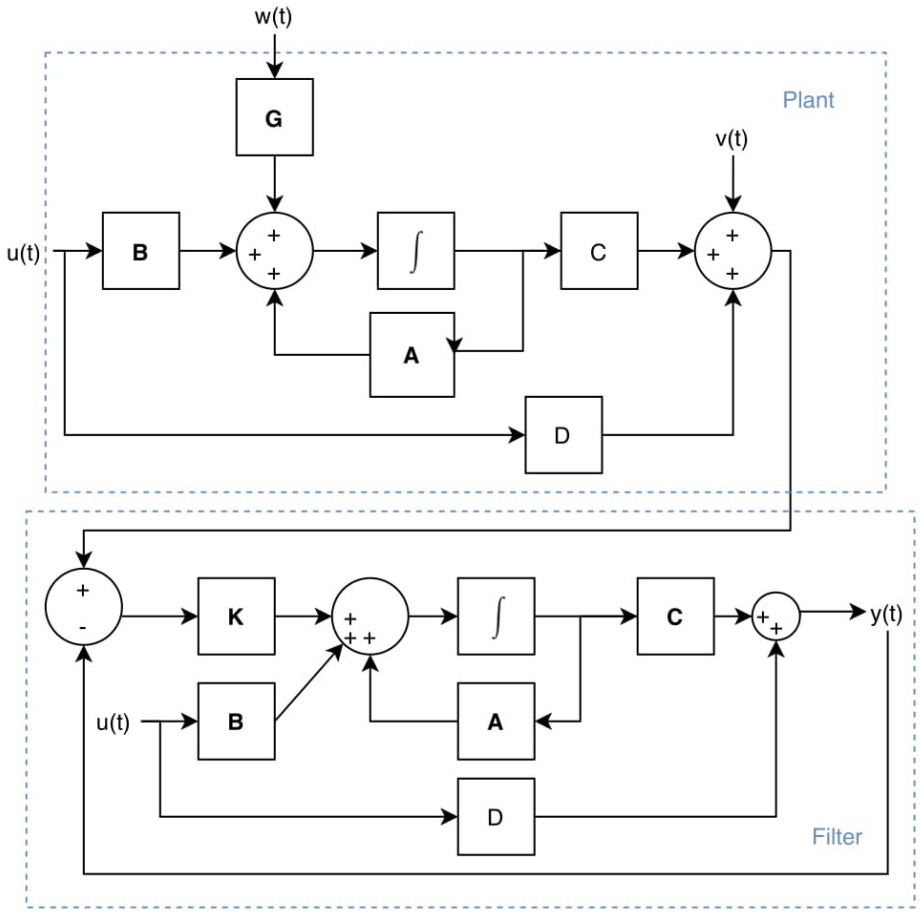

Figure 3.1: Kalman filter schematic

A general Kalman filter schematic is represented in Figure 3.1. To determine Kalman gain K in above schematic an estimation error should be defined

$$\tilde{x}(t) = x(t) - \hat{x}(t) \tag{3.2}$$

By using a performance measure as below

$$J(\tilde{x}(t)) = E\{\tilde{x}(t)^T \tilde{x}(t)\} \tag{3.3}$$

The gain K that minimizes J can be determined by equating a gradient of J to zero.

$$K(t) = P(t)C^T R^{-1} \tag{3.4}$$

where P(t) is the filtering error covariance found by the solution of Algebraic Riccati Equation below,

$$\frac{d}{dt}P(t) = AP + PA^T - PC^T R^{-1} CP + GQG. \tag{3.5}$$

A discrete-time Kalman filter can be derived based on the equations above. The equations for the discrete-time Kalman filter are given below.

Algorithm: Discrete Kalman Filter

Prediction:

1. $\hat{x}(k|k-1) = A(k-1)\hat{x}(k-1|k-1) + B(k-1)u(k-1)$
2. $P(k|k-1) = A(k-1)P(k-1|k-1)A(k-1)^T + G(k-1)Q(k-1)G(k-1)^T$

Update:

3. $K(k) = P(k|k-1)C(k)^T[C(k)P(k|k-1)C(k)^T + R]^{-1}$
4. $\hat{x}(k|k) = \hat{x}(k|k-1) + K(k)[y(k) - C(k)[A(k)\hat{x}(k|k-1) + B(k)u(k)] - D(k)u(k)]$
5. $P(k|k) = P(k|k-1) - K(k)C(k)P(k|k-1)$

Figure 3.2: Discrete-time Kalman filter algorithm for linear systems

In this algorithm, inputs are measurements $\{y(k)\}$, and outputs are an estimate of states $\{\hat{x}(k|k)\}$ at every time step. Before performing prediction and update steps mean, and covariance of the Gaussian state distribution should be initialized by setting $\hat{x}(0|0)$ and $P(0|0)$.

3.2.1 Initialization of Kalman Filter

The covariance matrix P is formed as a diagonal matrix whose individual elements are chosen according to the expected initial variances of system states.

$$P(0|0) = \begin{bmatrix} \sigma_{x_1}^2 & 0 & 0 & 0 & 0 & 0 & 0 & 0 \\ 0 & \sigma_{x_2}^2 & 0 & 0 & 0 & 0 & 0 & 0 \\ 0 & 0 & \sigma_{x_3}^2 & 0 & 0 & 0 & 0 & 0 \\ 0 & 0 & 0 & \sigma_{x_4}^2 & 0 & 0 & 0 & 0 \\ 0 & 0 & 0 & 0 & \sigma_{x_5}^2 & 0 & 0 & 0 \\ 0 & 0 & 0 & 0 & 0 & \sigma_{x_6}^2 & 0 & 0 \\ 0 & 0 & 0 & 0 & 0 & 0 & \sigma_{x_7}^2 & 0 \\ 0 & 0 & 0 & 0 & 0 & 0 & 0 & \sigma_{x_8}^2 \end{bmatrix} \tag{3.6}$$

If system states are not measured, variances in Equation 3.6 are not known; instead, the error covariance matrix can be calculated as

$$P(0|0) = C^T R C \tag{3.7}$$

where

$$R = \begin{bmatrix} \sigma_{y_1}^2 & 0 & 0 \\ 0 & \sigma_{y_1}^2 & 0 \\ 0 & 0 & \sigma_{y_1}^2 \end{bmatrix}. \tag{3.8}$$

R is the measurement covariance matrix, and variances are given in Table 3.1.

$x(0|0)$ is taken as (1×8) zero matrix by assuming the vehicle is stationary at the beginning.

The Kalman filter is realized in simulations using the Kalman filter block of MATLAB through initializations above.

3.2.2 Kalman Filter Performance Evaluation

Root mean squared error (RMSE) is one of the most widely used statistical measures in the performance evaluation of prediction algorithms, removing negative and positive error problems and evaluating prediction performance.

$$RMSE = \sqrt{\frac{\sum_{i=1}^{N}(x_i - \hat{x}_i)^2}{N}} \tag{3.9}$$

Given that RMSE formulation is used for performance evaluation of estimated parameters, these parameters are given in later Chapter 7.

CHAPTER 4

RIDE COMFORT EVALUATION

4.1 Introduction

The evaluation rubric of vibration measurement concerning human response includes different qualities like vibration environment, magnitudes, frequencies, directions and durations [24]. Vibration can be detected with other senses; they can be classified as touching, vision and hearing. In this study, the vibration is quantified by the accelerometer measuring are considered.

The vibration in vehicles can be felt over a wide range of frequencies, from less than 1 Hz to more than 300 Hz. At frequencies less than 0.5 Hz, the dominant effect may be motion sickness. A bandwidth from 0.5 to 80 Hz is related to health, comfort and perception. This bandwidth is considered sufficient for whole-body vibration. High frequencies can be termed as "hand-transmitted" or "hand-arm" vibration. [25]

For human body ride comfort, the most important frequency range is 4 Hz to 10 Hz. [5]

4.2 Weighted Frequency Filter

As stated before, vibration affects health, comfort, perception and motion sickness dependent on the vibration frequency content. While calculating the weighted sprung mass acceleration $a_w(t)$, ISO-2631 weighted frequency filter (Equation 4.1) is used.

The total weighting function is

$$H(s) = H_h(s)H_l(s)H_t(s)H_s(s) \tag{4.1}$$

Weighted frequency filter is expressed as a product of other transfer functions;

Band-limiting transfer functions:

High pass filter;

$$|H_h(s)| = \left| \frac{s^2}{s^2 + s\sqrt{2}\omega_1 + \omega_1^2} \right| \tag{4.2}$$

Low pass filter;

$$|H_l(s)| = \left| \frac{\omega_2^2}{s^2 + s\sqrt{2}\omega_2 + \omega_2^2} \right| \tag{4.3}$$

Acceleration-velocity transition transfer function:

$$|H_t(s)| = \left| \frac{1 + \frac{s}{\omega_3}}{1 + \frac{s}{Q_4\omega_4} + \left(\frac{s}{\omega_4}\right)^2} \right| \tag{4.4}$$

Upward step transfer function:

$$|H_s(s)| = \left| \frac{1 + \frac{s}{Q_5\omega_5} + \left(\frac{s}{\omega_5}\right)^2}{1 + \frac{s}{Q_6\omega_6} + \left(\frac{s}{\omega_6}\right)^2} \cdot \left(\frac{\omega_5}{\omega_6}\right)^2 \right| \tag{4.5}$$

Table 4.1: Parameters of the transfer functions of the principal frequency weightings

Weighting	Band limiting		Acceleration-velocity transition			Upward Step			
	$f_1[Hz]$	$f_2[Hz]$	$f_3[Hz]$	$f_4[Hz]$	Q_4	$f_5[Hz]$	Q_5	$f_6[Hz]$	Q_6
W_k	0.4	100	12.5	12.5	0.63	2.37	0.91	3.35	0.91
W_d	0.4	100	2.0	2.0	0.63	∞	-	∞	-
W_f	0.08	0.63	∞	0.25	0.86	0.00625	0.80	0.1	0.80

Table 4.1 stands for coefficients of transfer functions given by equations 4.2 - 4.5. W_k, W_d, W_f accounts for vertical, horizontal and lateral vibrations respectively. Vertical vibration is the one that affects ride comfort most; therefore, it will be a topic in this study. The frequency response of the resulting filter is shown in Figure 4.1 as a plot.

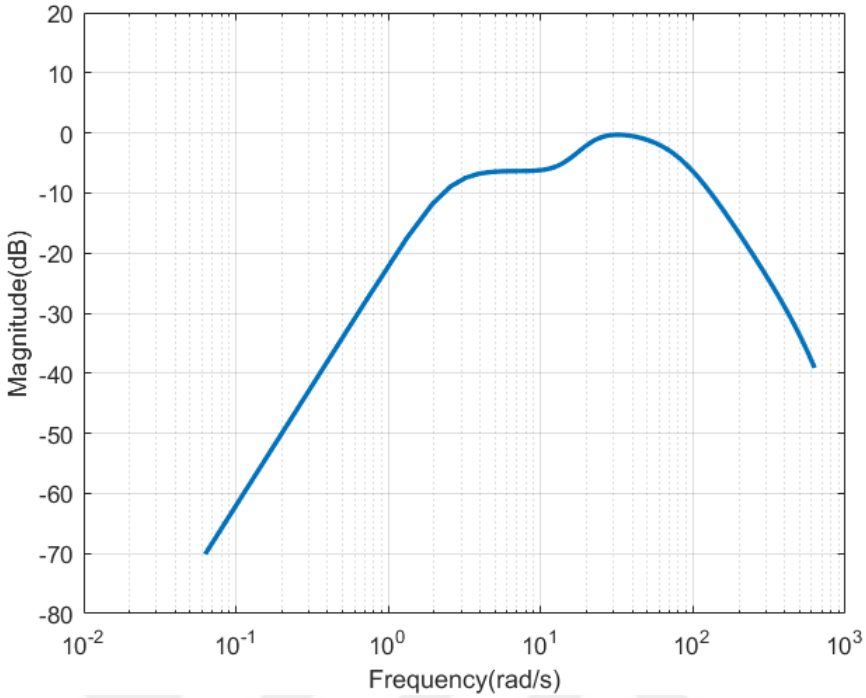

Figure 4.1: Frequency weighting function generated with transfer function in Equation 4.1

4.3 Time-domain Evaluation

Vibration assessment can be accomplished in the time-domain and frequency-domain in different aspects. Magnitude and duration of the vertical acceleration of the sprung mass should be considered for time-domain performance evaluation. Commonly, the RMS value of time-varying quantities are determined as:

$$a_{RMS} = \left[\frac{1}{T}\int_{t=0}^{T} a_w^2(t)dt\right]^{\frac{1}{2}} \tag{4.6}$$

where T is duration and $a_w(t)$ is the weighted sprung mass acceleration.

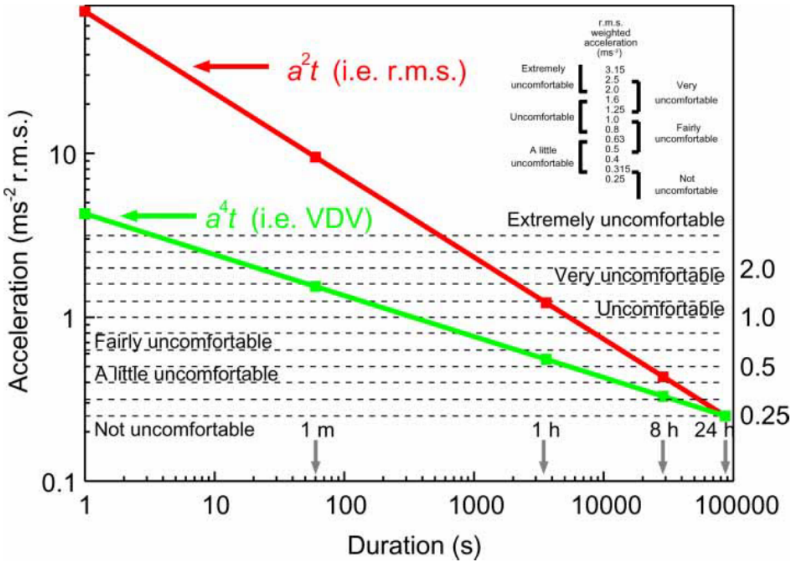

Figure 4.2: Ride comfort scale for time-domain response [24]

The given figure above (Figure 4.2) can be used as a scale for ride comfort in the time-domain, below 0.25 ms^{-2} RMS can be defined as comfortable and higher than 2.0 ms^{-2} RMS can be classified as extremely uncomfortable.

4.4 Frequency Domain Evaluation

4.4.1 Comfort Boundaries

It is also possible to evaluate ride comfort in the frequency-domain. The comfort boundary lines for 1 hour, 4 hours and 8 hours can be obtained by using ISO 2631-1:1985 standards (Table 4.2 and Table 4.3). But it should be noted that the original 1985 version of the standard has been withdrawn. However, in the new version, it is stated that "… the exposure boundaries recommended in ISO 2631-1:1985 were safe and preventive of undesired effects." Therefore, it is still used.

Table 4.2: ISO comfort boundaries for vertical vibrations limiting RMS values of acceleration

Frequency [Hz]	$a[m/s^2]$						
	1 min	16 mins	25 mins	1 hour	2.5 hours	4 hours	8 hours
1	1.778	1.349	1.127	0.749	0.444	0.337	0.2
4	0.889	0.673	0.571	0.375	0.225	0.168	0.1
8	0.889	0.673	0.571	0.375	0.225	0.168	0.1
80	8.89	6.73	5.71	3.75	2.25	1.68	1

Table 4.3: ISO comfort boundaries for vertical vibrations limiting PSD values of acceleration

Frequency [Hz]	$PSD[(m/s^2)^2]$		
	1 hour	4 hours	8 hours
1	2.42	0.489	0.173
4	0.152	0.031	0.011
8	0.076	0.015	0.005
80	0.757	0.153	0.054

Using Table 4.2 and Table 4.3, comfort boundary line graphs for RMS and PSD values are plotted as:

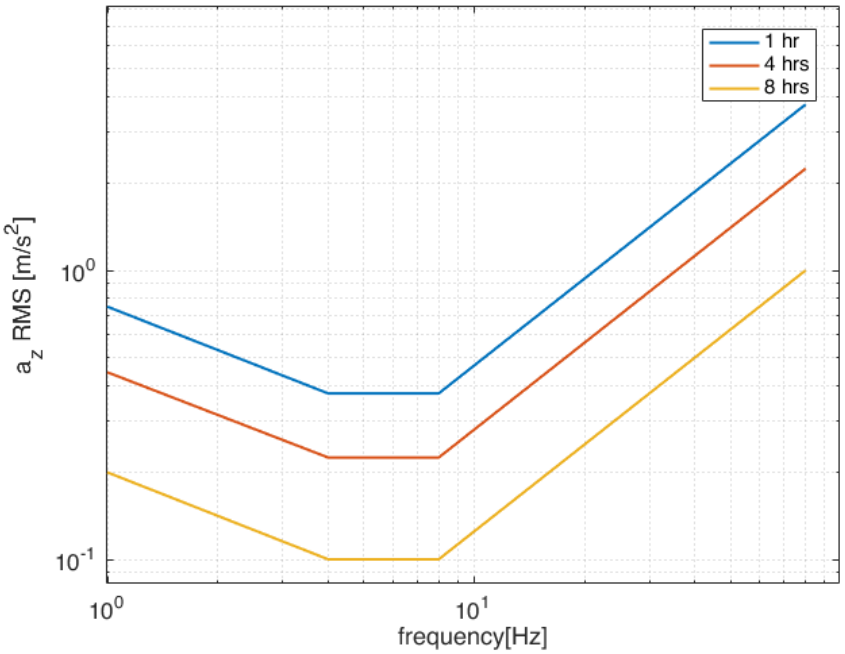

Figure 4.3: ISO comfort boundary lines for RMS values of sprung mass acceleration

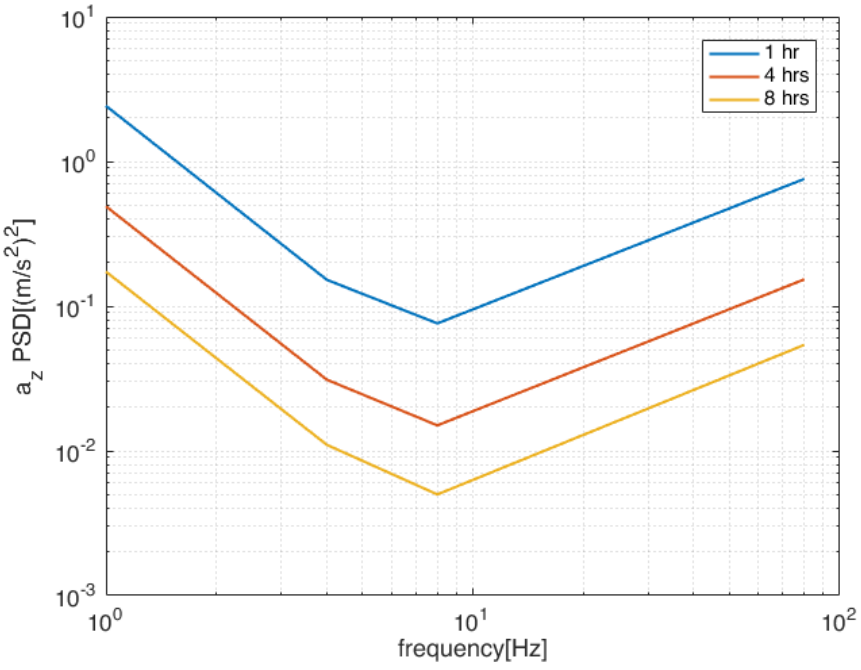

Figure 4.4: ISO comfort boundary lines for PSD values of sprung mass acceleration

CHAPTER 5

ACTIVE SUSPENSION CONTROLLER DESIGNS

5.1 PID Controller

PID controller is the most commonly used control method for controlling a wide range of systems. More than half of the industrial controllers used are kind of PID controllers [26]. This control method is commonly used because the mathematical model does not need to be known. Tuning the controller without conventional design techniques such as root locus is possible.

A PID controller includes three terms as Proportional, Integral and Derivative. It aims at minimizing the error between a desired reference input and measured output by manipulating K_p, K_i, K_d terms. Usually, K_p and K_d terms improve transient behavior and K_i is used to eliminate the steady-state error. But it should be noted that K_d the term can amplify the noise to the system.

PID controller has a transfer function;

$$G_c(s) = K_P + \frac{K_I}{s} + \frac{K_D s}{\tau_d + 1} \tag{5.1}$$

τ_d is usually selected as a very small value; thus transfer function of the controller can be further simplified to:

$$G_c(s) = K_P + \frac{K_I}{s} + K_D s \tag{5.2}$$

In the time-domain control input can be written as;

$$u(t) = K_P e(t) + K_I \int e(t)dt + K_D \frac{de(t)}{dt} \tag{5.3}$$

PID is applicable for single input single output (SISO) systems. Among the states of the active suspension system given by Equation 2.5 (pitch, unsprung mass accelerations, wheel travel, suspension travel etc.), sprung mass acceleration is the most critical variable for ride comfort improvement. Therefore, the PID controller is applied to sprung mass acceleration. The problem that is tried to be solved in this thesis is the disturbance rejection problem; thus, a schematic like below will be helpful.

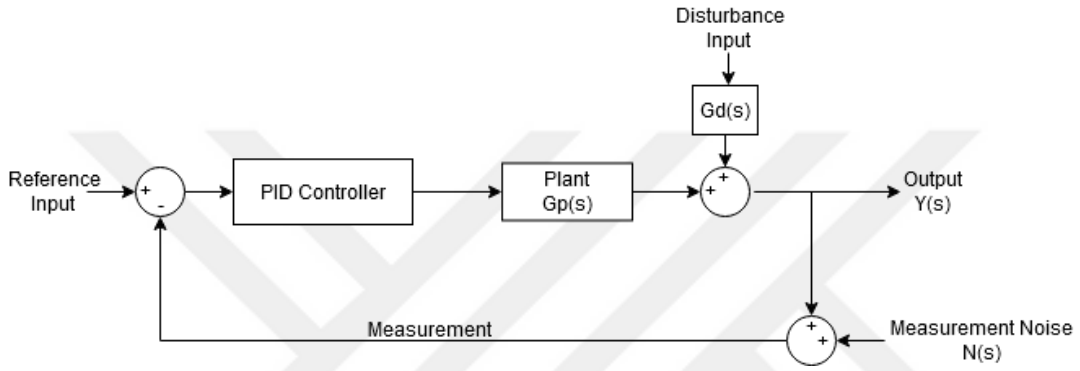

Figure 5.1: PID controller closed-loop schematics with disturbance

The transfer functions G_D and G_P are obtained by using the state-space model given in Chapter 2.1.1. To get an open-loop transfer function between control input (u) and output (sprung mass acceleration), the formulation

$$G_P(s) = C(sI - A)^{-1}B + D \tag{5.4}$$

is used. Note that C is chosen as 1×8, in which only output is sprung mass acceleration. But for open-loop transfer function between disturbance ($\dot{w}$) and output (sprung mass acceleration) the formulation

$$G_D(s) = C(sI - A)^{-1}G_1 + G_2 \tag{5.5}$$

is used. The closed-loop transfer function disturbance ($\dot{w}$) and output (sprung mass acceleration) is

$$\frac{Y(s)}{D(s)} = \frac{G_D(s)}{1 + G_C(s)G_P(s)} \tag{5.6}$$

Before the determination of PID coefficients, the stabilizability of the system should be checked. Root locus can be used for this purpose; roots of the characteristic equation are closed-loop poles of the system. A gain parameter is varied from 0 to infinity, and contributions of each open-loop pole or zero on locations of closed-loop poles and zeros are observed via the root locus method [26].

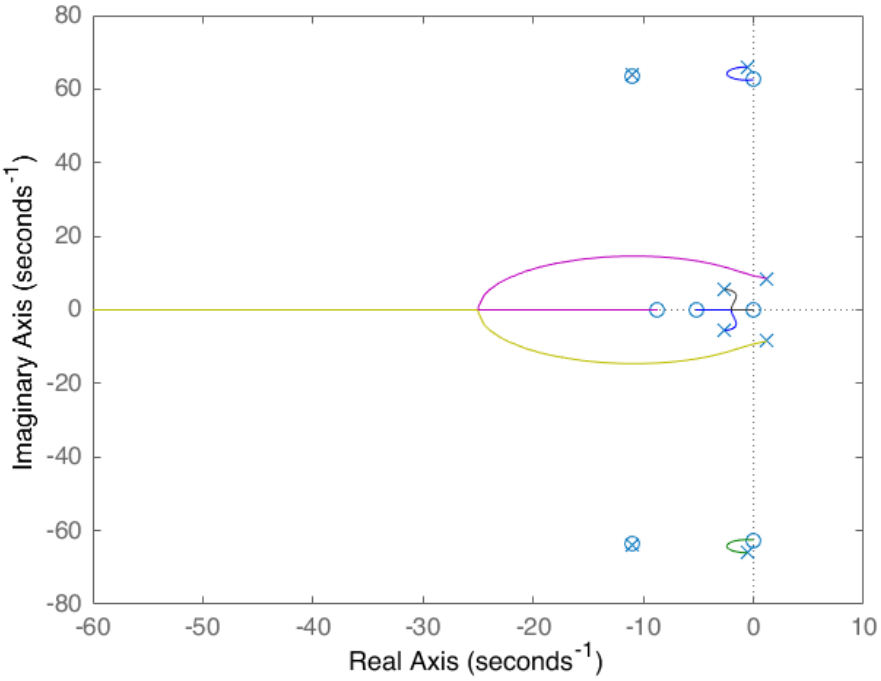

Figure 5.2: Root locus of the open-loop transfer function between disturbance and sprung mass acceleration, $G_D(s)$

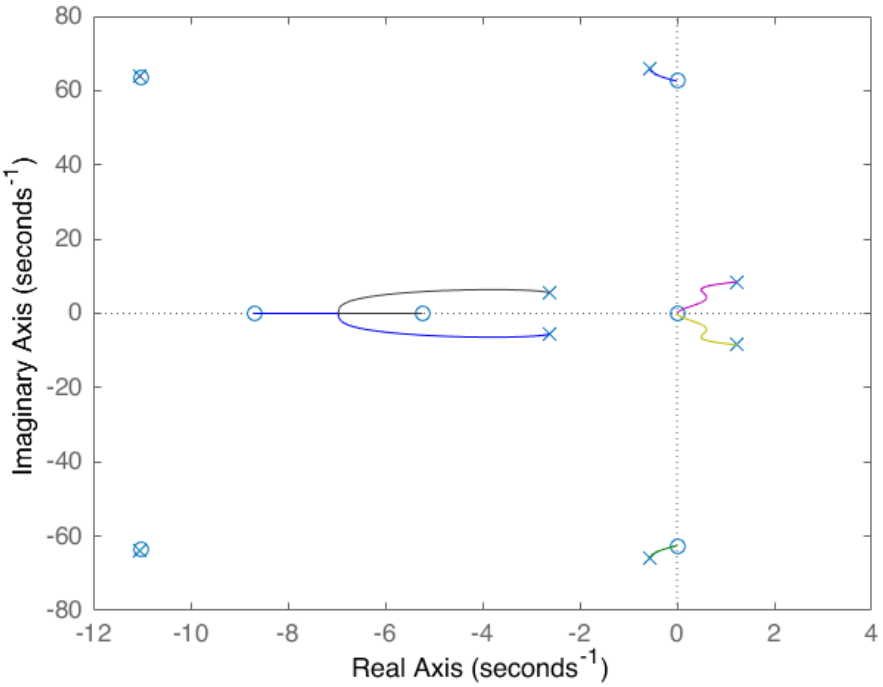

Figure 5.3: Root locus of the open-loop transfer function between control input (actuator) and sprung mass acceleration, $G_P(s)$

For the active suspension system given in Figure 5.1, the system should be stable with both disturbance input and control input excitations. Hence, the root loci of each system are checked in Figure 5.2 and Figure 5.3. It is observed that for some gain values, the system between random road input and SMA is stable (Figure 5.2). But for the second case, the system between actuator input and SMA, there are always closed-loop poles at the open right half-plane; hence the system is not stabilizable with proportional gain. The effect of the integral term of PID can be realized by adding a pole at the origin, as it is shown in Figure 5.4.

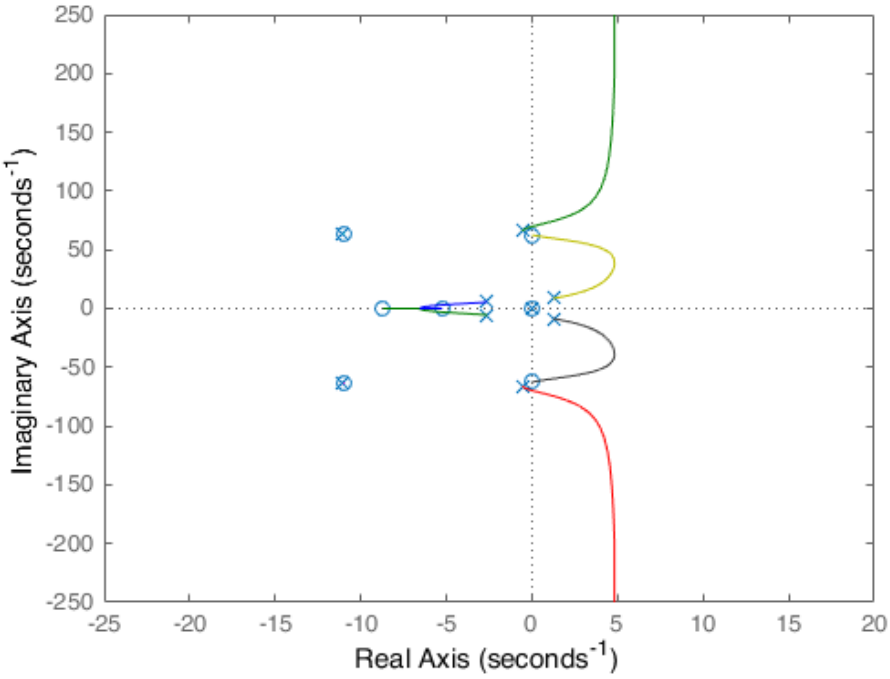

Figure 5.4: Root locus of the open-loop transfer function between control input (actuator) and sprung mass acceleration with an additional pole at the origin

The above figure shows that there are always closed-loop poles at the open right half-plane with the integral term either. As a result of the root locus method, it can be concluded that the PID controller is not a sufficient control method for the active suspension system driven by a linear electric motor with these parameter values.

5.2 State Feedback Control

When applying full-state feedback controllers, it is assumed that the linear plant written in state-space form $\dot{x} = Ax + Bu$ and all states, x, are available for the controller. If some states are not measured, they should be estimated; in this study, Kalman Filter is used for this purpose. The feedback gain matrix K, is implemented as

$$u = -K(x - x_{desired}) \tag{5.7}$$

and systems dynamics has become

$$\dot{x} = (A - BK)x + BKx_{desired}. \tag{5.8}$$

The controllability of the system should be checked first. The controllability matrix given in Equation 5.9 should be full rank for a controllable system [26].

$$rank[B|AB|\cdots|A^{n-1}B] = n \tag{5.9}$$

The system matrices given in Chapter 2.1.1 are used, and it is checked that system is controllable.

5.2.1 Linear Quadratic Regulator

The aim of LQR based optimal control is obtaining a state feedback K, such that a cost function expressed in terms of states and input are minimized. For this purpose, a quadratic cost function is described in Equation 5.10:

$$J = \frac{1}{2}x^T(t_f)S(t_f)x(t_f) + \int_{t_0}^{t_f} \frac{1}{2}\overbrace{[x^T(t)Qx(t) + u^T(t)R(t)u(t)]}^{L(x,u)}\,dt \tag{5.10}$$

The Hamiltonian is defined as:

$$\begin{aligned} H(t) &= \frac{1}{2}(x^TQx + u^TRu) + \lambda^T(Ax + Bu) \\ \dot{x} &= \frac{\partial H}{\partial \lambda} = Ax + Bu \\ -\dot{\lambda} &= \frac{\partial H}{\partial x} = Qx + A^T\lambda \\ 0 &= \frac{\partial H}{\partial u} = Ru + \lambda^T B \Longrightarrow u = -R^{-1}B^T\lambda \end{aligned} \tag{5.11}$$

Guess the form of the solution,

$$\begin{aligned} \lambda(t) &= P(t)x(t) \\ \dot{\lambda} = \dot{P}x + P\dot{x} &= \dot{P}x + P(Ax - BR^{-1}B^TP)x \\ -\dot{P}x - PAx + PBR^{-1}BPx &= Qx + A^TPx \end{aligned} \tag{5.12}$$

The formulation above (Equation 5.12) is satisfied if we can find $P(t)$ such that

$$-\dot{P} = PA + A^T P - PBR^{-1}Px + Q \tag{5.13}$$

The ODE derived is called *Algebraic Riccati Equation* (ARE). After solving this equation for $P(t)$ the control law

$$u = -Kx = -R^{-1}B^T P(t)x \tag{5.14}$$

can be applied.

5.2.1.1 Determination of LQR Weightings

The most straightforward choice on LQR weightings are $Q = I_{8\times 8}$ and $R = \rho$ then

$$L(x,u) = \|x\|^2 + \rho\|u\|^2 \tag{5.15}$$

By varying the parameter ρ performance can be tuned.

Using output weightings is a common method; choose output you want to keep small by letting $z = Hx$. Then,

$$Q = H^T H \; and \; R = \rho \tag{5.16}$$

But none of these methods give optimal solutions to the quadratic cost function, J. Optimization methods described in the next chapter are used, and J is minimized to get optimal solutions. By solving the optimization problem, the RMS value of SMA is minimized.

$$Q = \begin{bmatrix} q_1 & \cdots & 0 \\ \vdots & \ddots & \vdots \\ 0 & \cdots & q_8 \end{bmatrix}_{8\times 8} \tag{5.17}$$

In the optimization algorithm, $Q(8 \times 8)$ is taken as a diagonal weighting matrix and quadratic function, J is optimized with 8 parameters. Input weighting matrix R is not optimized, and it is taken close to zero for utilization of the linear motor force as much as possible. Actuator limits are set as constraints of optimization functions. In

addition to force limitation, real parts of the eigenvalues of the controlled system are restricted to be negative.

Also, ride comfort boundaries explained in Chapter 4.4.1 are set as constraints of the optimization problem. PSD values of SMA are used in the process; therefore, boundaries in Figure 4.4 are used. The 8-hours comfort boundary line is set as a constraint for both GA and GD, but if the algorithm is not providing a solution, constraints are reduced to 4-hours and 1-hour boundary lines with an order.

Table 5.1: Determined state feedback gains with optimization

	GA	GD
k_1	-1761.321	-2342.069
k_2	927.835	9960.586
k_3	1809.082	1398.909
k_4	-0.594	-18.452
k_5	-18.860	-22.500
k_6	53.909	-1474.136
k_7	5605.126	6587.228
k_8	1794.025	2388.623

5.3 H_∞ Control Method

In this work, two different H_∞ control methods are presented. In the finite frequency case, the approach in [19] is used, and the frequency range between 4 Hz and 8 Hz, which is the most is the critical frequency range for human body ride comfort, is considered for optimization. In the other case, the entire frequency case, the classical H_∞ controller is used. In both cases, limits of suspension deflection and wheel travel and also maximum force limit of the actuator, F_r, are taken as constraints.

Standard design procedure of H_∞ control is followed, and state-space is structured such that the system is represented as the combination of controlled outputs, z_1, and constrained outputs, z_2. Controlled outputs are sprung mass and pitch acceleration.

$$z_1 = C_1 x + D_1 F_r \tag{5.18}$$

where

$$C_1 = \begin{bmatrix} 0 & 0 & \frac{2k_{sf}}{M_s} & \frac{2k_{sr}}{M_s} & \frac{2c_f}{M_s} & \frac{2c_r}{M_s} & \frac{2(ac_f - bc_r)}{M_s} + V_x & \frac{-2(c_f + c_r)}{M_s} \\ 0 & 0 & \frac{-2ak_{sf}}{I_{yy}} & \frac{2bk_{sr}}{I_{yy}} & \frac{-2ac_f}{I_{yy}} & \frac{2bc_r}{I_{yy}} & \frac{-2(a^2c_f + b^2c_r)}{I_{yy}} & \frac{2(ac_f - bc_r)}{I_{yy}} \end{bmatrix}$$

$$D_1 = \begin{bmatrix} \frac{1}{M_s} \\ \frac{b}{I_{yy}} \end{bmatrix} \tag{5.19}$$

The three constrained outputs are the suspension deflection, which is bounded by its physical limit, $x_{3,4max}$, dynamic tire loads are set such that they do not exceed static ones. This assumption is made considering cruising at a constant speed with no steering, braking or acceleration. Also, the pitch rate is taken as constrained output, $x_{7\max}$, because, while minimizing sprung mass acceleration, pitch rate should be limited for ride comfort and stability of the vehicle. Thus, the constrained outputs vector is represented as

$$z_2 = C_2 x + D_2 F_r \tag{5.20}$$

where

$$C_2 = \begin{bmatrix} \frac{k_t}{\frac{M_s g b}{l} + mg} & 0 & 0 & 0 & 0 & 0 & 0 & 0 \\ 0 & \frac{k_t}{\frac{M_s g a}{l} + mg} & 0 & 0 & 0 & 0 & 0 & 0 \\ 0 & 0 & \frac{1}{x_{3,4max}} & 0 & 0 & 0 & 0 & 0 \\ 0 & 0 & 0 & \frac{1}{x_{3,4max}} & 0 & 0 & 0 & 0 \\ 0 & 0 & 0 & 0 & 0 & 0 & \frac{1}{x_{7max}} & 0 \end{bmatrix} \quad (5.21)$$

$$D_2 = \begin{bmatrix} 0 \\ 0 \\ 0 \\ 0 \\ \frac{1}{M_s a_{zmax}} \end{bmatrix}$$

And it can be written that:

$$|z_2(t)| \leq 1 \quad (5.22)$$

The new structure of state-space can be expressed as:

$$\begin{aligned} \dot{x}(t) &= \bar{A}x + Gw(t) \\ z_1(t) &= \bar{C}_1 x(t) \\ z_2(t) &= \bar{C}_2 x(t) \end{aligned} \quad (5.23)$$

where $\bar{A}$= A+BK and $\bar{C}_1$= C_1+D_1K, $\bar{C}_2$= C_2+D_2K

5.3.1 Entire Frequency Case

By solving LMIs below (Equation 5.24), H_∞ norm of the closed-loop transfer function from the road disturbance $w(t)$ to the controlled output $z_1(t)$ can be kept bounded, $\left\|T_{z_1 w}\right\|_\infty < \gamma$, while constraints are satisfied [18].

$$\begin{bmatrix} sym(A\bar{P}+B\bar{K}) & \text{G} & * \\ * & \text{-}\gamma^2 I & 0 \\ C_1\bar{P}+D_1\bar{K} & 0 & \text{-I} \end{bmatrix} < 0$$

$$\begin{bmatrix} -\bar{P} & * \\ \sqrt{\rho}(C_2\bar{P}+D_2\bar{K}) & \text{-I} \end{bmatrix} < 0 \qquad (5.24)$$

$$\begin{bmatrix} -\bar{P} & \frac{\sqrt{\rho}}{F_{rmax}\bar{K}^T} \\ * & \text{-I} \end{bmatrix} < 0$$

The proofs of LMIs in Equation 5.24 are given in Appendix C.

By solving these LMIs using the LMI toolbox of MATLAB, the desired state feedback gain K is obtained.

5.3.2 Finite Frequency Case

In the second part of the H_∞ control problem, instead of minimizing the disturbance effect on ride comfort at the whole frequency range, focused at a finite frequency range that is the most important ride comfort band for the human body. For developing an H_∞ controller in a finite frequency range, the Kalman Yakubovich Popov Lemma is used.

Kalman Yakubovich Popov Lemma: Let real scalars $\omega_1 \leq \omega_2$, matrices $A \in C^{nxn}$, $B \in C^{nxm}$ and a Hermitian matrix $\Theta \in C^{(n+m)x(n+m)}$ be given. Then the following statements are equivalent:

i. The finite frequency condition

$$\begin{bmatrix} (j\omega I - A)^{-1}B \\ I \end{bmatrix}^* \Theta \begin{bmatrix} (j\omega I - A)^{-1}B \\ I \end{bmatrix} < 0, \forall \omega_1 \leq \omega \leq \omega_2 \qquad (5.25)$$

holds

ii. There exists Hermitian matrices $P, Q \in C^{nxn}$ such that $Q > 0$ and

$$\begin{bmatrix} A & B \\ I & 0 \end{bmatrix}^* \begin{bmatrix} -Q & P + j\omega_c Q \\ P - j\omega_c Q & -\omega_1\omega_2 Q \end{bmatrix} \begin{bmatrix} A & B \\ I & 0 \end{bmatrix} + \Theta < 0 \qquad (5.26)$$

By solving LMIs below, H_∞ norm of the closed-loop transfer function from the road disturbance $w(t)$ to the controlled output $z_1(t)$ is asymptotically stable and $\left\|T_{z_1 w}\right\|_\infty < \gamma$, while constraints are satisfied in the finite frequency range.

$$\begin{bmatrix} -[\bar{F}]_S & A\bar{F} + B\bar{K} + \bar{P}_1 & \bar{F} & G \\ * & -\bar{P}_1 & 0 & 0 \\ * & * & -\bar{P}_1 & 0 \\ * & * & * & -\eta I \end{bmatrix} < 0$$

$$\begin{bmatrix} -\bar{Q} & \bar{P} + j\omega_c\bar{Q} - \bar{F}^T & 0 & 0 \\ * & -\omega_1\omega_2\bar{Q} + [A\bar{F} + B\bar{K}]_S & G & \bar{F}^T C_1^T + \bar{K}^T D_1^T \\ * & * & -\gamma^2 I & 0 \\ * & * & * & -I \end{bmatrix} < 0 \qquad (5.27)$$

$$\begin{bmatrix} -I & \sqrt{\rho}C_2\overline{F} \\ * & -\overline{P_1} \end{bmatrix} < 0$$

where $\omega_c = (\omega_1 + \omega_2)/2$.

Note that the matrices in inequalities (5.27) are defined as:

$$\begin{aligned} \bar{Q} &= (F^{-1})^T Q F^{-1} \\ \bar{P} &= (F^{-1})^T P F^{-1} \\ \bar{P}_1 &= (F^{-1})^T P_1 F^{-1} \\ \bar{K} &= K F^{-1} \\ \bar{F} &= F^{-1} \end{aligned} \qquad (5.28)$$

Given LMIs in Equation 5.27 are proved by referring to [19],[28],[29] they are given in Appendix D.

Table 5.2: Selected feedback gains with finite and infinite frequency H_∞ controllers

	Entire frequency (K_1)	Finite frequency (K_2)
k_1	118973	65256
k_2	69555	-538.2
k_3	549554	11240
k_4	160628	-39204
k_5	-3554	-1937.1
k_6	-45.1	-17.1
k_7	108538	-11258
k_8	-296502	-5340

With the H_∞ controller gains in Table 5.2, the PSD of SMA is obtained. The closed-loop transfer functions of the system for both of the H_∞ controller gains are squared and multiplied with PSD of random road input for road class F in Table 2.2. Hence, RMS plots in Figure 5.4 are observed for finite frequency and entire frequency H_∞ controllers.

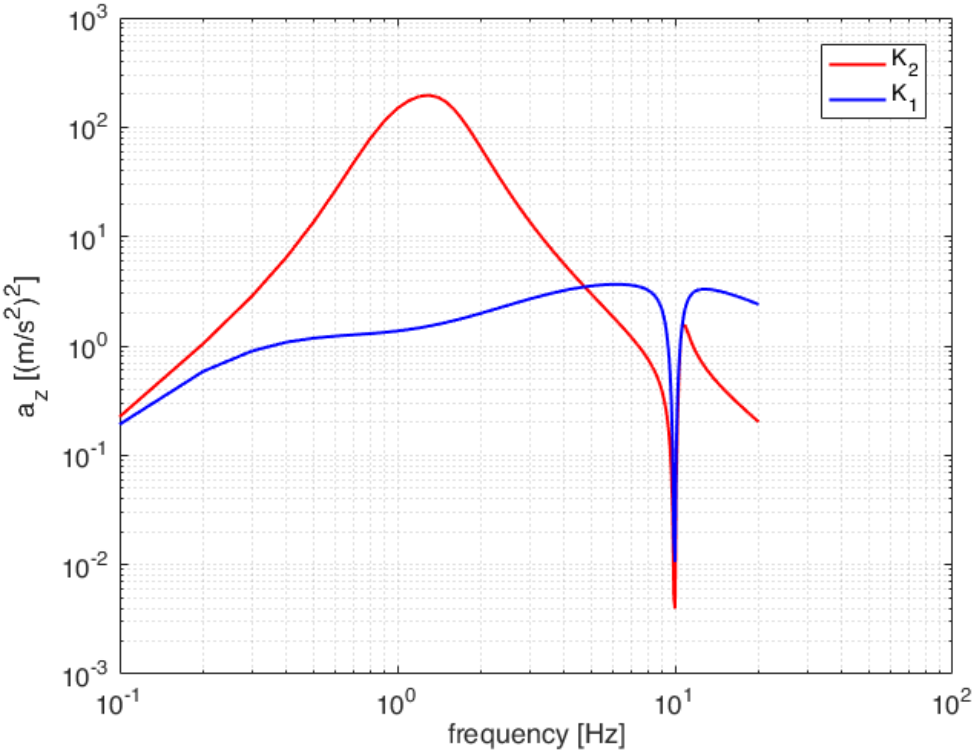

Figure 5.5: PSD of SMA for the H_∞ controllers with gains K_1 and K_2

The above PSD plot for H_∞ controllers shows that until 4 Hz controller with gain K_1 (blue line) has better performance than the controller with gain K_2 but after 4 Hz K_2 (red line) has better performance. If the real-time spectrum of SMA can be calculated, switching the controller gains with respect to the dominant frequency range is possible. This idea is later discussed in Chapter 6.3.

5.4 Optimal Sliding Mode Controller

In the sliding mode control, trajectories are forced to reach a sliding manifold (sliding surface) in the finite time and stay on the manifold for all future time.

By using the given half-car model in Chapter 2.1., sprung mass acceleration can be expressed as,

$$\frac{2k_{sf}}{M_s}x_3 + \frac{2k_{sr}}{M_s}x_4 + \frac{2c_f}{M_s}x_5 + \frac{2c_r}{M_s}x_6 + \left(\frac{2(ac_f - bc_r)}{M_s} + V_x\right)x_7 - \frac{2(c_f + c_r)}{M_s}x_8 + \frac{1}{M_s}u = \ddot{z}_s \tag{5.29}$$

Let's express the sliding surface as:

$$S = K_a x \tag{5.30}$$

where K_a is the sliding surface coefficient vector, and x is the system states.

For the application of optimal sliding mode control, weighting matrix Q necessary. The weighting parameters are defined for wheel travel, suspension deflection, pitch rate and sprung mass velocity.

$$Q = \begin{bmatrix} \delta_1 & 0 & 0 & 0 & 0 & 0 & 0 & 0 \\ 0 & \delta_1 & 0 & 0 & 0 & 0 & 0 & 0 \\ 0 & 0 & \delta_2 & 0 & 0 & 0 & 0 & 0 \\ 0 & 0 & 0 & \delta_2 & 0 & 0 & 0 & 0 \\ 0 & 0 & 0 & 0 & 0 & 0 & 0 & 0 \\ 0 & 0 & 0 & 0 & 0 & 0 & 0 & 0 \\ 0 & 0 & 0 & 0 & 0 & 0 & \delta_3 & 0 \\ 0 & 0 & 0 & 0 & 0 & 0 & 0 & \delta_4 \end{bmatrix} \tag{5.31}$$

The transformation matrix for application of sliding mode control is taken as I_{8x8} matrix; thus, transformed A and Q matrices do not change.

Define the following matrices:

$$\begin{aligned} A_{11} &= A_{(1:7),(1:7)} \\ A_{12} &= A_{(1:7),8} \\ Q_{11} &= Q_{(1:7),(1:7)} \\ Q_{12} &= Q_{(1:7),8} \\ Q_{22} &= Q_{8,8} \end{aligned} \tag{5.32}$$

and obtaining the solution of the following matrix Riccati equation for the above matrices:

$$(PA_{11})^T + PA_{11} + Q_{11} - (PA_{12} + Q_{12})Q_{22}^{-1}(PA_{12} + Q_{12})^T = 0 \tag{5.33}$$

The sliding surface coefficient can be expressed as:

$$K_a = [Q_{22}^{-1}(A_{12}^T P + Q_{12}^T)] \tag{5.34}$$

In sliding mode control, it is necessary to check the Lyapunov function given in Equation 5.48, which ensures the stability of the system for obtaining control input.

$$V = \frac{1}{2}S^2 \tag{5.35}$$

To ensure stability time rate of change of Lyapunov function (V) should be smaller than $-\varepsilon|S|$ where ε is a positive constant.

$$\dot{V} = S\dot{S} = S\begin{pmatrix} K_a(1)\dot{x}_1 + K_a(2)\dot{x}_2 + K_a(3)\dot{x}_3 + K_a(4)\dot{x}_4 + K_a(5)\dot{x}_5 \\ +K_a(6)\dot{x}_6 + K_a(7)\dot{x}_7 + K_a(8)\dot{x}_8 \end{pmatrix} \tag{5.36}$$

For stability, the following inequality can be written:

$$S\begin{pmatrix} K_a(1)\dot{x}_1 + K_a(2)\dot{x}_2 + K_a(3)\dot{x}_3 + K_a(4)\dot{x}_4 + K_a(5)\dot{x}_5 + K_a(6)\dot{x}_6 \\ +K_a(7)\dot{x}_7 + K_a(8)\dot{x}_8 \end{pmatrix} \leq -\varepsilon|S| \tag{5.37}$$

Substitute state equations into Equation 5.50.

$$\dot{V} = S\begin{Bmatrix} K_a(1)\left(-x_5 + \dot{z}_{0f}\right) + K_a(2)(-x_6 + \dot{z}_{0r}) + K_a(3)(x_5 + ax_7 - x_8) + K_a(4)(x_6 - bx_7 - x_8) \\ +K_a(5)\left(\frac{k_t}{m}x_1 - \frac{k_{sf}}{m}x_3 - \frac{c_f}{m}x_5 - \frac{ac_f}{m}x_7 + \frac{c_f}{m}x_8\right) \\ +K_a(6)\left(\frac{k_t}{m}x_2 + \frac{k_{sf}}{m}x_3 + \frac{c_f}{m}x_5 + \left(\frac{ac_f}{m} + \frac{M_s V_x}{2m}\right)x_7 - \frac{c_f}{m}x_8 - \frac{1}{2m}u\right) \\ +K_a(7)\left(\frac{-2k_{sf}(a+b)}{I_{yy}}x_3 - \frac{2c_f(a+b)}{I_{yy}}x_5 - \left(\frac{2ac_f(a+b)}{I_{yy}} + \frac{bM_s V_x}{I_{yy}}\right)x_7 + \frac{2c_f(a+b)}{I_{yy}}x_8 + \frac{b}{I_{yy}}u\right) \\ +K_a(8)\left(\frac{2k_{sf}}{M_s}x_3 + \frac{2k_{sr}}{M_s}x_4 + \frac{2c_f}{M_s}x_5 + \frac{2c_r}{M_s}x_6 + \left(\frac{2c_f(a-b)}{M_s} + V_x\right)x_7 - \frac{2(c_f + c_r)}{M_s}x_8 + \frac{1}{M_s}u\right) \end{Bmatrix} \tag{5.38}$$

Rearrange Equation 5.51 as:

$$\begin{aligned} \dot{V} = S\Bigg\{ & \frac{-K_a(5)k_t}{m}x_1 - \frac{K_a(6)k_t}{m}x_2 - \left(\frac{-K_a(5)k_{sf}}{m} + \frac{K_a(6)k_{sf}}{m} - \frac{2K_a(7)k_{sf}(a+b)}{I_{yy}}\right)x_3 \\ & - \left(-K_a(1) + K_a(3) - \frac{K_a(5)c_f}{m} + \frac{K_a(6)c_f}{m} - \frac{2K_a(7)c_f(a+b)}{I_{yy}}\right)x_4 \\ & - \left(-K_a(2) + K_a(4)\right)x_6 \\ & - \left(aK_a(3) - bK_a(4) - \frac{aK_a(5)c_f}{m} + \frac{aK_a(6)c_f}{m} + \frac{K_a(6)M_s V_x}{2m} - \frac{2aK_a(7)c_f(a+b)}{I_{yy}}\right. \\ & \left. - \frac{K_a(7)bM_s V_x}{I_{yy}}\right)x_7 - \left(-K_a(3) - K_a(4) + \frac{K_a(5)c_f}{m} - \frac{K_a(6)c_f}{m} + \frac{2K_a(7)c_f(a+b)}{I_{yy}}\right)x_8 \\ & + \left(\frac{1}{M_s} + \frac{b}{Iyy} - \frac{1}{2m}\right)u\Bigg\} \end{aligned} \tag{5.39}$$

By using Equation 5.52, control input (u) is written as with estimated states:

$$
\begin{aligned}
u = \frac{-K}{\left(\frac{1}{M_S}+\frac{b}{I_{yy}}-\frac{1}{2m}\right)}\Bigg(&sign(S)\\
&+\left[\frac{-K_a(5)k_t}{m}\hat{x}_1-\frac{K_a(6)k_t}{m}\hat{x}_2-\left(\frac{-K_a(5)k_{sf}}{m}+\frac{K_a(6)k_{sf}}{m}-\frac{2K_a(7)k_{sf}(a+b)}{I_{yy}}\right)\hat{x}_3\right.\\
&-\left(-K_a(1)+K_a(3)-\frac{K_a(5)c_f}{m}+\frac{K_a(6)c_f}{m}-\frac{2K_a(7)c_f(a+b)}{I_{yy}}\right)\hat{x}_5-\left(-K_a(2)+K_a(4)\right)\hat{x}_6\\
&-\left(aK_a(3)-bK_a(4)-\frac{aK_a(5)c_f}{m}+\frac{aK_a(6)c_f}{m}+\frac{K_a(6)M_sV_x}{2m}-\frac{2aK_a(7)c_f(a+b)}{I_{yy}}\right.\\
&\left.\left.-\frac{K_a(7)bM_sV_x}{I_{yy}}\right)\hat{x}_7-\left(-K_a(3)-K_a(4)+\frac{K_a(5)c_f}{m}-\frac{K_a(6)c_f}{m}+\frac{2K_a(7)c_f(a+b)}{I_{yy}}\right)\hat{x}_8\right]\Bigg)
\end{aligned}
\tag{5.40}
$$

Then following expression satisfies stability:

$$
S\left\{\begin{array}{c}
\frac{K_a(5)k_t}{m}(x_1-\hat{x}_1)+\frac{K_a(6)k_t}{m}(x_2-\hat{x}_2)+\left(\frac{-K_a(5)k_{sf}}{m}+\frac{K_a(6)k_{sf}}{m}-\frac{2K_a(7)k_{sf}(a+b)}{I_{yy}}\right)(x_3-\hat{x}_3)\\
+\left(-K_a(1)+K_a(3)-\frac{K_a(5)c_f}{m}+\frac{K_a(6)c_f}{m}-\frac{2K_a(7)c_f(a+b)}{I_{yy}}\right)(x_5-\hat{x}_5)\\
+\left(-K_a(2)+K_a(4)\right)(x_6-\hat{x}_6)\\
+\left(aK_a(3)-bK_a(4)-\frac{aK_a(5)c_f}{m}+\frac{aK_a(6)c_f}{m}+\frac{K_a(6)M_sV_x}{2m}-\frac{2aK_a(7)c_f(a+b)}{I_{yy}}-\frac{K_a(7)bM_sV_x}{I_{yy}}\right)(x_7-\hat{x}_7)\\
+\left(-K_a(3)-K_a(4)+\frac{K_a(5)c_f}{m}-\frac{K_a(6)c_f}{m}+\frac{2K_a(7)c_f(a+b)}{I_{yy}}\right)(x_8-\hat{x}_8)\\
-Ksign(S)+K_a(1)\dot{z}_{0f}+K_a(2)\dot{z}_{0r}
\end{array}\right\}\leq-\varepsilon|S|
\tag{5.41}
$$

The errors between true states, x and estimated states $\hat{x}$ are neglected. And the control gain, K, is selected as below:

$$
K>\left(K_a(1)+K_a(2)\right)\dot{z}_{0_{max}}
\tag{5.42}
$$

Then it is proved that given Equation 5.57 satisfies the stability condition.

$$
\dot{V}\leq\varepsilon|S|
\tag{5.43}
$$

Table 5.3: Simulator parameters for optimal sliding mode controller

Simulator parameters	Values
δ_1 wheel travel weighting	30
δ_2 suspension deflection weighting	30
δ_3 pitch speed weighting	100
δ_4 sprung mass speed weighting	5
q covariance of the road profile [m^2/s^2]	0.076
r_1 rear unsprung mass accelerometer noise covariance [m^2/s^4]	0.4
r_2 pitch speed sensor noise covariance [rad^2/s^2]	0.0001
r_3 sprung mass accelerometer noise covariance [m^2/s^4]	0.001
τ sensor & controller sampling rate [ms]	10

CHAPTER 6

OPTIMIZATION OF CONTROLLERS

6.1 Trust-Region Algorithm

The trust-region method is one of the most important numerical optimization methods in solving nonlinear programming problems. It is a gradient-based algorithm and arises from Newton's Method. The trust-region method tries to minimize the quadratic cost function within a region around x_k [30]. In this work, the trust region algorithm is used for optimizing the weighting matrix, Q of LQR. Thus, x_k refers to diagonal elements of weighting matrix, Q and $f(x_k)$ refers to the quadratic cost function of LQR. Trust region algorithm tries to find a solution inside a trust region with a radius Δ_k around the point x_k. The 'fmincon' inside MATLAB Optimization Toolbox is used for realizing the trust-region algorithm. The initial point x_0 is set as zero matrix (8×1). The constraints are set as follows:

- Eigenvalues of the closed-loop system matrix, $A - BK$, should be on the open left half-plane.
- Calculated PSD of SMA should be under comfort boundary lines specified in Figure 4.4.
- The maximum actuator limit, 2150 N, should not be excessed.

Using these constraints and initial point, x_0, Trust-Region algorithm realized. The operation of Trust-Region algorithm is given in Appendix E. Although the trust-region algorithm 'fmincon' in MATLAB is a very fast and accurate solver for convex and twice continuous differentiable problems, the results depend strongly on the initial values and often fall into local minima. Also, it has the disadvantages of finding a minimum close to the starting point and the Hessian matrix close to the singular point.

Note that due to the Trust-region algorithm is gradient-based, GD is used to mean it.

6.2 Genetic Algorithm

Genetic Algorithms are essential for global search problems because rather than a single initial point, GAs are initialized with a population of initial guesses. This population is generally randomly chosen and will be spread through the search space. A typical algorithm includes [32] ;

- Selection or reproduction
- crossover
- mutation.

Like other optimization algorithms, GA begins with the definition of a cost function. Before the selection of the phase variables of the cost function, randomly chosen N_{pop} (number of initial population) with N_{bits}-bit chromosomes should be defined. The variable values are represented in binary; thus, continuous values should be quantized. Each l-bit gene represents a variable, and the length of chromosomes is determined by the number of genes that will be optimized.

$$\begin{gathered} N_{bits} = N_{var} \times l \\ chromosome = [p_1, p_2, p_3, \ldots, p_{N_{var}}] \end{gathered} \tag{6.1}$$

In the beginning, chromosomes can be obtained randomly.

$$population = round(rand(N_{pop} \times N_{bits})) \tag{6.2}$$

6.2.1 Selection

According to Darwin's natural selection, the survival chance of the fittest is higher in the population. In the algorithm, it means chromosomes have a lower cost, survive, and the rest are discarded. The chromosomes that survive to the next generation are selected with respect to the selection rate, X_{rate}. Taking X_{rate} small let is keeping only a few chromosomes, and it limits available genes. Taking X_{rate} high and

keeping too many chromosomes can cause bad performance. Often, X_{rate} is taken 0.5 [33] .

$$N_{keep} = N_{pop} \times X_{rate} \tag{6.3}$$

Now, kept population (N_{keep}) is a mating pool and random pairing takes place until the population reach N_{pop}. There are different pairing methods like bottom to top pairing or random pairing, but weighted random pairing works like natural selection. A chromosome with the lowest cost has the highest probability of pairing.

6.2.2 Crossover

Mating is the creation of offspring from the parents selected. A crossover point is chosen randomly between 1 and N_{bits} and crossover happens like in the figure below.

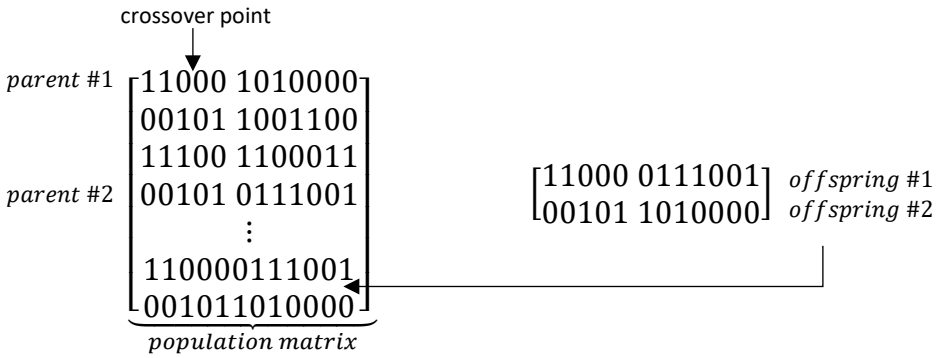

Figure 6.1: Selection and crossover schematic

6.2.3 Mutation

Mutations are randomly chosen between all bits ($N_{bits} \times N_{pop}$) with a mutation rate μ. But low-cost members of the population are not mutated; they are defined as *elite* solutions.

After mutations have been done, the next generation is obtained. At this point, it should be checked that an acceptable solution to the cost function is observed. If cost is not sufficient, the algorithm should return to the selection phase. The number of generations depends on whether the convergence is gathered or the maximum iteration number. If one of these situations is satisfied algorithm would be stopped.

Pseudocode for the process in GA is given in Figure 6.2. [33]

Algorithm: The Pseudo Code for GA

1. Set parameters will be optimized
2. Encode parameters
3. Generate initial population randomly
4. **while** i< *MaxIteration* **and** *BestFitness*<*MaxFitness* **do**
5. Selection
6. Crossover
7. Mutation
8. Fitness calculation
9. Decode the individual with maximum fitness
10. **return** the best solution

Figure 6.2: Pseudocode for a general GA

The problem optimized with GA is carried out a couple of times to get optimal result due to a randomly chosen initial population.

6.3 Real-Time Spectrum Analysis

In this study, real-time spectrum analysis is used for the application of H_∞ control. The idea is switching the controller gain at a specific frequency such that SMA is minimized. Designing a real-time spectrum analyzer should begin with introducing the discrete Fourier transform concept.

Discrete Fourier Transform (DFT) is a method for analyzing the Fourier representation of finite-length signals. DFT is used commonly for filtering and spectrum analysis in signal processing applications. One of the significant applications of the DFT is analyzing the frequency content of continuous-time signals. In the process of getting Fourier analysis with DFT, a continuous-time signal should be discretized and windowed. DFT operation is applied to the discretized and windowed signal. Windowing is necessary because of the finite-time requirement of DFT.

Discretization in the frequency domain,

$$X(e^{j\omega}) = \frac{1}{T}\sum_{r=-\infty}^{\infty} X_c(j\frac{\omega}{T} + j\frac{2\pi r}{T}) \tag{6.4}$$

Windowing with a window W in the frequency domain,

$$V(e^{j\omega}) = \frac{1}{2\pi}\int_{-\pi}^{\pi} X(e^{j\theta})\, W(e^{j(\omega-\theta)})d\theta \tag{6.5}$$

The discrete signal $x[n]$ should be multiplied with $w[n]$ in the time-domain; therefore, the periodic convolution operation above is necessary for the frequency domain. [36]

Computation of DFT,

$$V[k] = \sum_{n=0}^{N-1} v[n]\, e^{-j\frac{2\pi}{N}kn}, \qquad k = 0,1,\dots,N-1 \tag{6.6}$$

where,

$$V[k] = V(e^{j\omega})\big|_{\omega=\frac{2\pi k}{N}} \tag{6.7}$$

Window length L should be equal or smaller than DFT length N.

6.3.1 Fast Fourier Transform

The fast Fourier transform is a well-known and very efficient algorithm for calculating N-point DFT. Without the FFT algorithm, computing N-point DFT (Equation 6.11) requires N^2 arithmetic operations, but the FFT algorithm uses only $N \log N$ arithmetic operations. FFT is a re-expressed version of N point DFT, in terms of smaller DFTs of sizes N_1 and N_2 as $N = N_1 N_2$ [37]

The Equation 6.6 can be formulated again with FFT taking $n = n_1 N_2 + n_2$ and $k = k_1 + k_2 N_1$.

$$X[k] = \sum_{n_2=0}^{N_2-1} \left[\left(\sum_{n_1=0}^{N_1-1} x[n_1 N_2 + n_2]\, e^{-j\frac{2\pi}{N_1} k_1 n_1} \right) e^{-j\frac{2\pi}{N} k_1 n_2} \right] e^{-j\frac{2\pi}{N_2} k_2 n_2} \quad (6.8)$$

where $k_1, k_2 \ldots k_N = 0,1, \ldots , N-1$.

6.3.2 Time-Dependent Fourier Transform

While obtaining the DFT of a signal, it is assumed that the signal does not change with time. But in real life, signals (for example, speech, radar, or data communication signals) often change with time. If a signal does not change with time, window length, and window type will not be important; otherwise, these parameters should be decided. This situation leads to a time-dependent Fourier Transform.

Time-dependent Fourier transform of a signal $x[n]$ is

$$X[n, \lambda) = \sum_{m=-\infty}^{\infty} x[n + m] w[m] e^{-j\lambda m} \quad (6.9)$$

With this operation, $x[n]$ shifted through window sequence $w[n]$ and discrete-time Fourier transform of $x[n]$ is computed. The shifting operation should be arranged by considering the operation rate.

6.3.2.1 Window Properties

While choosing a window for time-dependent Fourier Transform, a few criteria are essential for effective transform.[36]

- One of them is narrow main lobes because they provide sharp transitions. It is a desirable property that Fourier transforms of signals are concentrated around $w = 0$
- Also, the second side lobe must be reduced in amplitude. Figure 6.3 shows the rectangular window has the narrowest main lobe, but the second lobe does not decrease enough.
- Side lobes diminished by tapering at the end of the window. Hann and Blackman windows in Figure 6.5 and Figure 6.7 satisfy the desired tapering.

Between Figure 6.3 and Figure 6.7, frequently used windows are represented in time and frequency domains.

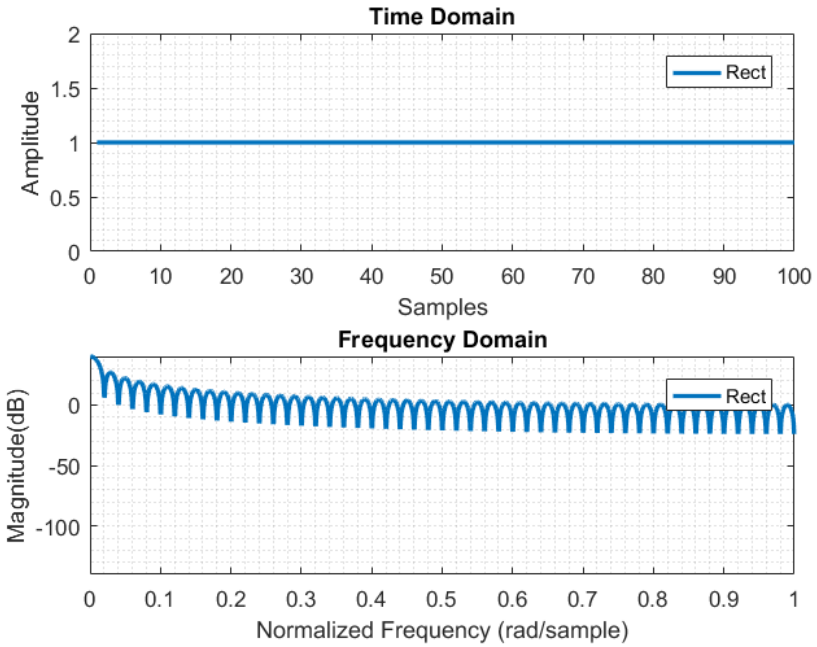

Figure 6.3: Rectangular window

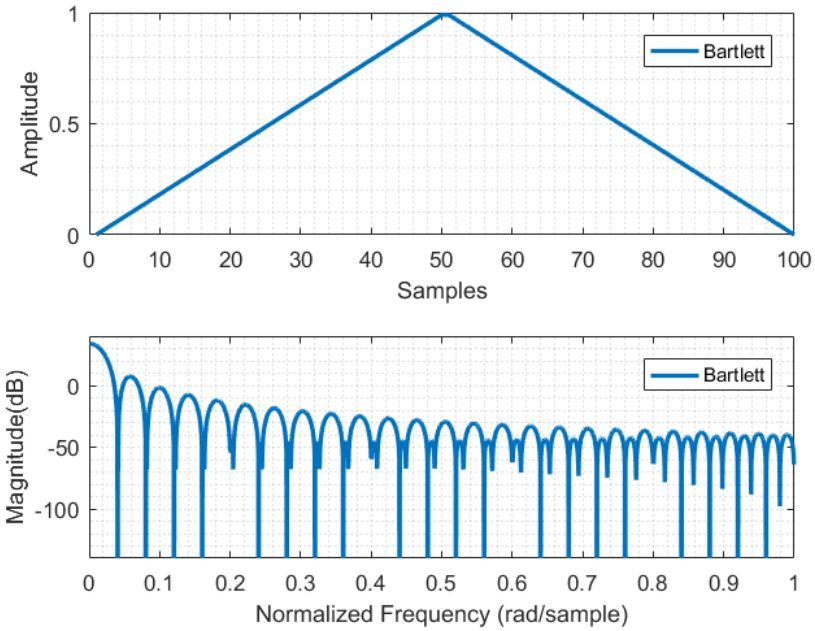

Figure 6.4: Barlett window

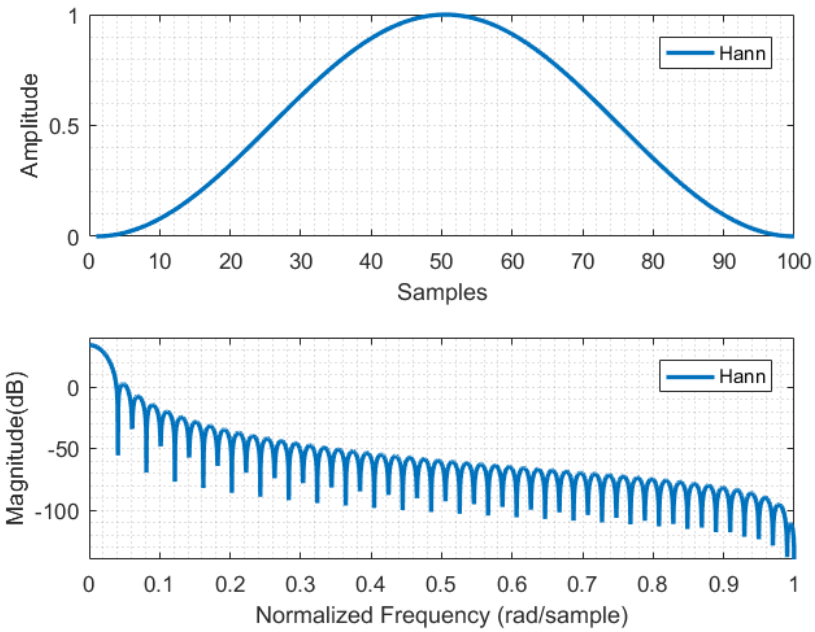

Figure 6.5: Hann window

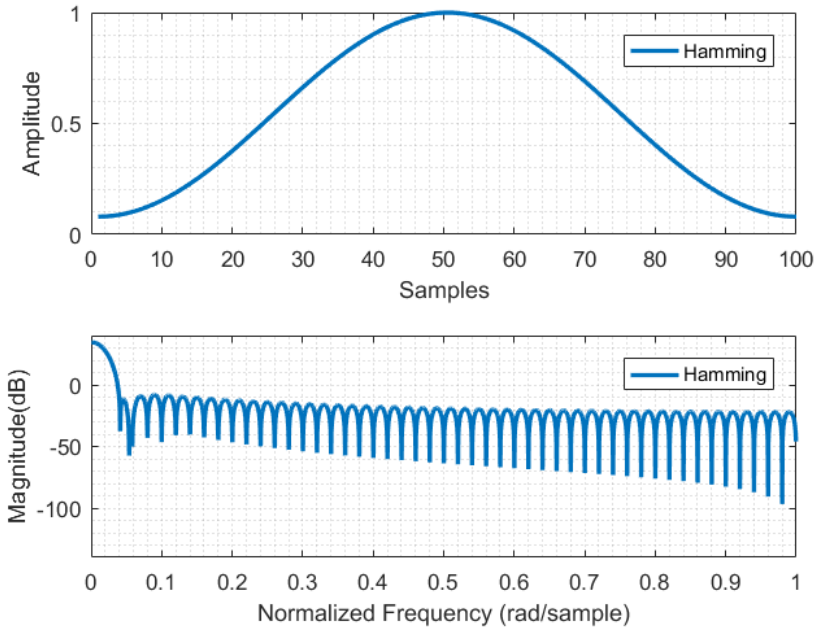

Figure 6.6: Hamming window

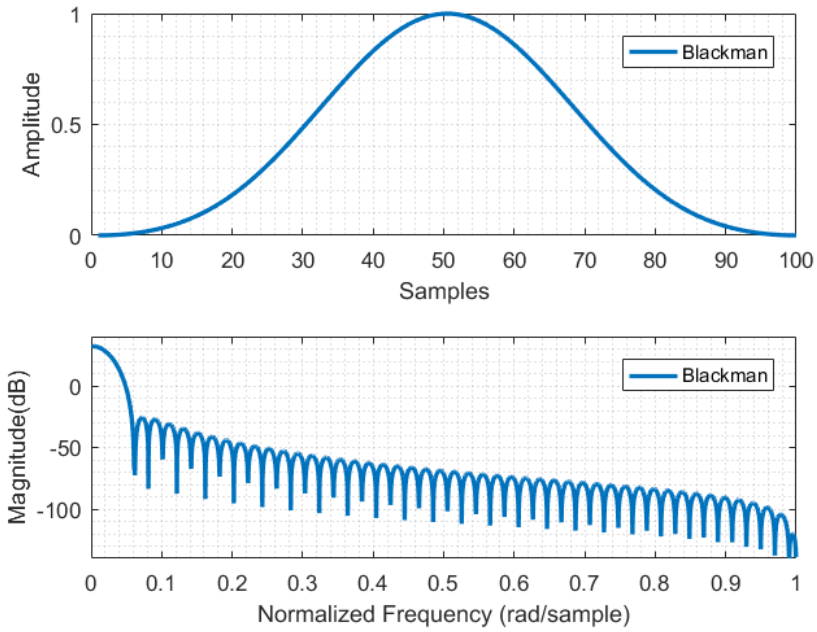

Figure 6.7: Blackman window

Using Hamming window time-dependent Fourier transform is applied on SMA of vehicle. H_∞ control method derived in Chapter 5.3 is applied based on the results of real-time spectrum analysis.

CHAPTER 7

TEST AND SIMULATION RESULTS

7.1 Results for Kalman Filter

For a realistic simulation environment, the sensors in a conventional passenger car (sprung mass and unsprung mass accelerometers, gyroscope for pitch rate) are modeled using real sensor rates, mean, and variances. Measurement noises are considered as zero-mean white noise. The used variances and sensor sampling rates in Kalman filter modeling are given in Table 3.1.

The discrete Kalman filter algorithm in Figure 3.2 is realized and using sensor outputs as an input of the Kalman filter, system states are estimated. The simulations are carried out with road class F given in Table 2.2.

The results for measured and estimated system states are given in Figure 7.1– Figure 7.5 below. These are front and rear wheel travels, suspension deflections, front and rear unsprung mass velocities, sprung mass velocity, and pitch speed.

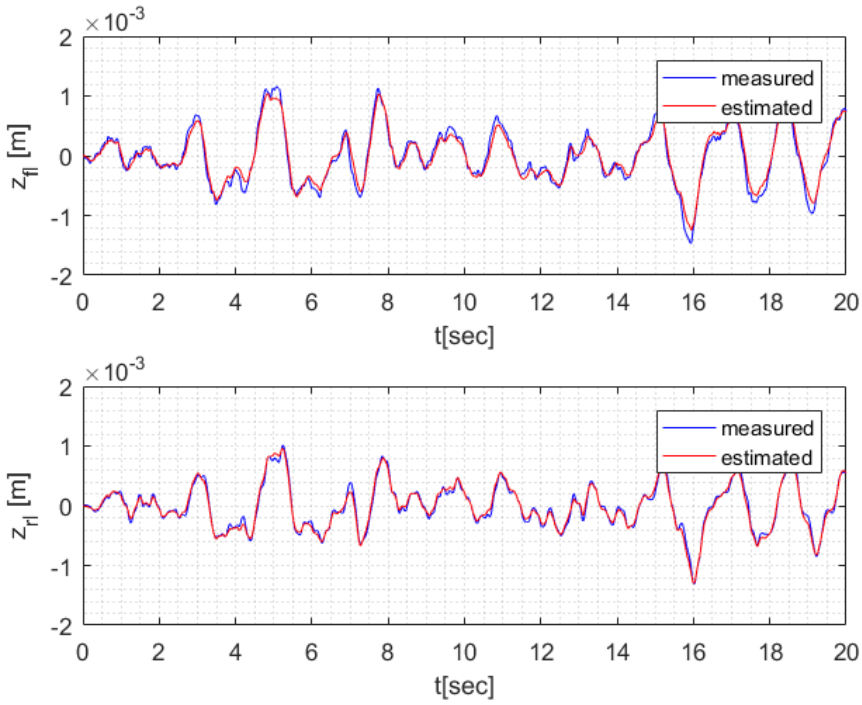

Figure 7.1: Measured and estimated front and rear wheel travels

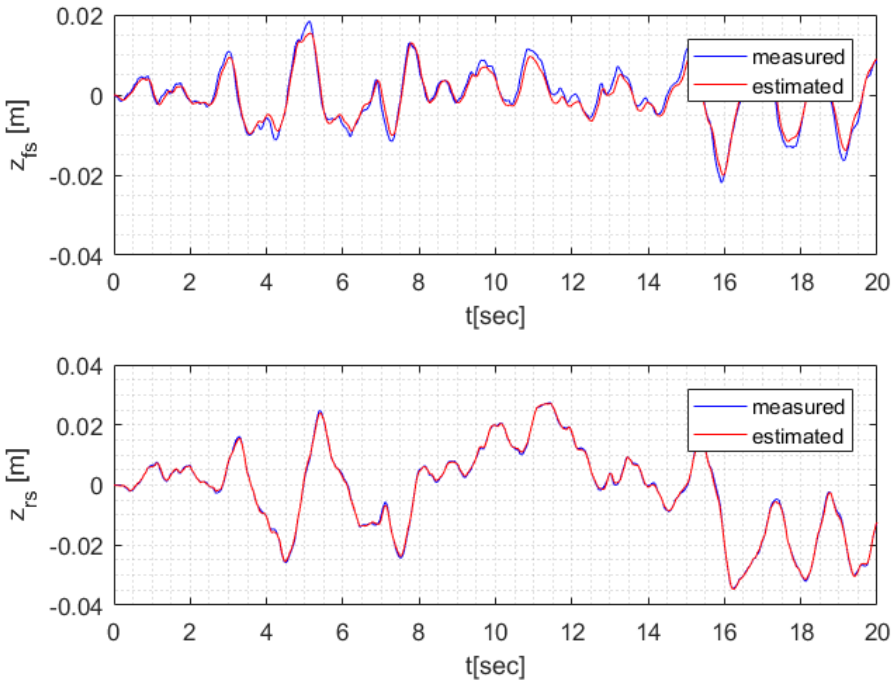

Figure 7.2: Measured and estimated front and rear suspension deflections

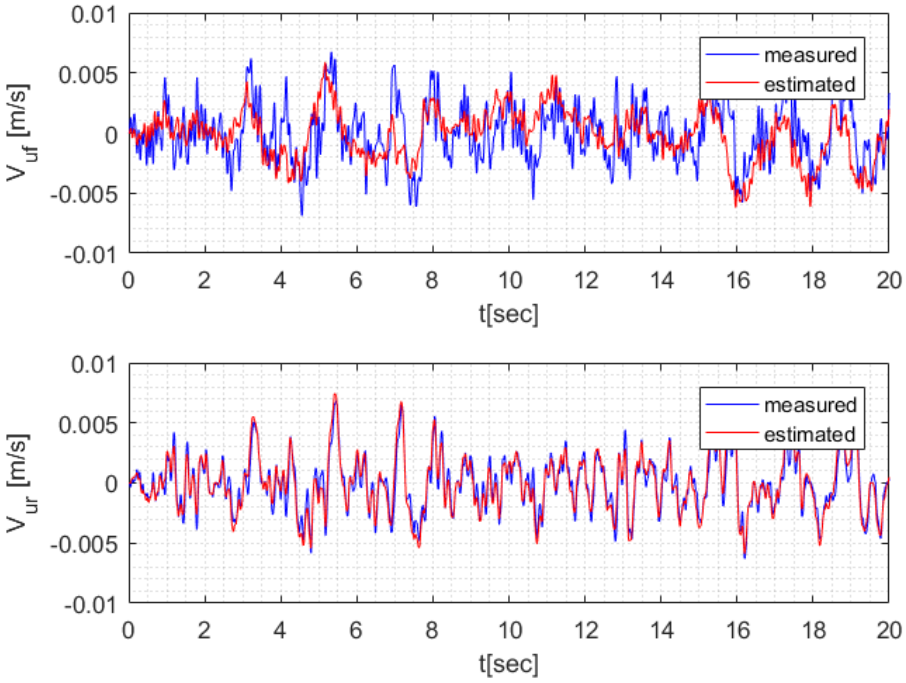

Figure 7.3: Measured and estimated front and rear unsprung mass velocities

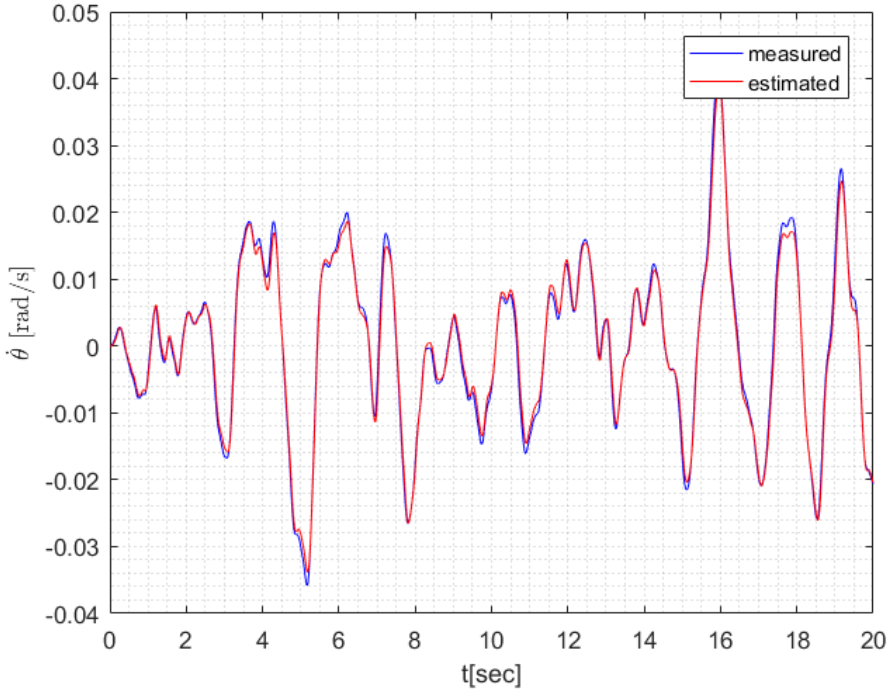

Figure 7.4: Measured and estimated pitch rates

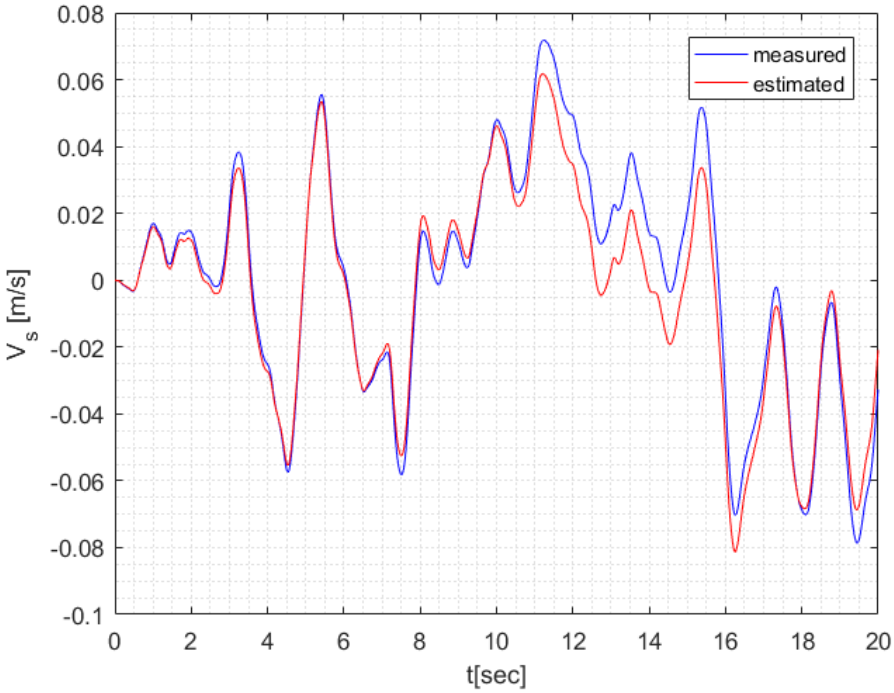

Figure 7.5: Measured and estimated sprung mass velocities

The plots for system states between Figure 7.1 and Figure 7.5 show that estimations with red lines follow the measured system states expressed with blue lines. But the time plots can be deceptive for performance evaluation of Kalman filter; for that reason, RMSE declared in Chapter 3.2.2 is used for statistical performance evaluation. As an example, in Figure 7.3, the measured and estimated front sprung mass velocities seem different, but error percentages only 0.225 %. The results given in Table 7.1 reveal that Kalman filter estimations are very accurate; the highest error percentage is 1.193 % for sprung mass velocity, and the rest of the states are estimated with an error below 1%.

Table 7.1: RMSE and error percentage table for Kalman filter performance evaluation

	RMSE ($\times 10^{-3}$)	Error Percentage (%)
front wheel travel	0.1001	0.010
rear wheel travel	0.0521	0.005
front suspension deflection	1.6389	0.164
rear suspension deflection	0.4408	0.044
front unsprung mass velocity	2.255	0.225
rear unsprung mass velocity	0.6886	0.069
pitch speed	1.2729	0.127
sprung mass velocity	11.9365	1.193

7.2 Simulation Results for Controllers

In this study, LQR, H_∞ and sliding mode controllers are developed, and simulations are performed with these controllers. One of the main goals of this study is improving ride comfort; hence SMA results are given for all controllers. But besides improving ride comfort, keeping wheel travel, suspension deflection, and pitch rate bounded is crucial for road holding; therefore, simulation results for these features are also presented. Suspension deflection and wheel travel are bounded by 0.05 m, and pitch rate is bounded with 0.2 rad/sec for the vehicle parameters used in this study (Table 2.1). Actuator forces for given controllers are added to observe the effect of the controller on a linear actuator.

In addition to time-domain simulation results, the ride comfort criteria is explained in Chapter 4.4.1. The frequency domain is used for performance evaluation. For frequency-domain assessment, the transfer function between SMA and road input is calculated and multiplied with a weighted frequency filter ($H(s)$) given in Equation 4.1. PSD of resulted transfer function multiplied with PSD of road input and SMA

in the frequency domain is obtained. The obtained SMA is plotted with comfort boundary lines in Figure 4.4.

7.2.1 LQR Control

The LQR is optimized with GA and GD based trust-region algorithm separately, and results are observed for the passive system, LQR optimized with GA and GD algorithms. Results are presented together to show the effectiveness of optimization algorithms.

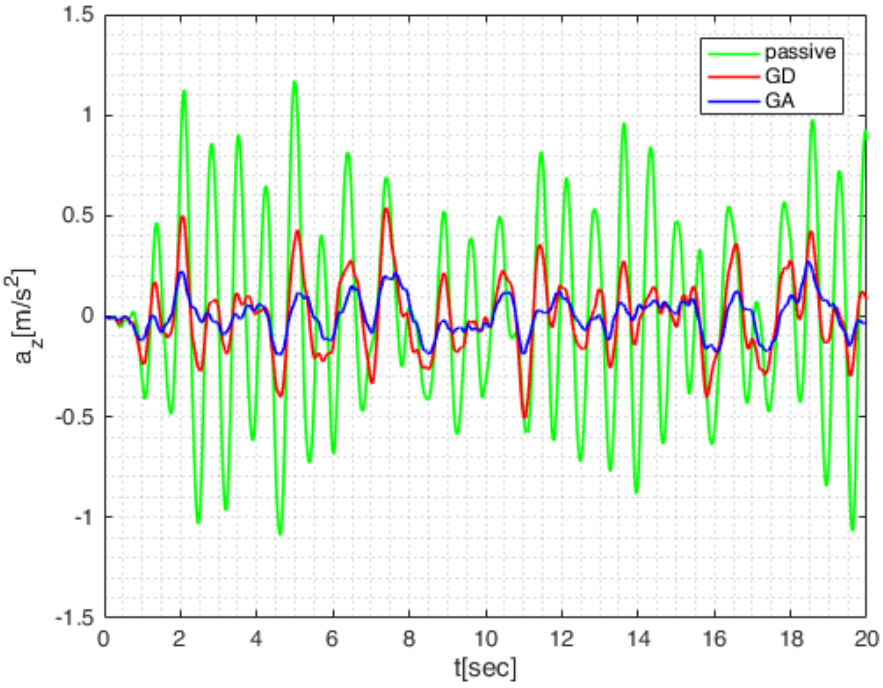

Figure 7.6: SMA values for passive system and LQR controller optimized with GA and GD

The above figure indicates that smaller SMA values are gathered with the LQR controller optimized with GA. Although GD based trust-region optimization algorithm is stuck into local minima, it still gives better results than passive suspension.

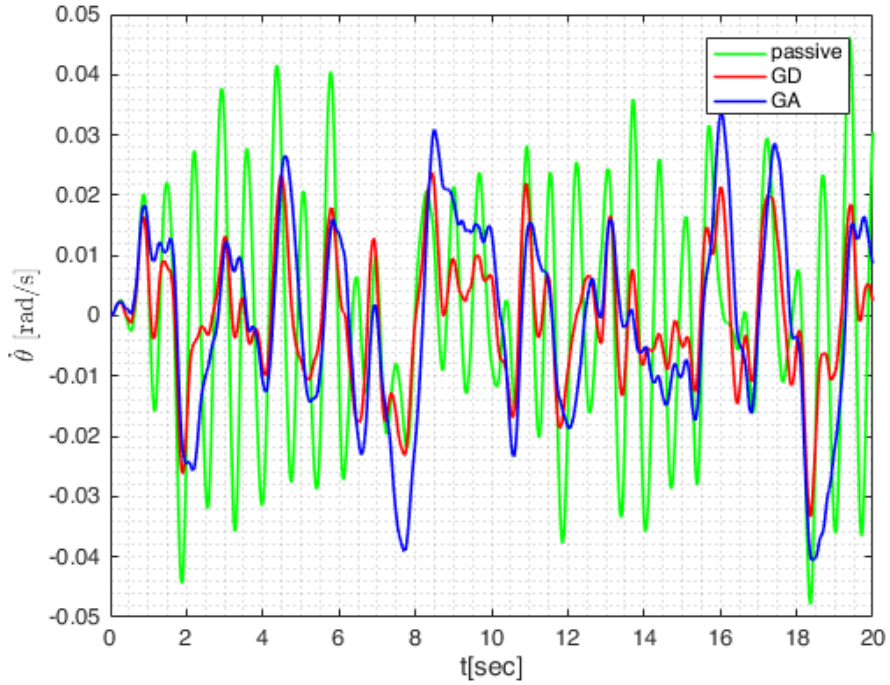

Figure 7.7: Pitch rate values for passive system and LQR controller optimized with GA and GD

The pitch rate ($\dot{\theta}$) boundary is acquired as 0.2 rad/sec for road handling and ride comfort. For three of the results in Figure 7.7, pitch rate is kept below the boundary.

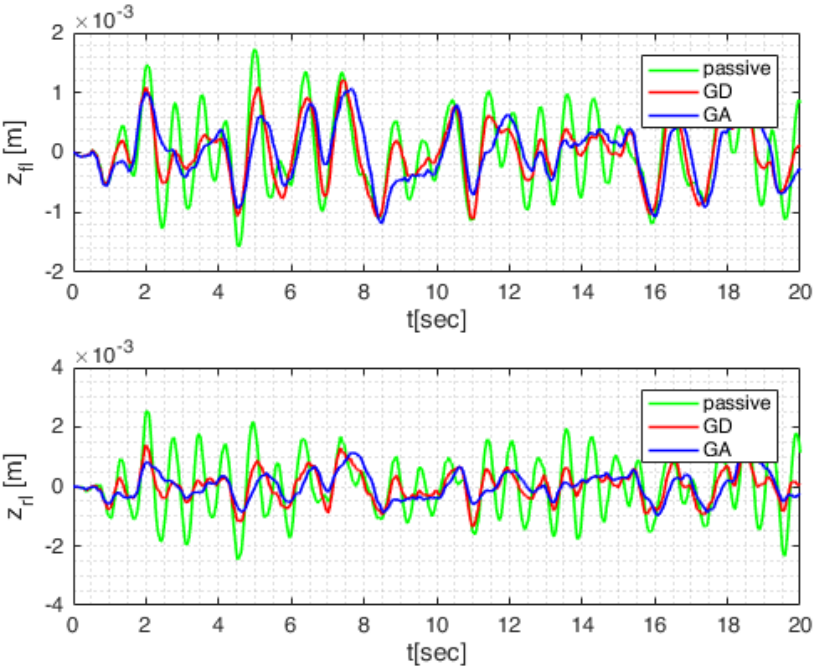

Figure 7.8: Front and rear wheel travels for passive system and LQR controller optimized with GA and GD

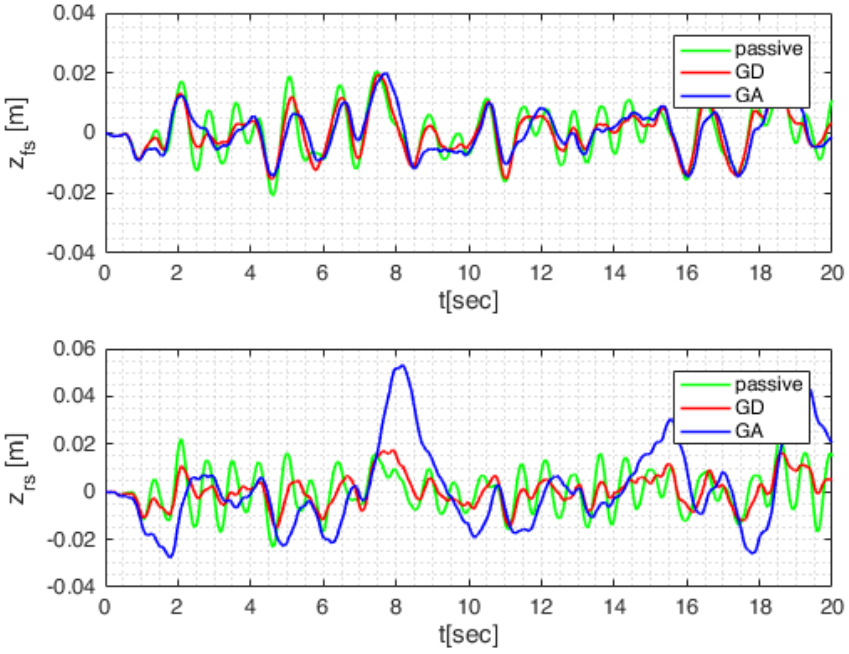

Figure 7.9: Front and rear suspension deflections for passive system and LQR controller optimized with GA and GD

Front and rear wheel travels and suspension deflections shown in Figure 7.8 and Figure 7.9 are below the maximum limits of deflections. Rear suspension deflection values are maximum for LQR optimized with GA rather than passive and GD cases. It is expected because, as it is mentioned in the introduction, ride comfort and road holding are conflicting parameters. Suspension deflection is related to the stability of the vehicle so, the main issue is keeping suspension deflection bounded, not minimizing, and for GA suspension deflections below 0.05 m.

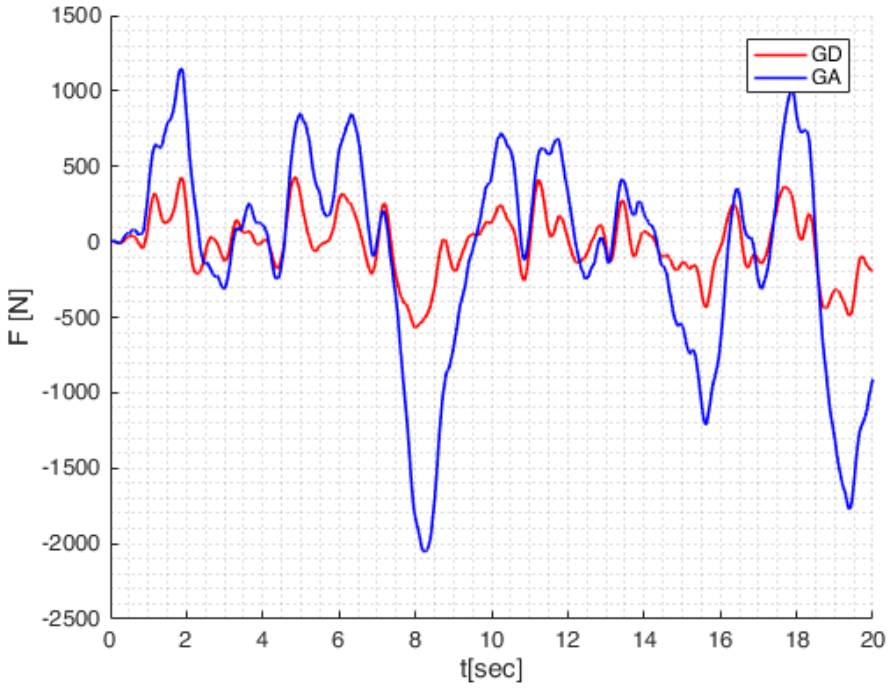

Figure 7.10: Total actuator force for LQR controller optimized with GA and GD

The linear motor can provide a maximum force of 2150 N [3]. Due to the half-car model, the maximum force limit is 4300 N. In the LQR optimized with GA, the linear actuator is more aggressive though it has better performance.

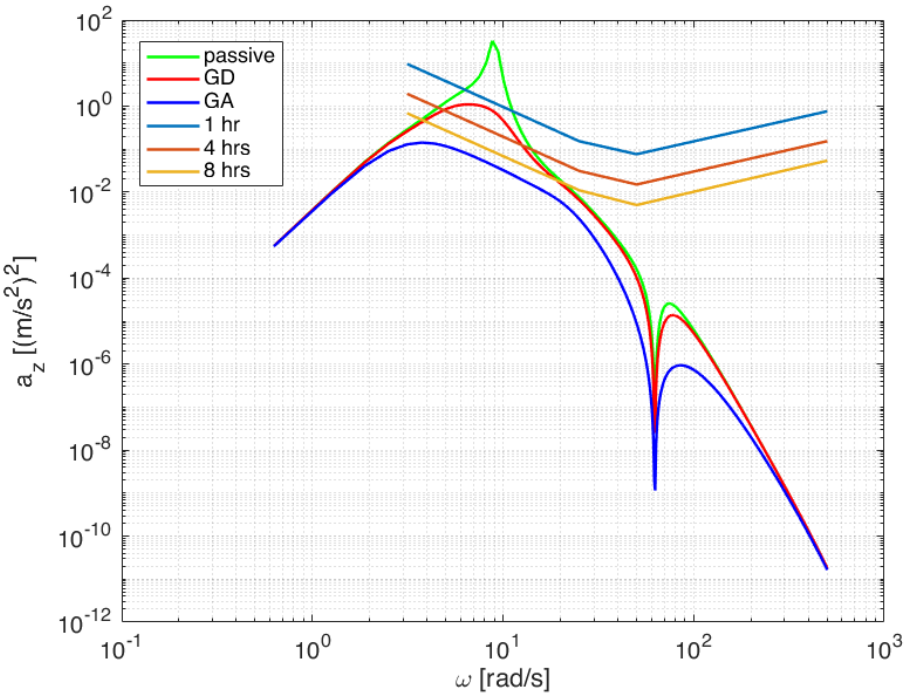

Figure 7.11: PSD of SMA for passive system and LQR controller optimized with GA and GD and comfort boundary lines for 1 hour, 4 and 8 hours

In the optimization algorithm, 1 hour, 4 hours and 8 hours (blue, orange and yellow lines in Figure 7.11 by order) comfort boundary lines are used as constraints of the optimization algorithm. A feasible solution could not be achieved with GD based trust-region algorithm for 4 hours and 8 hours comfort lines, but it is accomplished for 1-hour line. Due to the gradient nature of 'fmincon', it falls into a local minimum. The results with GA are better; 8 hours boundary line is satisfied while minimizing the cost function.

7.2.2 H_∞ Control

The structure of H_∞ control and derivations of necessary LMIs for both finite and infinite frequency H_∞ controllers are discussed in Chapter 5.3, and obtained state gains are given in Table 5.2.

Real-time spectrum analysis and obtained state gains are combined in simulation. The H_∞ the control part of the simulation is given in Appendix B. Dominant frequency range is determined with respect to frequency domain SMA results. K-selection block determines the dominant frequency range, and if it is smaller than 3 Hz, the gain, K_1, comes into play, but it is more than 3 Hz, K_2 is used. After appropriate control gain is selected, simulations are carried out until dominant frequency alternates.

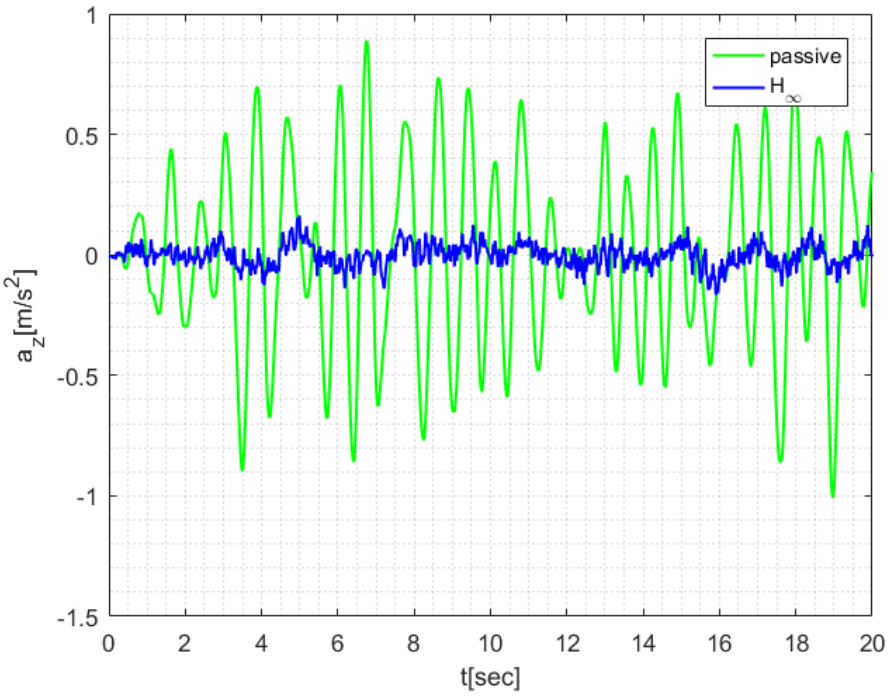

Figure 7.12: SMA values for the passive system and H_∞ controller

The SMA results acquired at the end of the simulation are satisfying. Gathered SMA RMS with H_∞ controller is lower than 0.06 m/s^2. Ride comfort is quite improved when it is compared with the passive suspension system.

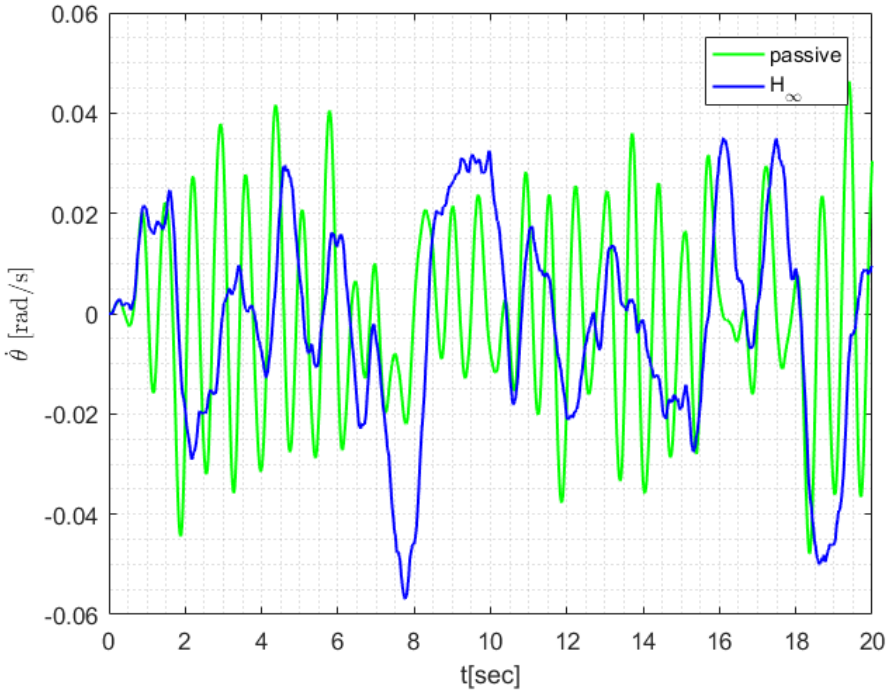

Figure 7.13: Pitch rate values for the passive system and H∞ controller

Pitch rate values of the H∞ controller shown with the blue line in Figure 7.13 are slightly higher than the pitch rate obtained with the passive suspension system. This result is expected because the objective of the H∞ controller minimizing SMA, pitch rate is only limited, and results satisfy a 0.2 rad/sec pitch rate limit.

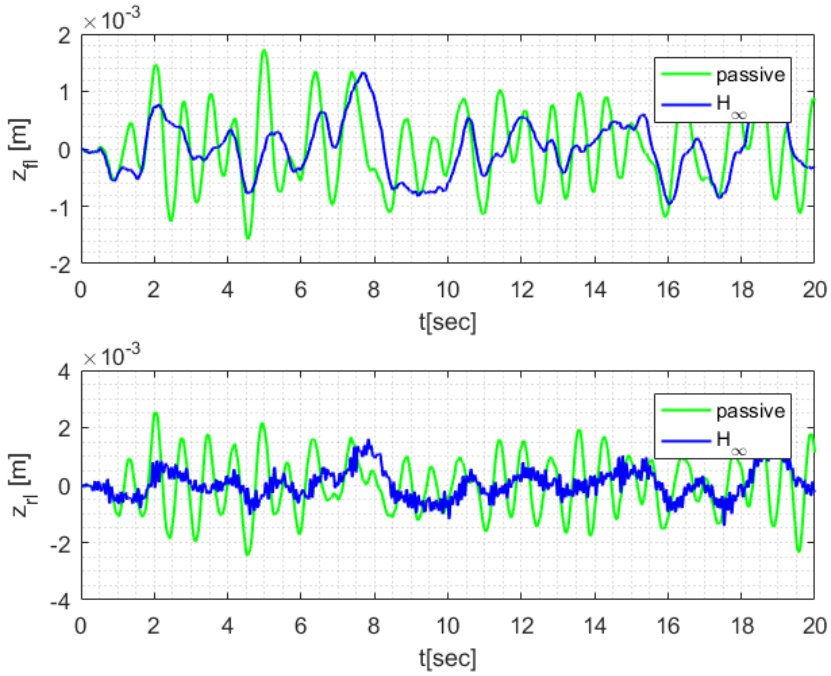

Figure 7.14: Front and rear wheel travels for passive system and H_∞ controller

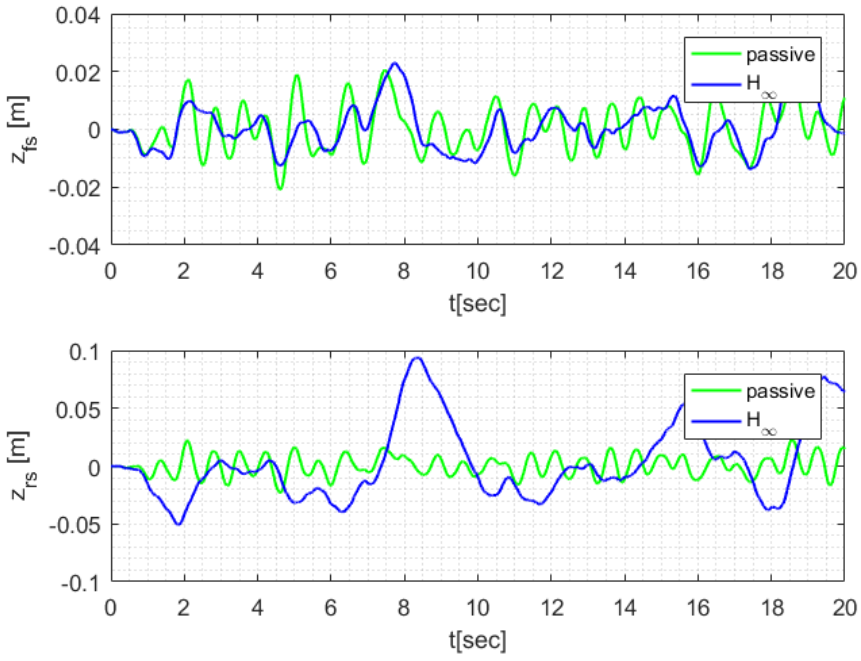

Figure 7.15: Front and rear suspension deflections for passive system and H_∞ controller

Wheel travels and suspension deflections are also below defined limits. The linear actuators are put in the rear compartment; thus, front wheel travel and suspension deflection give similar results to the passive system. However, the effect of the linear actuator can be seen from rear wheel travel and suspension deflection; wheel travel is decreased, and at the same time, suspension deflection is getting higher due to suspension movements.

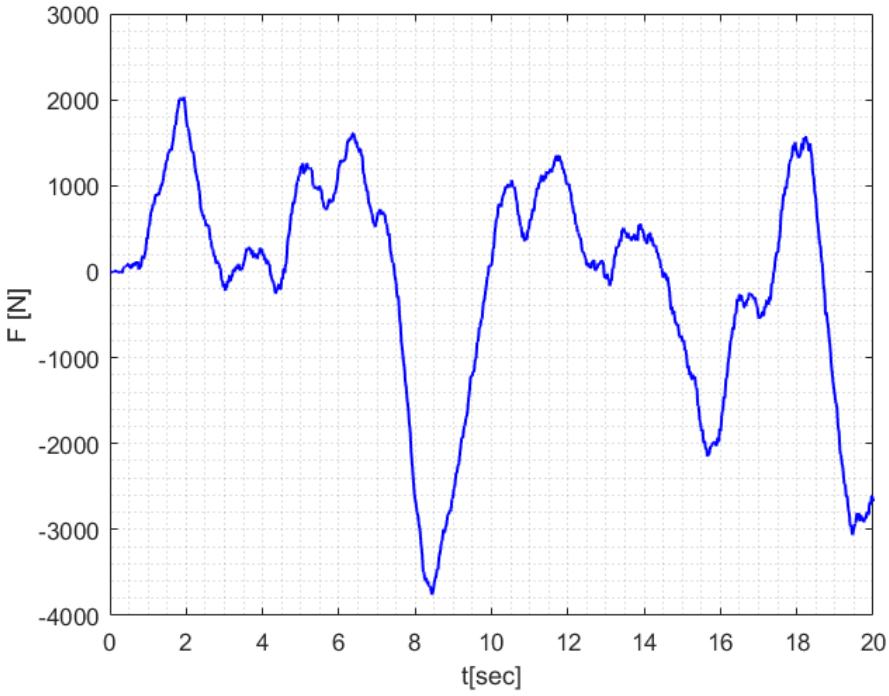

Figure 7.16: Total actuator force for H_∞ controller

The total maximum force limit of two actuators is 4300 N [3], and linear actuators are used more aggressively and obtained forces close to the maximum limit.

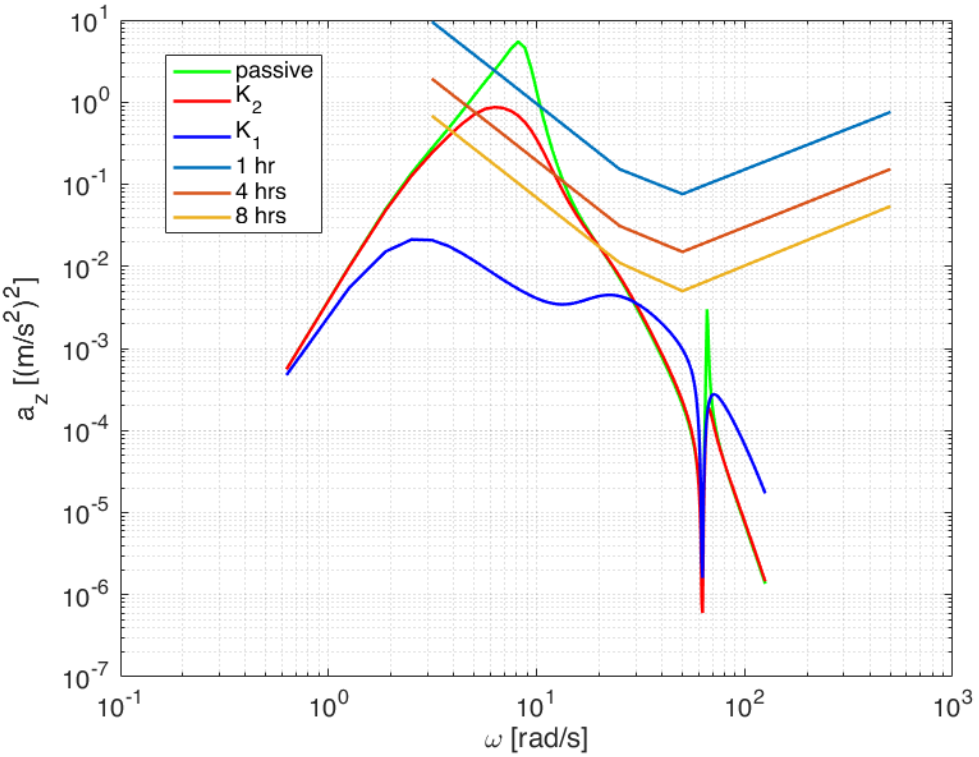

Figure 7.17: PSD of SMA for the passive system, H_∞ controller and comfort boundary lines for 1 hour, 4 and 8 hours

Both the finite frequency and the standard (entire frequency) H_∞ controllers give better responses than the passive suspension system. Until 4.5 Hz standard H_∞ controller (blue line) is better but, after 4.5 Hz finite, the other one has lower PSD of SMA. In time-domain plots, between Figure 7.12 and Figure 7.15, the differences between the two H_∞ controllers do not seem due to switching, but in Figure 7.17, the advantage of switching is observed clearly. Until the 3 Hz, the blue line has better performance, and after that point, the finite frequency H_∞ controller is better.

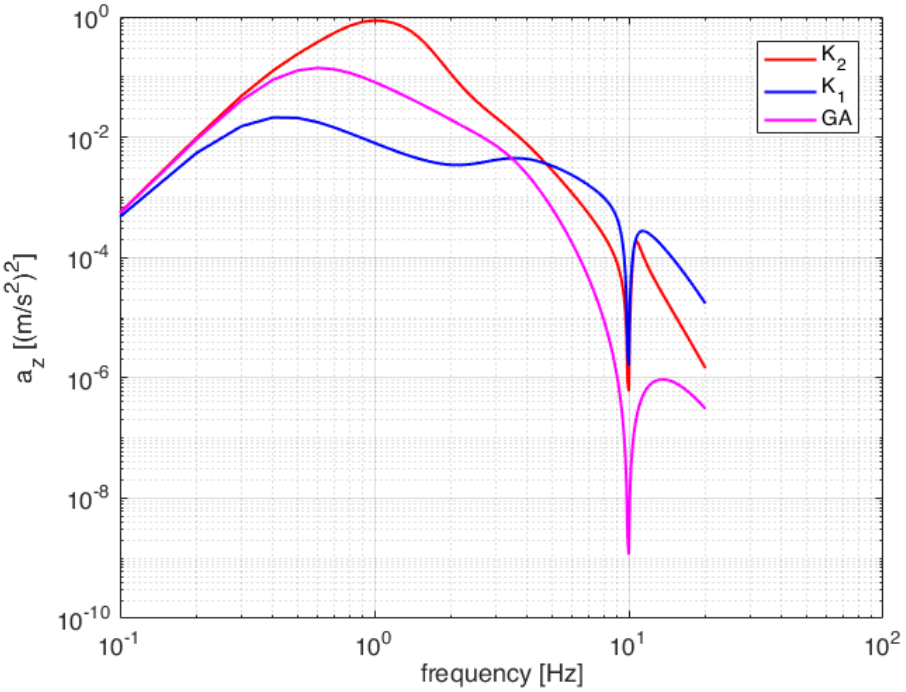

Figure 7.18: PSD of SMA for the H_∞ controller (K_1 and K_2) and LQR optimized with GA

All results were found for the frequency domain combined in Figure 7.18 to observe the efficiency of controllers. The magenta line represents the result found for LQR optimized with GA, and other lines represent H_∞ controllers. The given cursor shows that in frequencies lower than 3.4 Hz standard H_∞ controller designed for the entire frequency range provides the best result. However, after 3.4 Hz, the magenta line gives the best performance. This figure shows that there are low peaks at 10 Hz for all types of controllers. These lower peaks are called wheel hop, and due to strong suspension forces, it is expected to see these peaks. The 8 hours comfort boundary line or RMS of SMA specified by ISO standards is satisfied with H_∞ and LQR controllers, but their performances are changing at different frequencies.

7.2.3 Optimal Sliding Mode Control

Optimal sliding mode control is applied to the half-car model, as it is clarified in Chapter 5.4. The simulations are realized using Simulink, and the control structure for sliding mode control is given in Appendix B. Due to the non-linear characteristic of sliding mode control, only time-domain solutions are observed.

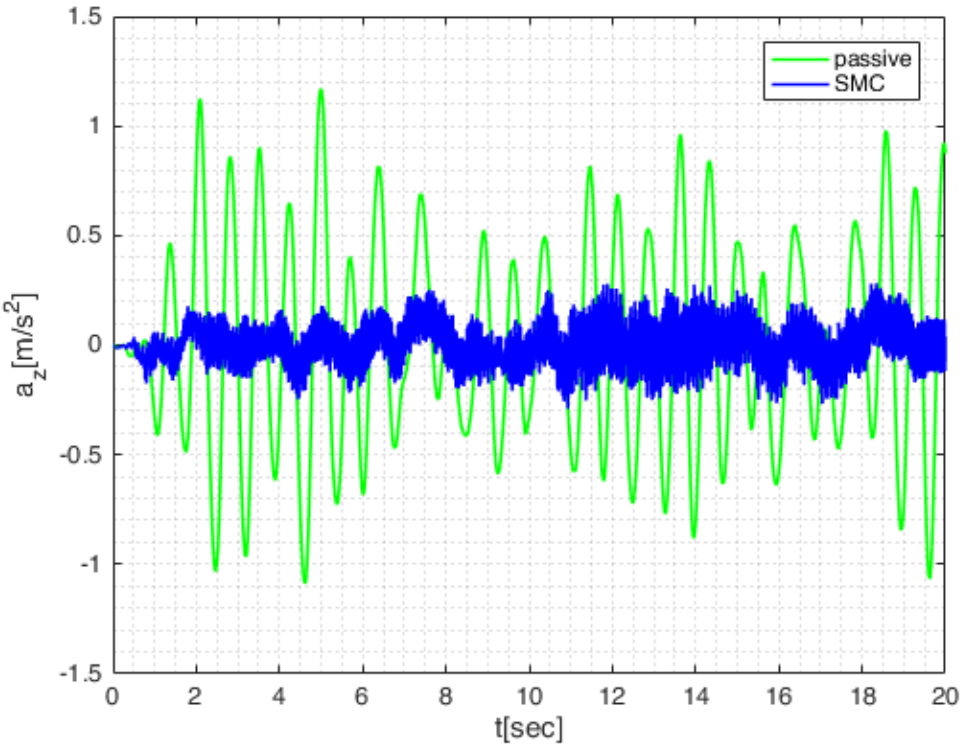

Figure 7.19: SMA values for the passive system and SMC

Figure 7.19 shows that SMA (thus ride comfort) is improved with optimal sliding mode control. In sliding mode control, the system reaches the sliding manifold and stays on the manifold by fluttering. Due to the fluttering nature of the SMC, observed SMA values are more fluttering when it is compared with the results of other controllers given in Figure 7.12 and Figure 7.6.

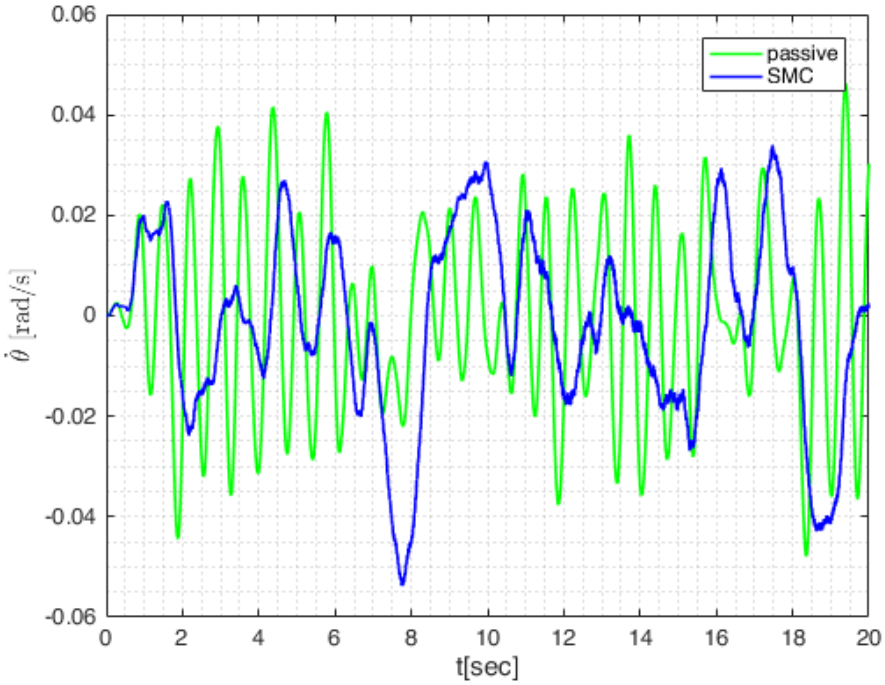

Figure 7.20: Pitch rate values for passive system and SMC

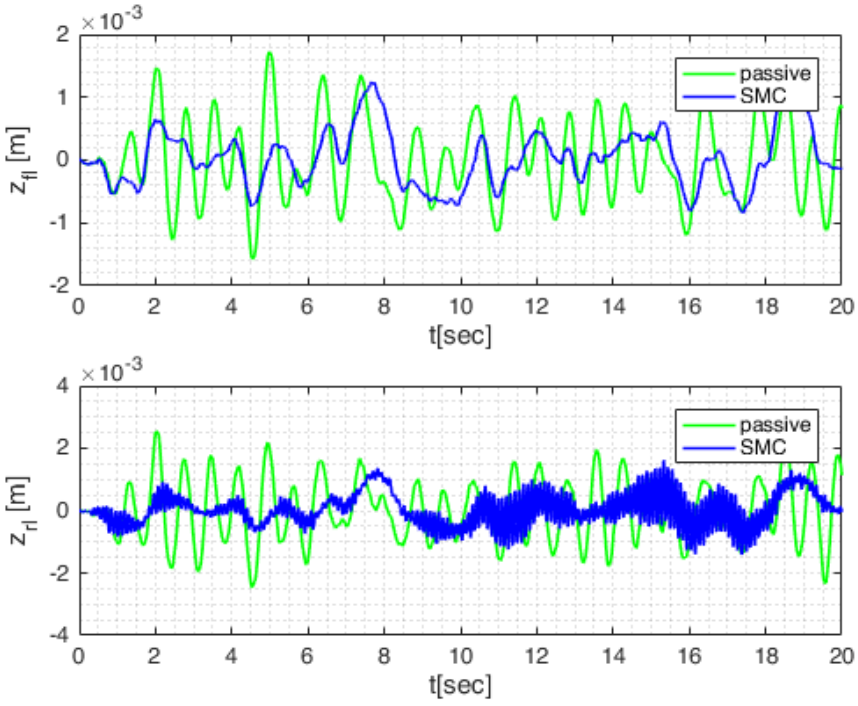

Figure 7.21: Front and rear wheel travels for passive system and SMC

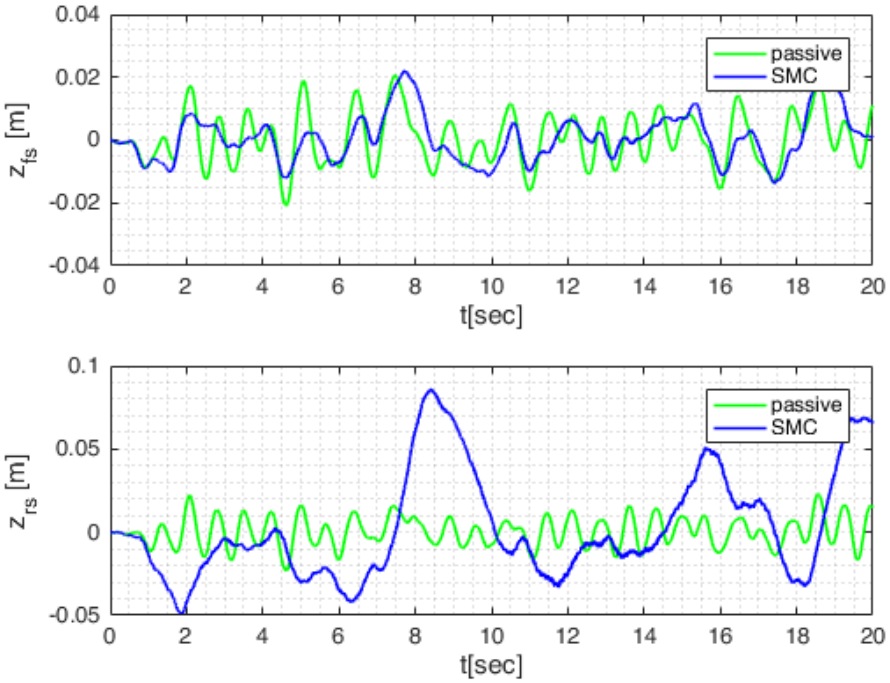

Figure 7.22: Front and rear suspension deflections for passive system and SMC

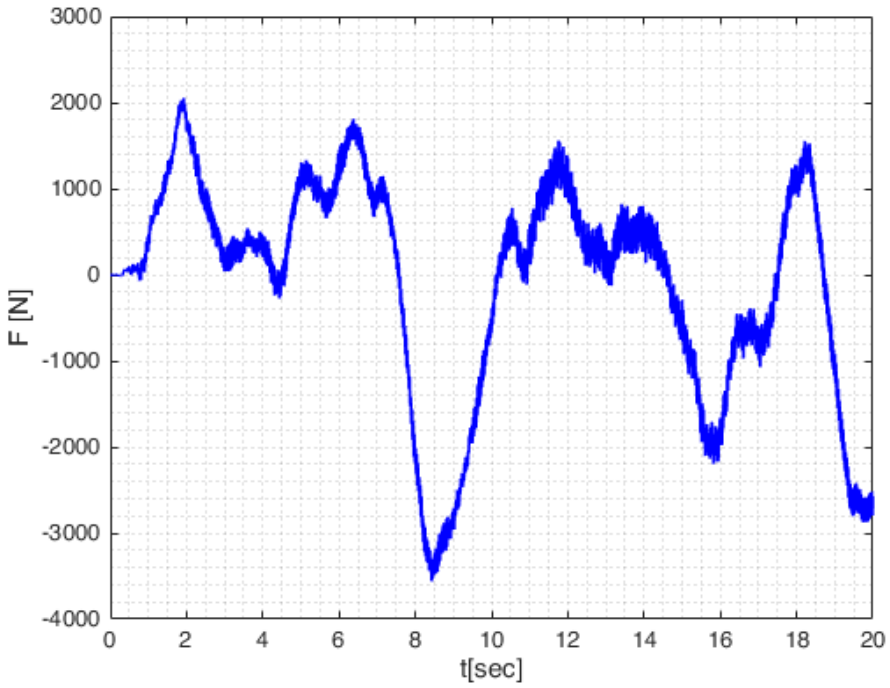

Figure 7.23: Total actuator force for SMC

The given results for SMC and H_∞ controller have very similar patterns. It can be observed in Figure 7.16 and Figure 7.23. However, the results for SMC have more oscillatory characteristics due to the switching nature of SMC. This oscillatory characteristic negatively affects SMA because oscillations increase the RMS of SMA and other system states.

Like the pitch rates and rear suspension deflections observed for LQR and H_∞ controllers, SMC also has higher pitch rates and suspension deflections than the passive suspension system because of linear actuators at the rear compartment.

Table 7.2: RMS values for sprung mass acceleration with different controllers

Suspension Type	**RMS values of SMA (m/s^2)**
Passive	0.4787
LQR with GA	0.0922
LQR with GD	0.1870
H_∞ control	0.0565
SMC	0.1025

If the RMS values of SMAs given in Table 7.2 are analyzed for all controllers, it is seen that active suspension with all types of controllers provides a better result than passive suspension. The RMS of SMA is 0.4066 m/s^2 for passive suspension, higher than the maximum limit of comfortable ride criteria specified as 0.25 m/s^2 in Figure 4.2. All of the controllers satisfy the maximum limit of SMA specified in Figure 4.2 in the time-domain. However, LQR optimized with GD does not satisfy 4 hours and 8 hours boundary lines; it only satisfies the 1-hour boundary line according to Figure 7.11.

Table 7.3: Closed-loop poles of active suspension systems

Passive	-11.0500 + 63.7203i, -11.0500 - 63.7203i, -11.2444 + 64.5375i, -11.2444 - 64.5375i, -0.4078 + 9.0327i, -0.4078 - 9.0327i, -2.4017 + 5.3890i, -2.4017 - 5.3890i
LQR with GA	-139.6844 + 0.0000i, -11.0456 + 63.7222i, -11.0456 - 63.7222i, -30.8008 + 0.0000i, -8.4021 + 9.7975i, -8.4021- 9.7975i, -2.7634 + 3.1016i, -2.7634 - 3.1016i
LQR with GD	-18.1335 + 63.6110i, -18.1335 - 63.6110i, -11.0455 + 63.7223i, -11.0455 - 63.7223i, -2.8710 + 8.8023i, -2.8710 - 8.8023i, -2.4888 + 5.1444i, -2.4888 - 5.1444i
H_∞ control (K1)	-108.7355 + 0.0000i, -10.9410 + 63.6907i, -10.9410 - 63.6907i -5.3143 + 62.8978i, -5.3143 - 62.8978i, -23.0220 + 0.0000i -3.2030 + 0.0000i, -1.9146 + 0.0000i
H_∞ control (K2)	-2.5753 + 65.6494i, -2.5753 - 65.6494i, -11.0468 + 63.7222i -11.0468 - 63.7222i, -3.4621 + 8.6646i, -3.4621 - 8.6646i -2.6992 + 5.1516i, -2.6992 - 5.1516i

The response of the system is affected by the location of the closed-loop poles. In the given table above, the closed-loop pole locations for different controllers are represented. The SMA values are improved while the pole locations go further away from the origin. In LQR control optimized with GA and entire frequency H_∞ control cases, there are poles at lower than -100. Thus, it is expected to see the best performances using them. Also, it is seen that in the closed-loop poles of the passive system, there are two poles close to the origin. These closed-loop poles close to the origin affects system performance badly.

7.3 Real-Time Frequency Spectrum Test Results

The real-time spectrum analysis is used for the implementation of H_∞ control in this study as it is explained in Chapter 6.3. Test of real-time spectrum analysis is made with Arduino Uno [36] and SparkFun LSM9DS1 9 DOF IMU [39]. IMU and Arduino are mounted on the chassis of a car in the Automotive Library of METU, as shown in Figure 7.24.

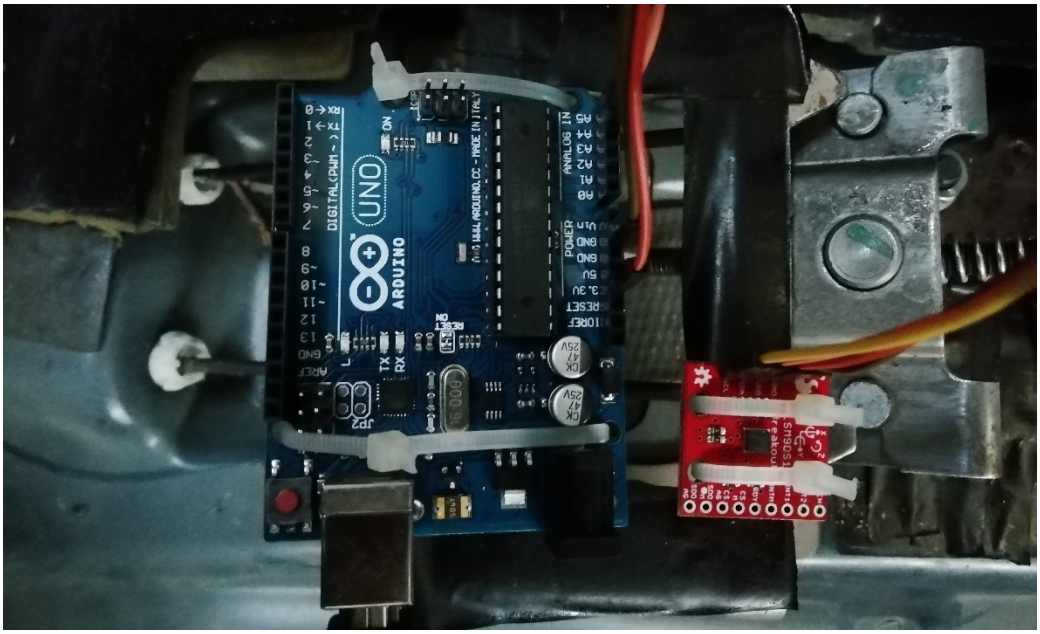

Figure 7.24: Arduino Uno and SparkFun IMU implementation on the chassis of the car

The data taken from IMU emulated to the computer with Arduino, and real-time spectrum analysis is carried out with Simulink. Tests are accomplished both on the road and bump on campus. Different constant velocities are used for the evaluation of real-time spectrum analysis.

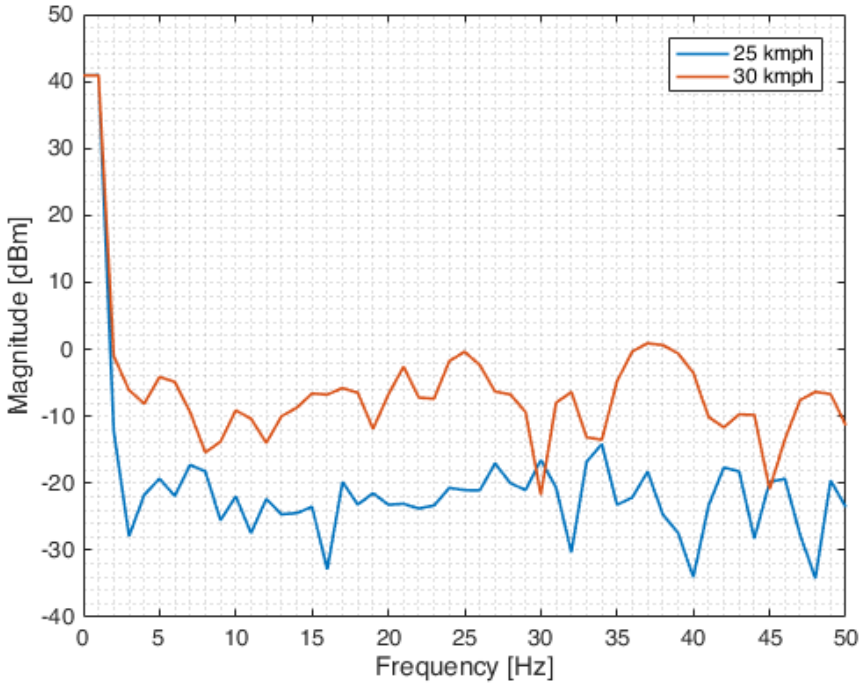

Figure 7.25: Real-time FFT of SMA of a car driven by 25 kmph vs. 30 kmph in a road on campus

Figure 7.25 shows the velocity dependency of a system. The fastest vehicle speeds damage the ride comfort more than the slowest speeds. It is important for the vehicle system because, unlike the constant velocity assumption of this study, commercial vehicles have alternating vehicle speeds. Efficient controllers can be designed for both different road types and vehicle speeds, using real-time spectrum analysis. Also, it is seen that the body bounce of the vehicle caused to dominant frequency content at 1 Hz.

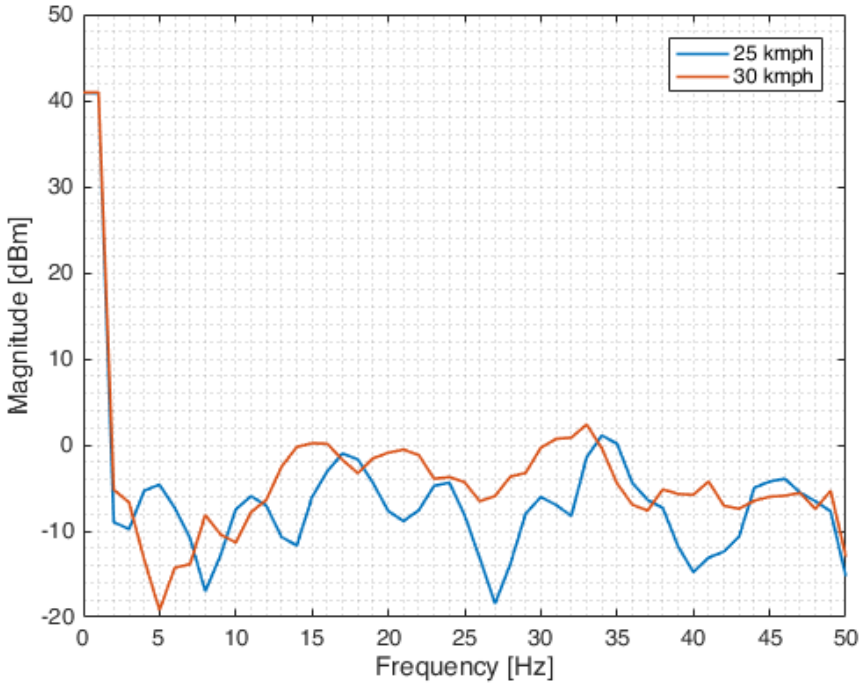

Figure 7.26: Real-time FFT of SMA of a car driven by 25 kmph vs. 30 kmph in a bump on campus

The plot results are gathered on a bump on campus with constant 25 kmph and 30 kmph speeds. Frequency-dependent dominant SMAs are more apparent with tests with a bump. In Figure 7.26, it is shown that lower frequencies are more dominant on a bump. The difference in SMAs between frequencies increases when vehicle speed increases. The orange line represents the 30 kmph constant velocity, and it gives higher magnitudes than the 25 kmph case. Furthermore, in comparison to Figure 7.25, the average trends of spectrums in Figure 7.26 are higher due to the frequency content of the bump.

CHAPTER 8

DISCUSSION AND CONCLUSION

8.1 General Discussion

In this part, simulation and test results are investigated. The simulations are carried out by considering straight line driving at constant vehicle speed at 40 kmph (excluding the real-time FFT results in Chapter 7.3). The simulation results for three different controllers are presented. Before the application of controllers, Kalman filter results are observed. Error percentage was less than 1.2% percent for all of the estimated states.

In the observed results of LQR, GD based algorithm cause local minima problems, and the only 1-hour comfort boundary line is satisfied. However, 8 hours of comfort boundary condition is satisfied with LQR optimized using GA.

The H_∞ controller gives the best results in time-domain between all controllers. Also, the structure of combined H_∞ controllers provided an advantage in the frequency-domain analysis. The SMC also performs better than the passive suspension system and LQR optimized with GD with an SMA RMS of 0.10 m/s^2.

The results observed by all controllers show that the rear suspension deflections, z_{rs}, values kept bounded within the maximum limits. The maximum limit of rear suspension deflection is taken as 0.05 m by considering vehicle stability. Pitch rate constraint (0.2 rad/sec) is also satisfied.

The simulation results show that a well-optimized LQR, H_∞ controller, and SMC is applicable with a linear electric motor.

The real-time spectrum tests show that it is possible to see the frequency content of the SMA. Vehicle speed and road input are variant parameters in this test, and both of them affect magnitudes at different frequencies.

8.2 Conclusion

The objective of this study was to improve the ride comfort of a conventional car while satisfying the road holding conditions by using a linear electric motor for an active suspension system. The equations of motions with 4 degrees of freedom and state-space representation of the vehicle are derived using the half-car model, which is sufficient for analyzing the sprung mass acceleration, pitch rate and physical constraints of the system; suspension and wheel deflection.

This study also aims to evaluate the effects of different controllers in the active suspension system. Investigation begins with a classical PID controller; the root locus analysis of SISO actuator input to SMA shows that system is not stabilizable with the PID controller. The MIMO controllers are desired for this system.

In the second case, the LQR is designed for the system. The diagonal elements of the weighting matrix of LQR are optimized with GA and GD based Trust-Region algorithms to get optimal results.

Another approach was controlling the system with H_∞ controllers by considering the incoming random road input frequency content. A standard entire frequency H_∞ controller is combined with an H_∞ controller designed for improving performance between 4 and 8 Hz. The frequency range between 4 Hz and 8 Hz is chosen since it is the most critical frequency range for the human body. The switching mechanism is obtained by using real-time spectrum analysis, and using spectrum results dominant frequency range is obtained. If the dominant frequency is less than 4 Hz, the entire frequency H_∞ controller is applied, but the finite frequency $H\infty$ controller is carried out in simulation for higher frequencies.

Both the LQR and H_∞ controllers are linear. However, it is known that nonlinear controllers are successful in disturbance rejection problems since, in the nonlinear controllers, trajectories are reached to the sliding manifold and stay on the manifold. Hence, a first-order optimal SMC is also designed and compared with other controllers.

It should also be noted that a state estimator was necessary to apply controllers because all of the given controllers include unmeasured states. The Kalman filter is used for this purpose, and unmeasured states are estimated.

Finally, the real-time frequency spectrum results were observed with campus road and two different vehicle speeds.

8.3 Future Works

Because of the time limitation, the implementation of linear motors to a vehicle could not be achieved. In the next step, the effect of these controllers can be observed in a real setup. Also, extrinsic SparkFun IMU is used for real-time spectrum analysis, but it has a low-level grade accelerometer. Therefore, using a vehicle based produced accelerometers probably will give better results. Furthermore, the suspension system of the vehicle can be identified better by collecting more real-time spectrum data. This would give better values for suspension stiffness and damping coefficients.

REFERENCES

[1] R. Crowder, Electric Drives and Electromechanical Systems. 2005.

[2] https://www.a-m-c.com/types-of-motors-in-motion-control/

[3] Linmot, Model P10-70x400U/150-BL-QJ Company url: https://linmot.com.

[4] ISO 2631 – 1 1997 "Mechanical vibration and shock-Evaluation of human exposure to whole-body vibration" Part 1: General requirements. ISO.

[5] ISO-8608, "International Standard 8608: Mechanical Vibration – Road Surface Profiles – Reporting of Measured Data," vol. 2016, p. 29, 2011

[6] X. D. Xue et al., "Study of art of automotive active suspensions," 2011 4th Int. Conf. Power Electron. Syst. Appl. PESA, 2011

[7] Martins, J. Esteves, G. D. Marques, and F. P. da Silva, "Permanent-magnets linear actuators applicability in automobile active suspensions," IEEE Trans. Veh. Technol., vol. 55, no. 1, pp. 86–94, 2006

[8] B. L. J. Gysen, J. J. H. Paulides, J. L. G. Janssen, and E. A. Lomonova, "Active electromagnetic suspension system for improved vehicle dynamics," IEEE Trans. Veh. Technol., 2010

[9] C. F. Zhou, L. B. Liu, and Q. Zhang, "Simulation Research on Dynamics Performance of Active Suspension of Car," in 2019 IEEE 5th International Conference on Mechatronics System and Robots, ICMSR, 2019

[10] Bhangal, Narinder & Maurya, "Optimal Control of Vehicle Active Suspension System", Journal of Automation and Control Engineering. 6. 22-26. 10.18178/joace.6.1.22-26. , 2018

[11] M. Kaleemullah, W. F. Faris, F. Hasbullah, and N. M. Ghazaly, "Optimization of robust and LQR control parameters for half car model using genetic algorithm," Int. J. Adv. Sci. Technol., 2019.

[12] Y. Huang, J. Na, X. Wu, X. Liu, and Y. Guo, "Adaptive control of nonlinear uncertain active suspension systems with prescribed performance," ISA Trans., 2015

[13] Yagiz, Nurkan, et al. "Fuzzy Sliding-Mode Control of Active Suspensions." IEEE Transactions on Industrial Electronics, 2008.

[14] H. Li, J. Yu, C. Hilton, and H. Liu, “Adaptive sliding-mode control for nonlinear active suspension vehicle systems using T-S fuzzy approach,” IEEE Trans. Ind. Electron., 2013.

[15] B. L. Zhang, G. Y. Tang, and F. L. Cao, “Optimal sliding mode control for active suspension systems,” Proc. 2009 IEEE Int. Conf. Networking, Sens. Control. ICNSC 2009, pp. 351–356, 2009

[16] S. A. Chen, J. C. Wang, M. Yao, and Y. B. Kim, “Improved optimal sliding mode control for a non-linear vehicle active suspension system,” J. Sound Vib., vol. 395, pp. 1–25, 2017

[17] Zhou, X. Liu, W. Chen, F. Xu, and B. Cao, “Optimal sliding mode control for an active suspension system based on a genetic algorithm,” Algorithms, 2018

[18] Li, H. and Liu, H., “Active Control for Actuator Uncertain Half-car Suspension Systems” In: Handbook of Vehicle Suspension Control Systems, The Institution of Engineering and Technology, 2013.

[19] Sun, W., Pan, H., Wang, P. and Gao, H. “Active Suspension Control with Finite Frequency Approach” In: Handbook of Vehicle Suspension Control Systems, The Institution of Engineering and Technology, 2013.

[20] C. S. Dharankar, M. K. Hada, and S. Chandel, “Numerical generation of road profile through spectral description for simulation of vehicle suspension,” J. Brazilian Soc. Mech. Sci. Eng., 2017

[21] N. Kovvali, M. Banavar, and A. Spanias, “An introduction to Kalman filtering with MATLAB examples”, vol. 12. 2013.

[22] Grewal, Mohinder S., and Angus P. Andrews. “Kalman Filtering Theory and Practice Using MATLAB”, Wiley, 2015

[23] Y. Bar-Shalom, X.-R. Li, and T. Kirubarajan, “Estimation with Applications to Tracking and Navigation”, 2001.

[24] M. J. Griffin, “Discomfort from feeling vehicle vibration,” User Modeling and User-Adapted Interaction. 2007.

[25] N. J. Mansfield, “Introduction to Vibration,” in Human Response to Vibration, 2018.

[26] Ogata, Katsuhiko, “Modern Control Engineering”, Pearson, 2016.

[27] Zhou, K., Doyle, J. C. and Glover, K., “Robust and Optimal Control”, 1996

[28] Iwasaki, T. Meinsma, G. and Fu, M. “Generalized S-Procedure and Finite Frequency KYP Lemma”, Mathematical Problems in Engineering, Vol. 6, pp. 305 – 320., 2000

[29] Iwasaki, T., Hara, S. and Yamauchi, H. “Dynamical System Design from a Control Perspective: Finite Frequency Positive-Realness Approach” IEEE Transactions on Automatic Control, 2003

[30] Sun, Wenyu, and Ya-xiang Yuan. “Optimization Theory and Methods: Nonlinear Programming”. Springer, 2010.

[31] Nocedal, Jorge, and Stephen J. Wright. “Numerical Optimization”. Springer, 2006.

[32] Coley, David A. “An Introduction to Genetic Algorithms for Scientists and Engineers.” World Scientific, 1999.

[33] Mitchell, Melanie, “An Introduction to Genetic Algorithms,” MIT, 1998.

[34] C. W. Ahn, “Practical genetic algorithms”, vol. 18. 2006.

[35] Oppenheim, Alan V, and Ronald W. Schafer, “Discrete-Time Signal Processing”, Pearson, 2010.

[36] M. Frigo and S. G. Johnson, “The design and implementation of FFTW3,” in Proceedings of the IEEE, 2005.

[37] Oppenheim, Alan V, and Ronald W. Schafer, “Discrete-Time Signal Processing”, Pearson, 2010.

[38] “Arduino Uno Rev3 | Arduino Official Store.”, Available: https://store.arduino.cc/usa/arduino-uno-rev3.

[39] “SparkFun 9DoF IMU Breakout - LSM9DS1 - SEN-13284 - SparkFun Electronics.”, Available: https://www.sparkfun.com/products/13284.

APPENDICES

Appendix A: General View of the Simulation Model

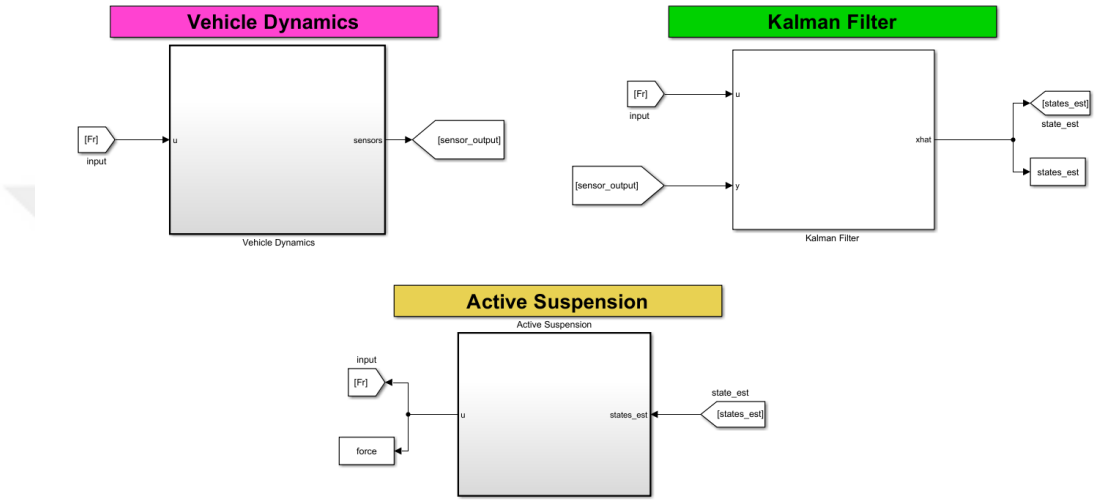

Figure A.1: General Structure of Half-Car Vehicle Model

Appendix B: Controller Dynamics with Simulations

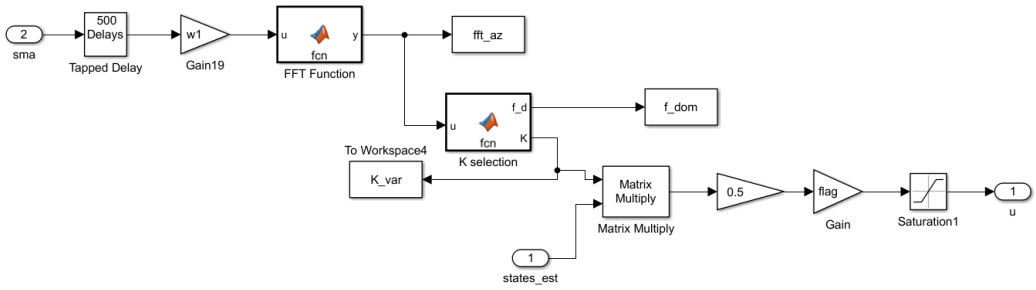

Figure B.1: H∞ control structure

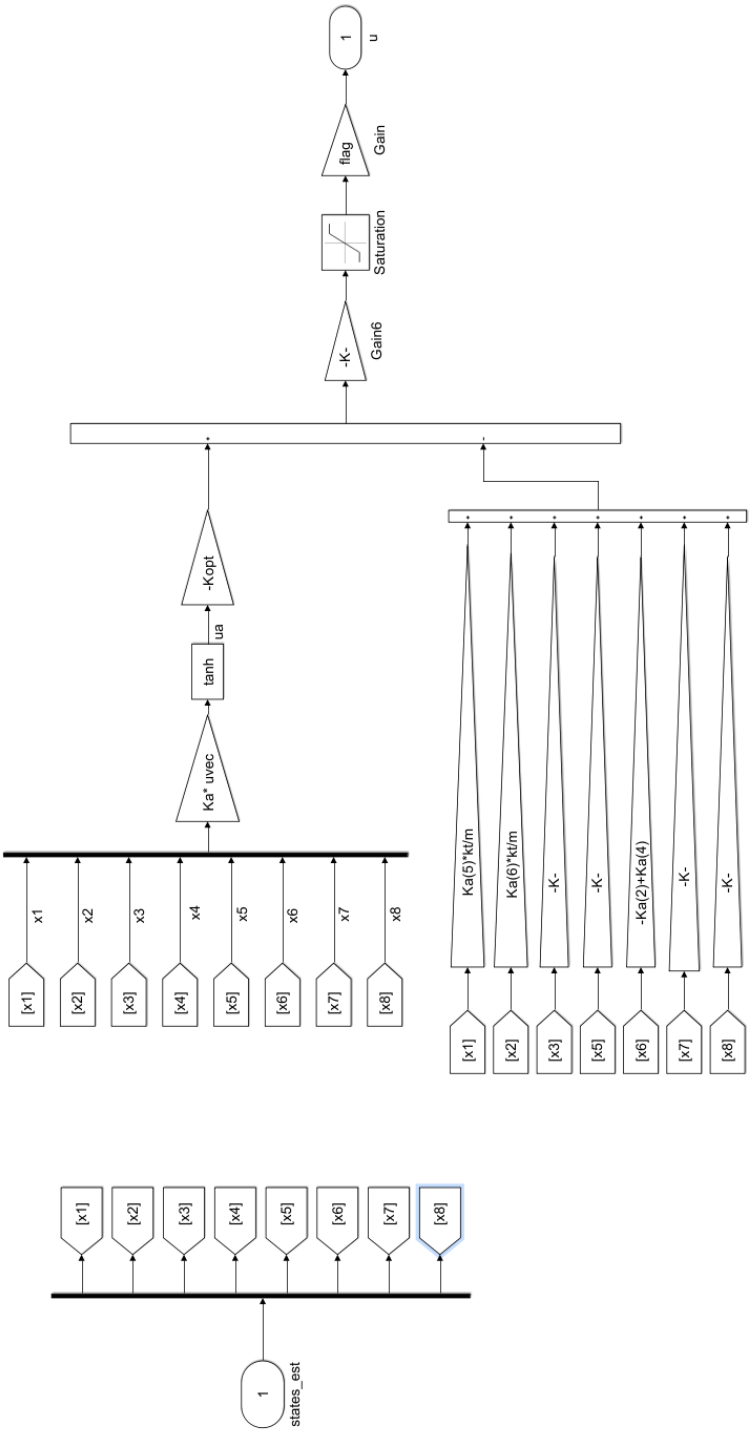

Figure B.2: Optimal sliding mode control structure

Appendix C: Proof of LMIs for Entire Frequency H∞ Control

Introduce $V(t) = x(t)^T P x(t)$ as Lyapunov function for proof of LMIs ((5.24)), P is a positive definite symmetric matrix. $\dot{V}(t) < 0$ should be satisfied for an asymptotically stable closed-loop system.

$$\dot{V}(t) = x^T(t)\big(sym(P\bar{A})\big)x^T(t) \tag{C.1}$$

For the H∞ performance of the active suspension system, the following algebraic Riccati equation can be written:

$$z_1^T(t)z_1(t) - \gamma^2 w^T(t)w(t) + \dot{V}(t) = [x^T(t)\ \ w^T(t)]\Theta\begin{bmatrix} x^T(t) \\ w^T(t) \end{bmatrix} \tag{C.2}$$

where

$$\Theta = \begin{bmatrix} sym\left(P\bar{A} + \bar{C_1}^T\bar{C_1}\right) & PB_1 \\ * & -\gamma^2 I \end{bmatrix} \tag{C.3}$$

If $sym(P\bar{A}) < 0$ and $\Theta < 0$, which means $\dot{V}(t) < 0$ hence it is guaranteed that $\|z_1\|_2 < \gamma^2\|w\|_2$. And the equation below can be written,

$$\begin{bmatrix} sym(P\bar{A}) & PB_1 & \bar{C_1}^T \\ * & -\gamma^2 I & 0 \\ * & * & -I \end{bmatrix} < 0 \tag{C.4}$$

Integrate Equation C.4 from 0 to t.

$$\dot{V}(t) - \gamma^2 w^T(t)w(t) < 0 \tag{C.5}$$

Results with

$$V(t) - V(0) < \gamma^2 \int_0^t w^T(t)w(t)dt < \gamma^2\|w\|_2^2 \tag{C.6}$$

$V(t) = x(t)^T P x(t) < \rho$ with $\rho = \gamma^2\, w_{max} + V(0)$

Now consider

$$max|z_2(t)|^2 = max\|x^T\bar{C}_2^T\bar{C}_2x\|_2 = max\left\|x^T\sqrt{P}\frac{1}{\sqrt{P}}\bar{C}_2^T\bar{C}_2\sqrt{P}\frac{1}{\sqrt{P}}x\right\|_2 < \rho\lambda_{max}\left(\frac{1}{\sqrt{P}}\bar{C}_2^T\bar{C}_2\frac{1}{\sqrt{P}}\right) \quad \text{(C.7)}$$

where λ_{max} is the maximum eigenvalue. The above equation can be written if C.7 is held:

$$\rho\left(\frac{1}{\sqrt{P}}\bar{C}_2^T\bar{C}_2\frac{1}{\sqrt{P}}\right) < I \quad \text{(C.8)}$$

Equation C.7 can be written as, by Schur complement [26]:

$$\begin{bmatrix} -P & \sqrt{\rho}\bar{C}_2^T \\ * & -I \end{bmatrix} < 0 \quad \text{(C.9)}$$

Also, a similar expression to Equation C.7 can be written for actuator input, F_r

$$max|u|^2 = max\|x^TK^TKx\|_2 = max\left\|x^T\sqrt{P}\frac{1}{\sqrt{P}}K^TK\sqrt{P}\frac{1}{\sqrt{P}}x\right\|_2 < \rho\lambda_{max}\left(\frac{1}{\sqrt{P}}K^TK\frac{1}{\sqrt{P}}\right) \quad \text{(C.10)}$$

It can be written that

$$\frac{\rho}{F_{rmax}^2}\left(\frac{1}{\sqrt{P}}K^TK\frac{1}{\sqrt{P}}\right) < 0 \quad \text{(C.11)}$$

Again, by using Schur complement [26]:

$$\begin{bmatrix} -P & \frac{\sqrt{\rho}}{F_{rmax}}K^T \\ * & -I \end{bmatrix} < 0 \quad \text{(C.12)}$$

If the equations [5.28, 5.33 and 5.36] are combined with T_1 and T_2 matrices:

$$T_1 = \begin{bmatrix} P^{-1} & 0 & 0 \\ 0 & I & 0 \\ 0 & 0 & I \end{bmatrix}$$

$$T_2 = \begin{bmatrix} P^{-1} & 0 \\ 0 & I \end{bmatrix} \quad \text{(C.13)}$$

Given LMIs in Equation 5.24, are proved.

$$T_1\begin{bmatrix} sym(P\bar{A}) & PB_1 & \bar{C}_1^T \\ * & -\gamma^2 I & 0 \\ * & * & -I \end{bmatrix}T_1^T = \begin{bmatrix} sym(A\bar{P}+B\bar{K}) & \text{G} & * \\ * & \text{-}\gamma^2 I & 0 \\ C_1\bar{P}+D_1\bar{K} & 0 & \text{-I} \end{bmatrix}$$

$$T_2\begin{bmatrix} \text{-P} & \sqrt{\rho}\bar{C}_2^T \\ * & \text{-I} \end{bmatrix}T_2^T = \begin{bmatrix} -\bar{P} & * \\ \sqrt{\rho}(C_2\bar{P}+D_2\bar{K}) & \text{-I} \end{bmatrix} \tag{C.14}$$

$$T_2\begin{bmatrix} -P & \frac{\sqrt{\rho}}{F_{rmax}}K^T \\ * & -I \end{bmatrix}T_2^T = \begin{bmatrix} -\bar{P} & \frac{\sqrt{\rho}}{F_{rmax}}\bar{K}^T \\ * & \text{-I} \end{bmatrix}$$

Appendix D: Proof of LMIs for Finite Frequency H_∞ Control

LMIs in Equation 5.27 are derived from the following set of LMIs

$$\begin{bmatrix} -[F]_S & F^T\bar{A}+P_1 & F^T & F^T\bar{B} \\ * & -P_1 & 0 & 0 \\ * & * & -P_1 & 0 \\ * & * & * & -\eta I \end{bmatrix} < 0$$

$$\begin{bmatrix} -Q & P+j\omega_c Q-F & 0 & 0 \\ * & -\omega_1\omega_2 Q+[F^T\bar{A}]_S & F^T\bar{B} & \bar{C}^T \\ * & * & -\gamma^2 I & 0 \\ * & * & * & -I \end{bmatrix} < 0 \qquad \text{(D.1)}$$

$$\begin{bmatrix} -I & \sqrt{\rho}C_2 \\ * & -P_1 \end{bmatrix} < 0$$

Proof: By using the Schur complement [27], the second equation in D.1 can be transformed into

$$\begin{bmatrix} \frac{1}{\eta}F^T GG^T F + F^T P_1^{-1} F - [F]_S & F^T\bar{A}+P_1 \\ * & -P_1 \end{bmatrix} < 0 \qquad \text{(D.2)}$$

by using the following matrix

$$\begin{bmatrix} F^{-1} & 0 \\ 0 & P_1^{-1} \end{bmatrix} \qquad \text{(D.3)}$$

where $F = W^{-1}$, Inequality D.2 can be transformed into

$$\begin{bmatrix} \frac{1}{\eta}\mathrm{GG}^T + P_1^{-1} - [W]_S & \bar{\mathrm{A}}P_1^{-1} + W^T \\ * & -P_1^{-1} \end{bmatrix} < 0 \qquad \text{(D.4)}$$

and by using the projection lemma from [11], Inequality D.3 is equivalent to

$$\bar{A}P_1^{-1} + P_1^{-1}\bar{A}^T + \frac{1}{\eta}GG^T < 0 \qquad \text{(D.5)}$$

Multiplying the inequality above, by the positive definite, symmetric matrix P_1 from both sides following expression can be held,

$$\bar{A}^T P_1 + P_1 \bar{A} + \frac{1}{\eta} P_1 G G^T P_1 < 0 \tag{D.6}$$

If Inequality D.6 holds, this means

$$\bar{A}^T P_1 + P_1 \bar{A} < 0 \tag{D.7}$$

According to the standard Lyapunov function, $V(t) = x^T(t) P_1 x(t)$, Inequality D.7 implies the closed-loop system is asymptotically stable.

The second term of D.1 can be expressed as follows:

$$\begin{bmatrix} I & 0 \\ 0 & I \\ 0 & 0 \end{bmatrix} \begin{bmatrix} -Q & P + j\omega_c Q \\ P - j\omega_c Q & -\omega_1 \omega_2 Q \end{bmatrix} \begin{bmatrix} I & 0 & 0 \\ 0 & I & 0 \end{bmatrix} + \begin{bmatrix} 0 & 0 \\ \bar{C}^T & 0 \\ 0 & I \end{bmatrix} \begin{bmatrix} I & 0 \\ 0 & -\gamma^2 I \end{bmatrix} \begin{bmatrix} 0 & \bar{C} & 0 \\ 0 & 0 & I \end{bmatrix} + \left[\begin{bmatrix} -I \\ \bar{A}^T \\ \bar{B}^T \end{bmatrix} F [0 \;\; I \;\; 0] \right]_S < 0 \tag{D.8}$$

and according to the projection lemma [11], Inequality D.8 holds, if and only if

$$\begin{bmatrix} I & 0 & 0 \\ 0 & 0 & I \end{bmatrix} \left(\begin{bmatrix} I & 0 \\ 0 & I \\ 0 & 0 \end{bmatrix} \begin{bmatrix} -Q & P + j\omega_c Q \\ P - j\omega_c Q & -\omega_1 \omega_2 Q \end{bmatrix} \begin{bmatrix} I & 0 & 0 \\ 0 & I & 0 \end{bmatrix} + \begin{bmatrix} 0 & 0 \\ \bar{C}^T & 0 \\ 0 & I \end{bmatrix} \begin{bmatrix} I & 0 \\ 0 & -\gamma^2 I \end{bmatrix} \begin{bmatrix} 0 & \bar{C} & 0 \\ 0 & 0 & I \end{bmatrix} \right) \begin{bmatrix} I & 0 \\ 0 & 0 \\ 0 & I \end{bmatrix} < 0$$

and

$$\begin{bmatrix} \bar{A}^T & I & 0 \\ \bar{B}^T & 0 & I \end{bmatrix} \left(\begin{bmatrix} I & 0 \\ 0 & I \\ 0 & 0 \end{bmatrix} \begin{bmatrix} -Q & P + j\omega_c Q \\ P - j\omega_c Q & -\omega_1 \omega_2 Q \end{bmatrix} \begin{bmatrix} I & 0 & 0 \\ 0 & I & 0 \end{bmatrix} + \begin{bmatrix} 0 & 0 \\ \bar{C}^T & 0 \\ 0 & I \end{bmatrix} \begin{bmatrix} I & 0 \\ 0 & -\gamma^2 I \end{bmatrix} \begin{bmatrix} 0 & \bar{C} & 0 \\ 0 & 0 & I \end{bmatrix} \right) \begin{bmatrix} \bar{A} & \bar{B} \\ I & 0 \\ 0 & I \end{bmatrix} < 0 \tag{D.9}$$

Inequality D.8 can be represented as follows:

$$\begin{bmatrix} \bar{A} & \bar{B} \\ I & 0 \end{bmatrix}^T \begin{bmatrix} -Q & P + j\omega_c Q \\ P - j\omega_c Q & -\omega_1 \omega_2 Q \end{bmatrix} \begin{bmatrix} \bar{A} & \bar{B} \\ I & 0 \end{bmatrix} + \begin{bmatrix} \bar{C} & 0 \\ 0 & I \end{bmatrix}^T \begin{bmatrix} I & 0 \\ 0 & -\gamma^2 I \end{bmatrix} \begin{bmatrix} \bar{C} & 0 \\ 0 & I \end{bmatrix} < 0 \tag{D.10}$$

which can be further transformed to

$$\begin{bmatrix}\bar{A} & \bar{B}\\ I & 0\end{bmatrix}^T \begin{bmatrix}-Q & P+j\omega_c Q\\ P-j\omega_c Q & -\omega_1\omega_2 Q\end{bmatrix}\begin{bmatrix}\bar{A} & \bar{B}\\ I & 0\end{bmatrix} + [\bar{C}\ \ 0]^T[\bar{C}\ \ 0] + \begin{bmatrix}0 & 0\\ 0 & -\gamma^2 I\end{bmatrix} < 0 \tag{D.11}$$

Lemma: Consider the linear system, *A*, *B*, *C*, *D*. Given a symmetric matrix Π, the following statements are equivalent:

1. The finite frequency inequality

$$\begin{bmatrix}G(j\omega)\\ I\end{bmatrix}^T \Pi \begin{bmatrix}G(j\omega)\\ I\end{bmatrix} < 0 \text{ for } \omega_1 < \omega < \omega_2 \tag{D.12}$$

2. There exist symmetric matrices *P* and *Q* satisfying $Q > 0$ and

$$\begin{bmatrix}\Gamma & [\bar{C}\ \ \bar{D}]^T\\ * & -I\end{bmatrix} < 0 \tag{D.13}$$

Where

$$\Gamma = \begin{bmatrix}A & \mathrm{B}\\ I & 0\end{bmatrix}^T \begin{bmatrix}-Q & P+j\omega_c Q\\ P-j\omega_c Q & -\omega_1\omega_2 Q\end{bmatrix}\begin{bmatrix}A & B\\ I & 0\end{bmatrix} + \begin{bmatrix}0 & \mathrm{C}^T\Pi_{12}\\ * & [D^T\Pi_{12}]_S + \Pi_{22}\end{bmatrix} \tag{D.14}$$

By using this Lemma [4,12] and Schur complement [11], Inequality D.11 and Inequality D.12 are equivalent.

Again considering the Lyapunov function without ignoring the disturbance term *w(t)*,

$$V(t) = x^T(t)P_1 x(t) \tag{D.15}$$

which yields

$$\dot{V}(t) = x^T(\bar{A}^T P_1 + P_1\bar{A})x + w^T G^T P_1 x + x^T P_1 G w \tag{D.16}$$

and

$$w^T G^T P_1 x + x^T P_1 G w < \frac{1}{\eta} x^T P_1 \bar{B}\bar{B}^T P_1 x + \eta w^T w \tag{D.17}$$

we have

$$\dot{V}(t) < x^T\left(\bar{A}^T P_1 + P_1\bar{A} + \frac{1}{\eta}P_1\bar{B}\bar{B}^T P_1\right)x + \eta w^T w \tag{D.18}$$

Considering Inequality D.6, Inequality D.18 guarantees

$$\dot{V}(t) < \eta w^T w \tag{D.19}$$

Integrating both sides of Inequality D.19, from *0* to *t* results in:

$$V(t) - V(0) < \eta \int_0^t w^T w dt < \eta \left|\left|w\right|\right|_2^2 = \eta w_{\boldsymbol{max}} \tag{D.20}$$

This shows that

$$x^T P_1 x < V(0) + \eta w_{\boldsymbol{max}} \tag{D.21}$$

For the last LMI, considering constrained outputs

$$\max_{t \geq 0} |z_2|^2 = \max_{t \geq 0} (x^T C_2^T C_2 x) \tag{D.22}$$

Defining $\bar{x} = \sqrt{P_1}.\, x$, it follows that $\bar{x}^T \bar{x} \leq \rho$, hence

$$\max_{t \geq 0} |z_2|^2 \leq \rho \lambda_{max} \left(\frac{1}{\sqrt{P_1}} C_2^T C_2 \frac{1}{\sqrt{P_1}} \right) \tag{D.23}$$

where λ_{max} represents the maximum Eigenvalue. Then the constraints defined for LMIs holds if

$$\rho \frac{1}{\sqrt{P_1}} C_2^T C_2 \frac{1}{\sqrt{P_1}} < I \tag{D.24}$$

which by Schur complement, is equivalent to the third equation in Inequality D.1, the last LMI.

Applying congruence transformation to inequalities in D.1,

$$J_1 = \begin{bmatrix} F^{-1} & 0 & 0 & 0 \\ 0 & F^{-1} & 0 & 0 \\ 0 & 0 & F^{-1} & 0 \\ 0 & 0 & 0 & I \end{bmatrix}$$

$$J_2 = \begin{bmatrix} F^{-1} & 0 & 0 & 0 \\ 0 & F^{-1} & 0 & 0 \\ 0 & 0 & I & 0 \\ 0 & 0 & 0 & I \end{bmatrix} \tag{D.25}$$

$$J_3 = \begin{bmatrix} I & 0 \\ 0 & F^{-1} \end{bmatrix}$$

concludes the proof.

Appendix E: Trust-Region Algorithm

Trust-Region algorithm works as below:

1. The initial radius of trust-region is $\Delta_0 \in (0, \bar{\Delta})$.
2. Compute the gradient at the current point $g(x_k) = \nabla f(x_k)$. If $\| g(x_k) \| \leq \varepsilon$, where ε is a convergence parameter x_k is the solution. Otherwise, continue.
3. Compute the Hessian $H(x_k) = \nabla^2 f(x_k)$ and solve quadratic trust-region subproblem. The next point in the algorithm is $x_k + s_k$. To find s_k, $q^k(s_k)$ which is the predicted solution of the problem is calculated as follows in Equation 6.1:

$$\min_{s_k \in \Re^n} q^k(s_k) = f(x_k) + g(x_k)^T s_k + \frac{1}{2} s_k^T H(x_k) s_k \qquad \text{(E.1)}$$
$$s.t. \ \|s_k\| \leq \Delta_k$$

4. One of the critical issues in updating the radius of trust-region at every iteration. The radius of trust-region should be set with respect to a ratio that measures the accuracy of the quadratic model. Actual reduction and predicted reduction are,

$$\Delta f_{actual_k} = f(x_k) - f(x_k + s_k) \qquad \text{(E.2)}$$
$$\Delta f_{pred_k} = q^k(0) - q^k(s_k) = f(x_k) - q(s_k)$$

5. Define the ratio,

$$r_k = \frac{\Delta f_{actual_k}}{\Delta f_{pred_k}} \qquad \text{(E.3)}$$

6. Set,

$$x_{k+1} = \begin{cases} x_k + s_k, & if \ r_k \geq \eta_1 \\ x_k, & otherwise \end{cases} \qquad \text{(E.4)}$$

7. The trust-region in the next step Δ_{k+1} is selected according to the accuracy ratio calculated in Equation 6.3.

   If $r_k < \eta_1$, then $\Delta_{k+1} = \gamma_1 \Delta_k$

   If $r_k \in [\eta_1, \eta_2)$, then $\Delta_{k+1} = \Delta_k$

If $r_k \geq \eta_2$, then $\Delta_{k+1} = \gamma_2 \Delta_k$ and $\|s_k\| = \Delta_k$

where η_1, η_2, γ_1 and γ_2 constant parameters determined by Optimization Toolbox.

8. Update points,

$$x_{k+1} = x_k \; if \; r_k \leq 0 \qquad \text{(E.5)}$$
$$x_{k+1} = x_k + s_k, otherwise$$

In this algorithm, the if $r_k \geq \eta_2$ iterations are very successful else if $r_k \geq \eta_1$ said to be iterations are successful; otherwise, iterations are unsuccessful [31].

Appendix F: GA and GD Optimization Algorithms

GA and Trust-Region algorithms applications with MATLAB optimization toolbox:

```
clc
clear
% Cost function is defined within lqr_parameters_obj function
J = @(x)lqr_parameters_obj(x);
% Nonlinear constraints of the optimization problem is defined within
% confun_lqr function
nonlcon = @(x)confun_lqr(x);
% Initial point of trust-region algorithm is defined
x0 = zeros(1,8);
% ConstraintTolerance: 1.0000e-06 and StepTolerance: 1.0000e-10 is kept
% maximum iteration number and maximum function evaluation are set as:
options =
optimoptions(@fmincon,'MaxIterations',2000,'MaxFunctionEvaluations',30000)
;
% Trust-Region algorithm is carried out with 'fmincon'
[xeval,feval] = fmincon(J,x0,[],[],[],[],zeros(8,1),[],nonlcon,options);
options = optimoptions(@ga,'FunctionTolerance',1e-
20,'MaxGenerations',500,'PopulationSize',200);
% PopulationSize: Inital population size set as 200 default if
% number of variables larger than 5.
% EliteCount: Number of individuals survive to generation,
% is determined as ceil(0.05*PopulationSize)
% Single point crossover is defined between 1 and nbits.
% Mutation rate is set gaussian mutation by default which adds a random
% number of mutation taken from Gaussian distribution.
[xeval,feval]= ga(J,8,[],[],[],[],zeros(8,1),[],nonlcon,options_ga);
```

Objective function is defined below:

```
function J=lqr_parameters_obj(x)
s=tf('s');
%%%%%%%%%%%%%%%%vehicle parameters%%%%%%%%%%%%%%%%%%
M=1500;       %Total mass [kg]
mf= 46;       %unsprung mass of wheel2 [kg]
mr= 46;       %unsprung mass of wheel3 [kg]
M_s=M-2*mf-2*mr;          %Vehicle sprung mass [kg]
tr=1.55;      %track [m]
a=1.2;        %distance from center of gravity to front axle [m]
b=1.5;        %distance from center of gravity to rear axle [m]z
c=0;          %lateral center of gravity position [m]
l=a+b;        %wheelbase [m]
h=0.45;       %center of gravity height [m]
h_s=0.2;      %distance between center of gravity and roll center [m]
Iw=1.5;       %wheel inertia + hub motor inertia [kg.m^2]
Izz=3887;     %vehicle inertia z-axis [kg.m^2]
Ixx=723;      %vehicle inertia x-axis [kg.m^2]
Iyy=2000;     %vehicle inertia y-axis [kg.m^2]
ksf= 15000;   %spring coefficient of suspension1 [N/m]
ksr= 20074;   %spring coefficient of suspension3 [N/m]
cf= 1000;     %damping coefficient of suspension1 [N.s/m]
cr= 50;       %damping coefficient of suspension3 [N.s/m]
kt= 180000;   %spring coefficient of tyre [N/m]
%%%%%%%%%%%%%%%%%%%%%%%%%%%%%%%%%%%%%%%%%%%%%%%%%%%%%
Vx = 40/3.6; %inital speed [m/s]
```

```
tau = (a+b)/Vx;
A = [0 0 0 0 -1 0 0 0;0 0 0 0 0 -1 0 0;0 0 0 0 1 0 a -1;0 0 0 0 0 1 -b -1;
...
    kt/mf 0 -ksf/mf 0 -cf/mf 0 -a*cf/mf cf/mf; ...
    0 kt/mr 0 -ksr/mr 0 -cr/mr b*cr/mr cr/mr; ...
    0 0 -2*a*ksf/Iyy 2*b*ksr/Iyy -2*a*cf/Iyy ...
    2*b*cr/Iyy (-2*cf*a^2-2*cr*b^2)/Iyy (2*cf*a-2*cr*b)/Iyy; ...
    0 0 2*ksf/M_s 2*ksr/M_s 2*cf/M_s 2*cr/M_s (2*cf*a-2*cr*b)/M_s+Vx (-
2*cf-2*cr)/M_s];
B = [0;0;0;0;0;-1/2/mr;b/Iyy;1/M_s];
G=[[0;0;1;0;0;0;0;0],[0;0;0;1;0;0;0;0]];
C=[0 0 2*ksf/M_s 2*ksr/M_s 2*cf/M_s 2*cr/M_s (2*cf*a-2*cr*b)/M_s+Vx (-
2*cf-2*cr)/M_s];
D=1/M_s;
Gout=[0 0];

for i=1:8
Q(i,i)=x(i);
end
rho=1e-7;
K=lqr(A,B,Q,rho);
tim=0:0.01:20;
w=sqrt(0.262144*Vx)*randn(length(tim),1);
w=w-mean(w);
 Ar=[-2];
 Br=eye(1);
 Cr=eye(1);
 Dr=zeros(1,1);
 z0f=lsim(Ar,Br,Cr,Dr,w,tim); %road profile [m]
 z0r=z0f;
 i=1;
 for t=0:0.01:tau
     z0r(i)=0;
 i=i+1;
 end
 %simulate
 sys=ss(A-B*K,G,C-D*K,Gout);
 sma=lsim(sys,[z0f z0r],tim);
%  global cost
%  assignin('base','cost',cost);
 J=rms(sma);
%  cost=[cost J];
```

Nonlinear constraints are defined below as:

```
function [C,Ceq]=confun_lqr(x)
s=tf('s');
%%%%%%%%%%%%%%%%vehicle parameters%%%%%%%%%%%%%%%%%%
M=1500;      %Total mass [kg]
mf= 46;      %unsprung mass of wheel2 [kg]
mr= 46;      %unsprung mass of wheel3 [kg]
M_s=M-2*mf-2*mr;          %Vehicle sprung mass [kg]
tr=1.55;     %track [m]
a=1.2;       %distance from center of gravity to front axle [m]
b=1.5;       %distance from center of gravity to rear axle [m]z
c=0;         %lateral center of gravity position [m]
l=a+b;       %wheelbase [m]
h=0.45;      %center of gravity height [m]
h_s=0.2;     %distance between center of gravity and roll center [m]
Iw=1.5;      %wheel inertia + hub motor inertia [kg.m^2]
Izz=3887;    %vehicle inertia z-axis [kg.m^2]
Ixx=723;     %vehicle inertia x-axis [kg.m^2]
```

```
Iyy=2000;     %vehicle inertia y-axis [kg.m^2]
ksf= 15000;   %spring coefficient of suspension1 [N/m]
ksr= 20074;   %spring coefficient of suspension3 [N/m]
cf= 1000;     %damping coefficient of suspension1 [N.s/m]
cr= 50;       %damping coefficient of suspension3 [N.s/m]
kt= 180000;   %spring coefficient of tyre [N/m]
%%%%%%%%%%%%%%%%%%%%%%%%%%%%%%%%%%%%%%%%%%%%%%%%%%%%%%%%%%%%
Vx = 40/3.6;
tau = (a+b)/Vx;
A = [0 0 0 0 -1 0 0 0;0 0 0 0 0 -1 0 0;0 0 0 0 1 0 a -1;0 0 0 0 0 1 -b -1;
...
    kt/mf 0 -ksf/mf 0 -cf/mf 0 -a*cf/mf cf/mf; ...
    0 kt/mr 0 -ksr/mr 0 -cr/mr b*cr/mr cr/mr; ...
    0 0 -2*a*ksf/Iyy 2*b*ksr/Iyy -2*a*cf/Iyy ...
    2*b*cr/Iyy (-2*cf*a^2-2*cr*b^2)/Iyy (2*cf*a-2*cr*b)/Iyy; ...
    0 0 2*ksf/M_s 2*ksr/M_s 2*cf/M_s 2*cr/M_s (2*cf*a-2*cr*b)/M_s+Vx (-
2*cf-2*cr)/M_s];
B = [0;0;0;0;0;-1/2/mr;b/Iyy;1/M_s];
G=[0;0;0;1;0;0;0;0];
C=[0 0 2*ksf/M_s 2*ksr/M_s 2*cf/M_s 2*cr/M_s (2*cf*a-2*cr*b)/M_s+Vx (-
2*cf-2*cr)/M_s];
D=1/M_s;
Gout=0;

for i=1:8
Q(i,i)=x(i);
end
rho=1e-7;

K=lqr(A,B,Q,rho);
%
%% ISO filter
f1=0.4;
f2=100;
f3=12.5;
f4=12.5;
f5=2.37;
f6=3.35;

w1=f1*2*pi;
w2=f2*2*pi;
w3=f3*2*pi;
w4=f4*2*pi;
w5=f5*2*pi;
w6=f6*2*pi;

Q4=0.63;
Q5=0.91;
Q6=0.91;

H_h=tf([1 0 0],[1 sqrt(2)*w1 w1^2]);
H_l=tf([w2^2],[1 sqrt(2)*w2 w2^2]);
H_t=tf([w4/w3 w4^2],[1 w4/Q4 w4^2]);
H_s=tf([1 w5/Q5 w5^2],[1 w6/Q6 w6^2]);

H=H_h*H_l*H_t*H_s;
%%
[num_dp,den_dp] = ss2tf(A-B*K,G,C-D*K,Gout); % closed loop tf between dist
and sma
az_road_input_cl_tf=tf(num_dp,den_dp);

PSDd = 0.262144*Vx/(-s^2+0.139^2);
az_filter_psd=PSDd*(H*az_road_input_cl_tf)^2;
```

```
w=(1:80)*2*pi;
[mag,phase,wout]=bode(az_filter_psd,w);
mag = mag(:,:);

for i=1:4
    bound(i)=0.173-((0.173-0.011)/3)*(i-1);
end
for i=5:8
    bound(i)=0.011-((0.011-0.005)/4)*(i-4);
end
for i=9:80
   bound(i)= 0.005 + ((0.054-0.005)/72)*(i-8);
end

%
C=[real(eig(A-B*K)) ;(mag-bound)'];
Ceq=[];
```